Precision fits for the LHC and beyond

Emma Slade

Oriel College

University of Oxford

A thesis submitted for the degree of

Doctor of Philosophy

Hilary Term 2020

Abstract

In this thesis we consider the phenomenology of Quantum Chromodynamics (QCD) and the Standard Model Effective Field Theory (SMEFT), with reference to the ongoing experiments at the Large Hadron Collider (LHC). Our emphasis is on constraining free parameters of the theories, such that the precision of theoretical calculations for the LHC are able to match the high level of experimental precision now available.

To this end, we discuss two fitting frameworks which aim to be robust and reliable ways to extract these free parameters of QCD and the SMEFT. In QCD we wish to extract the strong coupling constant at the mass of the Z boson, $\alpha_s(M_Z)$, and in the SMEFT we want to constrain the free parameters of the theory which allow for deviations from the Standard Model.

We will first introduce QCD and the SMEFT and theoretically motivate our studies. We then move on to introduce the fitting framework used to extract the strong coupling constant. We will use parton distribution functions (PDFs) to determine the strong coupling; PDFs themselves must also be extracted from data, and their determination introduces many sources of methodological uncertainties which can propagate into our determination of $\alpha_s(M_Z)$. We will discuss the tools developed in order to quantify these uncertainties and obtain a reliable estimate of $\alpha_s(M_Z)$.

In the second part of this thesis, we will discuss a novel framework developed to determine the free parameters of the SMEFT. Initially we will motivate and outline the new methodology, which we denote SMEFiT, and then apply the framework to a detailed analysis of the top sector at the LHC.

Statement of originality

This thesis is a record of the work performed during my DPhil and contains published research. The discussion in Chapter 3 contains results published in [1]. The discussion in Chapters 4 and 5 as well as much of the discussion in Sec. 2.2.2 contains results published in [2] as well as work in progress in a paper to appear [3].

Acknowledgements

First and foremost I would like to thank my supervisors, Gavin Salam and Juan Rojo. Juan, for bringing me to Oxford, encouraging me to work as an independent researcher from day one, and for his ability to find new and interesting research topics for me to work on. I have to thank Gavin for so kindly taking me on as a D.Phil student, and for teaching me so much about phenomenology in a short amount of time. I am most grateful especially for all the chats and support. A very big thanks must also go to Uli Haisch, who very kindly agreed to be my official supervisor in the first 2 years.

I have had the good fortune to have worked with many wonderful people over the last three years. I would particularly like to thank Nathan Hartland, Zahari Kassabov, Emanuele Nocera and Luca Rottoli; this thesis would not exist without the kindness and support of the four of them, and importantly would have been nowhere near as fun without all the gossip shared. Huge thanks also go to Matthew Lim and Luca Rottoli for proof-reading the thesis.

I have greatly enjoyed my time at the Rudolf Peierls Centre, and I would like to thank Michelle Bosher for her infinite efficiency with my endless expense forms and administrative issues, for co-founding cake club, and always making time when I needed a pep-talk. Thanks also go to John Chalker and Subir Sarkar for finding 3 months funding for me.

My final, and most important thanks are to my friends, Joshua, and my family, in particular mum, dad and Guy. This thesis would not have been possible without their support.

My D.Phil has received funding from the European Research Council (ERC), under the European Union's Horizon 2020 research and innovation programme (grant agreement No. 335260, PDF4BSM), and under the European Union's Horizon 2020 research and innovation programme (grant agreement No. 788223, PanScales).

Contents

CHAPTER 1

Introduction

With the discovery of the Higgs Boson [4, 5] in July 2012 at the Large Hadron Collider (LHC) and the completion of the particle content of the Standard Model (SM), the physics programme both experimentally and theoretically is focused on determining properties of the SM at high precision, allowing for deviations from the SM to be measured. Although the discovery of the Higgs Boson seems to complete the SM, we know that there exist phenomena that are not successfully described by it, such as neutrino masses. This strongly suggests that the SM is in fact not complete, and there exists some physics beyond the Standard Model (BSM). There exist several different frameworks which explain neutrino masses, such as the seesaw mechanisms [6–8], or effective field theory extensions of the SM [9]. In both cases, additional parameters are required to explain the neutrino masses. In the case of the seesaw mechanism, a right-handed neutrino is added which does not interact weakly, whilst in the case of the effective field theory extension, an additional operator at mass dimension 5 must be added.

The LHC has not yet found clear evidence of a direct signal of new physics beyond the SM. The experimental programme is now exploring the possibility

that BSM physics may appear indirectly in the form of a deviation from the SM in the tails of kinematic distributions [10–13]. Due to the very high statistics at the LHC, many experimental measurements can be incredibly precise, and theoretical predictions of collider processes must therefore be sufficiently accurate to correctly interpret the experimental data. When looking for deviations from the SM, the theoretical predictions of collider processes enter as predictions of the background to the BSM signal. Therefore, the theoretical understanding of the SM enters, both when doing precision phenomenology within the SM, but also when attempting to discover BSM physics. Furthermore, any theories which are used to model the BSM physics one hopes to find at the LHC (i.e. the signals), must also be known to high accuracy, so that different BSM models can be accurately distinguished from each other.

With the exception of ALICE, the main experiments at the LHC (ATLAS, CMS and LHCb) focus on measurements of proton-proton collisions. The theoretical framework which describes hadronic collisions is known as Quantum Chromodynamics (QCD). An important property of QCD is that it is described by a coupling constant, α_s, which decreases at high energy. In the limit of very high energies, cross sections can be theoretically calculated using perturbative methods. The structure of the proton, however, which is encoded via Parton Distribution Functions (PDFs), cannot be determined perturbatively and has to be extracted from data or from lattice calculations, where good progress has recently been made [14]. Using factorisation theorems, we can separate the long distance (PDF) behaviour from the short distance behaviour, allowing one to make predictions about the collisions at the LHC.

It is therefore of paramount importance that, in order to make predictions about collisions at the LHC, both the PDFs and accurate theoretical calculations for cross sections are known to high precision. Both the PDFs and the theoretical predictions for cross sections in QCD rely on the strong coupling constant. Along with the masses of the quarks, the strong coupling constant is one of the only free

parameters in QCD. Therefore, one must also have a precise way of determining its value. As we will discuss in Chapter 2, the strong coupling has a scale dependence; the knowledge of the scale dependence, along with a measurement or prediction of the coupling at some given scale therefore allows us to predict the coupling at any scale.

In this thesis, we will discuss two aspects of the precision physics programme at the LHC. Firstly, in Chapter 2 we will outline the theoretical frameworks needed in the thesis. We focus initially on QCD and introduce PDFs beginning with a study of deep inelastic scattering. We will then introduce the Standard Model Effective Field Theory (SMEFT), which is a model-independent theory which can be used to encapsulate deviations from the SM at high energies and therefore possibly provide information on the ultraviolet completion of the SM. The only assumptions needed to formulate the SMEFT are those of the SM, i.e. Lorentz covariance and the gauge symmetries of the SM.

We will discuss in Chapter 3 a novel method developed [1] to extract the value of the strong coupling using PDFs, specifically in the NNPDF3.1 framework [15]. As discussed above, precise knowledge of the strong coupling is important for theoretical calculations in QCD. In Chapter 4 we will discuss SMEFiT [2], a fitting framework developed to constrain free parameters in the SMEFT, and in Chapter 5, we apply the framework to the top sector at the LHC. The top sector has particular significance in BSM physics scenarios, due to the large mass of the top quark. As we will discuss, there are many bounds on the size of the free parameters in the SMEFT, within the top sector, which allow us to compare the results within the SMEFiT framework to those of other groups. Finally in Chapter 6 we draw our conclusions and summarise the work presented.

CHAPTER 2

Theoretical Framework

The basis of this thesis is the discussion of computational fits in two different quantum field theories; Quantum Chromodynamics and the Standard Model Effective Field Theory. We introduce the theories and their features relevant for the purpose of our work in turn.

2.1 Quantum Chromodynamics

In this section we will introduce more formally the theory of strong interactions. We will also discuss some useful aspects of QCD, namely the collinear factorisation theorem, and the running of the strong coupling, which we will need in Chapter 3. One of the central pillars of QCD are parton distribution functions (PDFs), as they factor out the non-perturbative long distance behaviour of the theory into universal functions, allowing us to compute the cross sections in perturbation theory. We will introduce PDFs via the framework of deep inelastic scattering. We begin with the naive parton model and build up to introduce the collinear factorisation theorem. As we will use PDFs to extract a value for α_s at the scale

of the Z mass, M_Z, we also introduce another fundamental aspect of QCD, the running of the strong coupling.

2.1.1 The QCD Lagrangian

QCD is a gauge theory with the gauge group of $SU(3)$. The Lagrangian is, at the classical level,

$$\mathcal{L} = \sum_f \bar{\psi}_{f,i}(i\not{D} - m_f)_{ij}\psi_{f,j} - \frac{1}{4}F^{a\mu\nu}F^a_{\mu\nu}\,, \tag{2.1}$$

where ψ_f are the quark fields, with mass m_f. The flavour index, $f = 1, \ldots, n_f$ and the colour indices $i, j = 1, \ldots, 3$. $\not{D}_{ij} \equiv \gamma_\mu D^\mu_{ij}$ is the covariant derivative,

$$D^\mu_{ij} = \partial^\mu \delta_{ij} + ig_s A^\mu_a t^a_{ij}\,, \tag{2.2}$$

where A^μ_a are the gluon fields, and the matrices t^a are the generators of the $SU(3)$ colour group in the fundamental representation. The generators satisfy

$$[t^a, t^b] = if^{abc}t^c, \quad \mathrm{Tr}(t^a t^b) = \frac{1}{2}\delta^{ab}\,, \tag{2.3}$$

where f^{abc} are the structure constants of the group. We can also define the field strength

$$F^a_{\mu\nu} = \partial_\mu A^a_\nu - \partial_\nu A^a_\mu - g_s f^{abc} A^b_\mu A^c_\nu\,, \tag{2.4}$$

where g_s is the QCD coupling. We note that the final term in Eq. (2.4), indicates the non-Abelian nature of $SU(3)$, not present in QED, and gives rise to the gluon self-interactions.

To quantise the Lagrangian, one must introduce additional gauge-fixing and ghost terms, modifying the Lagrangian to be

$$\mathcal{L} = \sum_f \bar{\psi}_{f,i}(i\not{D} - m_f)_{ij}\psi_{f,j} - \frac{1}{4}F^{a\mu\nu}F^a_{\mu\nu} - \frac{1}{2\xi}(\partial^\mu A^a_\mu)^2 + \partial^\mu \bar{\eta}^a D^{bc}_\mu \eta^c\,, \tag{2.5}$$

in the covariant gauge. The fields η^a are anti-commuting scalar fields known as ghosts, which we will discuss momentarily. The parameter ξ needs to be

fixed; common choices include the Feynman gauge ($\xi = 1$) and the unitary gauge ($\xi \to \infty$). D_μ^{bc} is the covariant derivative in the adjoint representation

$$D_\mu^{bc} = \partial_\mu \delta^{bc} + g_s f^{bca} A_\mu^a \,. \tag{2.6}$$

We need to ensure that the Lagrangian is invariant under local $SU(3)$ transformations. The quarks transform as

$$\psi(x) \to \psi'(x) = e^{ig_s t^a \theta^a(x)} \psi(x) \equiv U(x)\psi(x) \,, \tag{2.7}$$

and we require the covariant derivative to transform as

$$D_\mu \to D'_\mu = U(x) D_\mu U^\dagger(x) \,, \tag{2.8}$$

where we have dropped colour labels. This is satisfied if the gluon fields transform as

$$A_\mu \to A'_\mu = U(x) A_\mu U^\dagger(x) + \frac{i}{g_s} (\partial_\mu U(x)) U^\dagger(x) \,, \tag{2.9}$$

and therefore, for infinitesimal $\theta^b(x)$,

$$A_\mu^a \to A_\mu^{a'} = A_\mu^a - D_\mu^{ab} \theta^b(x) \,. \tag{2.10}$$

The gauge invariance of the quark sector is already accounted for in Eq. (2.1), by ensuring the covariant derivative transforms as Eq. (2.8). There is still a problem with the gluon field; there is some redundancy in the definition of the gluon field as only the transverse components propagate. Similarly to electromagnetism, we can introduce a gauge-fixing term

$$\mathcal{L}_{\text{gauge-fixing}} = -\frac{1}{2\xi} (\partial^\mu A_\mu^a)^2 \,, \tag{2.11}$$

but in QCD, it is necessary to add a further term,

$$\mathcal{L}_{\text{ghost}} = \partial^\mu \bar{\eta}^a D_\mu^{bc} \eta^c \,, \tag{2.12}$$

due to the non-Abelian nature of the theory. The derivation of these two additional terms can be derived by following the Faddeev–Popov gauge fixing procedure and may be found in any suitable QFT textbook; we will simply mention that

the ghost fields, η^a, are required to exclude the two unphysical components of A^a_μ; the longitudinal and timelike components. In QED, ghosts are not needed as the gauge-fixing term is sufficient to remove the unphysical components of the gauge field.

2.1.2 The QCD coupling constant

When computing observables beyond leading order in perturbation theory, one finds divergences arising from calculating loop diagrams which require an integral over an arbitrarily high momentum. Renormalisation systematically tames the appearance of these ultraviolet (UV) divergences in order to obtain a finite prediction for any observable. The idea behind renormalisation is to realise that the quantities in our Lagrangian are not physically observable parameters. These so-called bare parameters are, in fact, formally infinite, and can be renormalised to be finite at any order in perturbation theory. There are several approaches to performing the renormalisation procedure; the most common one is known as dimensional regularisation (DR) and will be the renormalisation procedure used throughout the thesis. DR involves continuing the number of spacetime dimensions to $d = 4 - 2\epsilon$, $\epsilon < 0$, and has the advantage of regulating UV and infrared (IR) divergences.

The strong coupling constant is defined as

$$\alpha_s = \frac{g_s^2}{4\pi}\,, \tag{2.13}$$

and one finds that after renormalisation, the coupling gains a scale dependence, μ. This dependence is controlled via the Renormalisation Group Equation (RGE)

$$\mu^2 \frac{\partial \alpha_s(\mu^2)}{\partial \mu^2} = \beta\left(\alpha_s(\mu^2)\right)\,, \tag{2.14}$$

where the β function can be expanded as a power expansion in α_s,

$$\beta\left(\alpha_s(\mu^2)\right) = -\alpha_s^2(\mu^2)\left(\beta_0 + \beta_1\alpha_s(\mu^2) + ...\right)\,, \tag{2.15}$$

and is known up to 5 loops [16–20]. The minus sign, for $\beta_i > 0$, is the origin of asymptotic freedom and is the reason we can perform perturbative calculations at the LHC, as the energies are high enough that α_s is sufficiently small, and we can perform a perturbative expansion in α_s. The RGE can be solved iteratively, and at lowest order, the running of α_s is given by

$$\alpha_s(\mu^2) = \frac{\alpha_s(\mu_0^2)}{1 + \beta_0 \alpha_s(\mu_0^2) \ln \frac{\mu^2}{\mu_0^2}}\,, \tag{2.16}$$

where μ_0 is some initial scale. So long as the number of active flavours, n_f, is less than 17, $\alpha_s(\mu^2)$ decreases as the scale increases, as β_0 is given by

$$\beta_0 = \frac{33 - 2n_f}{12\pi}\,. \tag{2.17}$$

We should note that this statement does not hold if we include higher order corrections; β_1 is given by

$$\beta_1 = \frac{153 - 19n_f}{24\pi^2}\,, \tag{2.18}$$

which implies that in order to ensure the minus sign in Eq. (2.15), we now require $n_f < 16$, for $\alpha_s = \alpha_s(M_Z)$, using the PDG value [21] of $\alpha_s(M_Z) = 0.1179$.

2.1.3 Collinear factorisation

The last pieces of QCD which we need to formally introduce are the PDFs. In this last section we will introduce the collinear factorisation theorem, which is used to compute theoretical predictions when initial state hadrons are present.

Deep inelastic scattering

We begin with the study of deep inelastic scattering (DIS). A DIS experiment occurs when an initial state lepton with momentum k scatters off a hadronic target, such as a proton through the exchange of a virtual boson with momentum $q = k - k'$; we will assume here that the boson is a photon for simplicity. Defining

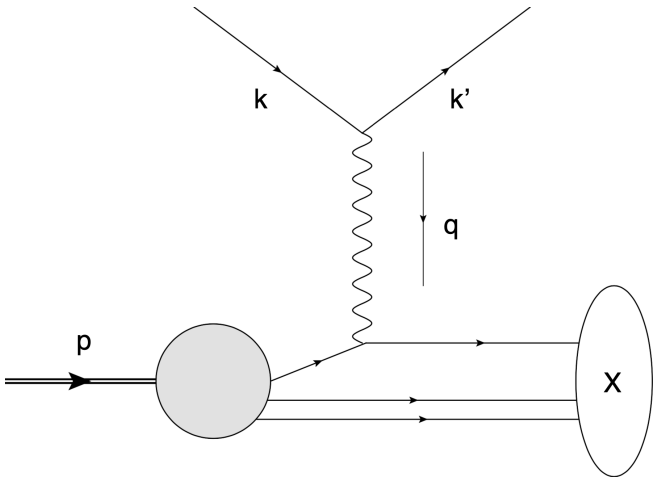

Figure 2.1: The DIS process.

$Q^2 \equiv -q^2$ and $W^2 = (p+q)^2$ allows us to define the regime for DIS in a Lorentz invariant way, by requiring Q^2 and W^2 to be large. In Fig. 2.1 we show the scattering. Defining the centre of mass energy as $s = (p+k)^2$, and working in the limit $m_p^2 \ll Q^2$, we can define two variables,

$$x = \frac{Q^2}{2p \cdot q} \qquad y = \frac{2p \cdot q}{s}\,, \tag{2.19}$$

where the x variable is known as Bjorken-x, and tells us how elastic the collision is; for $x = 0$ the collision is totally inelastic, and for $x = 1$, the collision is perfectly elastic. The variable y is the fractional energy loss of the lepton, and also can take values between 0 and 1.

It is common to write the matrix element squared as the product of two tensors; a leptonic tensor $L_{\mu\nu}$ and a hadronic tensor, $W^{\mu\nu}$,

$$|\mathcal{M}|^2 \sim L_{\mu\nu} W^{\mu\nu}\,. \tag{2.20}$$

This definition allows us to separate the leptonic contribution, which is computable in perturbation theory, from the hadronic part, which is not. Despite this, by requiring Lorentz invariance and current conservation, $q_\mu W^{\mu\nu} = q_\nu W^{\mu\nu} = 0$, it is possible to find the most general tensor structure allowed:

$$W^{\mu\nu} = \left(-g^{\mu\nu} - \frac{q^\mu q^\nu}{q^2}\right) F_1(x, Q^2) + \frac{1}{p \cdot q}\left(p^\mu - q^\mu \frac{p \cdot q}{q^2}\right)\left(p^\nu - q^\nu \frac{p \cdot q}{q^2}\right) F_2(x, Q^2)\,, \tag{2.21}$$

where the coefficients F_1 and F_2 are called structure functions. [1] It is useful to now define

$$F_L \equiv F_2 - 2xF_1 = \frac{Q^4}{(p \cdot q)^3} p^\mu p^\nu W_{\mu\nu}\,, \tag{2.22}$$

known as the longitudinal structure function.

The parton model

We have thus far only used the properties of Lorentz invariance and current conservation to try to understand DIS. In Feynman's parton model, we make an additional assumption; namely that for a sufficiently hard interaction, such that the binding energy that holds the partons inside the hadrons can be neglected, the virtual photon only interacts with a single point-like parton inside the proton [22] with momentum fraction ξ. In this model, the structure functions are a distribution in ξ rather than a delta function. Therefore, the probability of interacting with a parton carrying between ξ and $\xi + \delta\xi$ of the proton's momentum is given by $f(\xi)\delta\xi$ where $f(\xi)$ is the interaction probability for a parton with momentum ξp.

In this model, the structure functions are

$$F_2 = \sum_i 2e_i^2 x f_i(x), \quad F_L = 0\,, \tag{2.23}$$

where the sum runs over parton species and the $f_i(x)$ are the parton distribution functions, or PDFs. The second result is known as the Callan-Gross relation [23] and is due to the fact that quarks are spin-1/2 particles. We now know that the Callan-Gross relation only holds at leading order in QCD, and the parton model is a first step towards a fully perturbative QCD treatment of the proton.

[1] If we allow $Q^2 \gtrsim M_Z^2$, the Z boson can also contribute to the process, and a parity-violating structure function, F_3 would also need to be included.

In the partonic model, the structure functions have no dependence on the resolution parameter, Q^2, a phenomenon known as Bjorken scaling [24]. This scale independence is a consequence of the assumption that all the interactions are point-like and consequently have no characteristic length scale. Whilst early DIS experiments showed good agreement with the parton model, scale violations began to be observed at low Q^2 values, breaking the parton model, as we will now discuss.

Higher order corrections and factorisation

At lowest order in QCD, the point-like interaction for the subprocess $q\gamma^* \to q$ is proportional to a delta function in the structure functions, $\delta(\xi - x)$, which allows us to write them as in Eq. (2.23). At higher orders, as shown in Fig. 2.2, we have to consider additional diagrams with gluon loops and the emission of additional real gluons, which introduce logarithms of Q^2/Q_0^2 which break the Bjorken scaling.

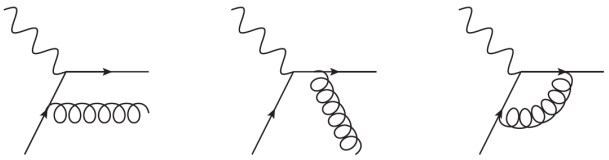

Figure 2.2: The $q\gamma^* \to q$ subprocess with a selection of the higher order real and virtual corrections.

QCD corrections have both UV and IR divergences. Whilst the UV divergences can be dealt with by renormalisation, the IR divergences arising from soft or collinear singularities cannot. These divergences cancel when the real emission diagrams are included, a result known as the KLN theorem [25, 26]. The KLN theorem states that all the singularities are cancelled provided that summation over all degenerate states is performed. Real diagrams produce IR singularities when integrating over the phase space of the emitted particles, whilst the IR divergences occur in virtual diagrams when the loop momentum probes the IR

region. By adding together the real and virtual diagrams, the KLN theorem ensures that the cross section is finite.

In addition to the final state singularities which cancel due to the KLN theorem, collinear singularities in the initial state for the process $q\gamma^* \to q$ exist and cannot be removed. This is due to the different kinematics of the real and virtual contributions in Fig. 2.2. In the initial state real emission diagram the quark carries momentum zp after emitting a gluon and in the virtual case it carries momentum p. The diagrams therefore do not cancel; it is these singularities which lead to the logarithms in Q^2. If, instead of two initial state particles, we included initial states with an arbitrary number of particles, the KLN theorem would also cancel the initial state divergence. In practice, however, we usually consider $2 \to n$ processes, and we end up with the logarithms in Q^2.

The method of dealing with the initial state collinear divergences is similar to the process of renormalisation. In the renormalisation procedure, we have the bare parameters which are formally infinite. Similarly, we treat the PDFs in Eq. (2.23) as bare PDFs, and we redefine them such that the collinear divergences can be absorbed into the physically observable quantities measured at a factorisation scale μ_F. As a consequence, all the long-distance, non-perturbative behaviour is inside the PDFs, with the cost that they gain a dependence on μ_F. The factorisation scale sets the scale at which we define the long-distance behaviour (the scale of the PDFs) from the short-distance (the hard underlying partonic interaction).

We can then define our structure functions as

$$F(x,Q^2) = \sum_i e_i^2 \left[f_i(x,\mu_F^2) + \frac{\alpha_s}{2\pi} \int_x^1 \frac{\mathrm{d}\xi}{\xi} f_j\left(\frac{x}{\xi},\mu_F^2\right) \left(P_{ij}(\xi) \log \frac{Q^2}{\mu_F^2} + R(\xi) \right) + \mathcal{O}(\alpha_s^2) \right] . \tag{2.24}$$

The P_{ij} functions are known as the Altarelli-Parisi splitting functions, which are calculable in perturbation theory:

$$P_{ij}(\xi) = \alpha_s \left(P_{ij}^{(0)}(\xi) + \alpha_s P_{ij}^{(1)}(\xi) + \alpha_s^2 P_{ij}^{(2)}(\xi) + ... \right) , \tag{2.25}$$

and are fully known up to NNLO [27,28]; parts of the N3LO splitting functions are also known [29–31]. At leading order, the splitting functions may be interpreted as the probabilities of finding a parton of type i in a parton of type j with momentum fraction ξ.

The form of $R(\xi)$ depends on the factorisation scheme, and is finite. Defining the coefficient functions C_i as the finite contributions which remain, we can write

$$F(x,Q^2) = \sum_i \int_x^1 \frac{\mathrm{d}\xi}{\xi} C_i\left(\frac{x}{\xi}, \frac{Q^2}{\mu_F^2}, \alpha_s\right) f_i(\xi, \mu_F^2)\,, \tag{2.26}$$

where the C_i are perturbatively calculable:

$$C_i(x,\alpha_s) = C_i^{(0)}(x) + \alpha_s C_i^{(1)}(x) + \alpha_s^2 C_i^{(2)}(x) + \dots\,. \tag{2.27}$$

Eq. (2.26) can be rewritten as

$$F(x,Q^2) = \sum_i C_i\left(x, \frac{Q^2}{\mu_F^2}, \alpha_s\right) \otimes f_i(x,\mu_F^2)\,, \tag{2.28}$$

where we have introduced the convolution symbol $\otimes$.

Eq. (2.26) tells us how PDFs relate to the structure functions of DIS. It is natural to ask whether this can be extended to the LHC, where we have two hadrons in the initial state; i.e.

$$h_1(p_1) + h_2(p_2) \to M(Q) + X\,, \tag{2.29}$$

where h_1 and h_2 are the hadrons, and M is the hard particle produced in the collision, with Q being the hard scale of the process (e.g. M_Z for Z production). In fact, the exact same logic applies, and in this case, the collinear factorisation theorem states that [32–35]

$$\sigma(p_1,p_2,Q) = \sum_{a,b} \int_\tau^1 \mathrm{d}x_1 \mathrm{d}x_2 f_{a/h_1}(x_1,\mu_F^2) f_{b/h_2}(x_2,\mu_F^2) \hat{\sigma}_{ab}(x_1p_1, x_2p_2, Q, \mu_F^2)\,, \tag{2.30}$$

where $\tau = Q^2/s$ and $s = (p_1+p_2)^2$ and we sum over parton flavours a, b for the two parton densities. The partonic cross section, $\hat{\sigma}_{ab}$ is equivalent to the coefficient

functions in DIS; they are computable order-by-order in perturbation theory and encapsulate the short-distance behaviour of the process.

The fact that Eqs. (2.26), (2.30) hold is highly non-trivial. We have assumed that the divergent terms in the initial state entirely factorise independently of the observable being calculated. It turns out that this strong assumption is true not only for DIS but also for Drell-Yan production, and the result is known as the collinear factorisation theorem. Although the factorisation theorem has not been proven for all processes we consider at the LHC, it is standard to take it on trust and perform theoretical calculations within the framework. Corrections to the factorisation theorem are suppressed by powers of Λ_{QCD}/Q and are inherently non-perturbative. These corrections are known as higher twist and will not be discussed in this thesis.

The PDFs in Eq. (2.30) are exactly the same as the ones in Eq. (2.28), as they are universal functions. As the PDFs are fundamentally non-perturbative, they cannot be computed from first principles within the context of perturbation theory, and therefore have to be extracted from experimental data. The beauty of the collinear factorisation theorem is that any process with sensitivity to PDFs can be used to constrain them, exactly because the PDFs are independent of the observable being measured.

DGLAP evolution

We finally must address the dependence of the PDFs on the factorisation scale. We introduced the factorisation scale by hand in order to deal with initial state divergences but the structure functions are physical, measurable quantities. Therefore the structure functions must be independent of the choice of the factorisation scale, which leads to the RGE

$$\mu_F \frac{\mathrm{d}}{\mathrm{d}\mu_{\mathrm{F}}} F(x, Q^2) = 0\,, \tag{2.31}$$

Using Eq. (2.24), we also have a RGE for the PDFs

$$\mu_F \frac{\mathrm{d}}{\mathrm{d}\mu_F} f_i(x, \mu_F^2) = \sum_j \int_x^1 \frac{\mathrm{d}z}{z} P_{ij}\left(\frac{x}{z}, \alpha_s(\mu_F^2)\right) f_j(z, \mu_F^2)\,. \tag{2.32}$$

These are the DGLAP equations [36–39], and they describe how PDFs evolve with the factorisation scale.

The DGLAP equations enable us to use experimental data at any energy scale to extract and constrain the PDFs. We can therefore use the lower energy DIS measurements for the PDFs used as input for theoretical calculations at the LHC. In addition we can use different types of measurements at the LHC itself, each of which with a different typical energy scale. Thus, with the large statistics at the LHC, as well as the large variety of processes being measured, we are able to understand PDFs at the highest level of precision we have achieved.

2.2 The Standard Model Effective Field Theory

Let us now turn to the second framework we need to introduce: the SMEFT. The essential idea of any effective field theory (EFT) is that the IR physics can be entirely separated from the UV, such that we can calculate any quantity we need in the IR, so long as limited theoretical precision is all we require. This is also true in the SM; the SM is not defined up to arbitrarily high scales due to Landau poles in the electroweak sector, as $\alpha_{EM}(Q) \to 1$ for $Q \to \infty$. Despite this, the SM has repeatedly been shown to be an accurate model of LHC data at the current level of precision. At first order, the running of α_{EM} is similar to QCD, Eq. (2.16), where now the coefficient $\beta_0 < 0$ in our convention. The Landau pole thus appears at approximately 10^{286} eV (we have assumed the only leptons are electrons for simplicity), which is well above the Planck scale of 10^{28} eV and can be safely ignored for LHC physics.

In this section we will outline the phenomenological application of the SMEFT as a model-independent way to parameterise new physics which might be observed

at the LHC. We focus in particular on the top sector of the SMEFT, and we will discuss the higher dimensional operators at mass dimension 6 which enter when top quarks are produced in hadronic collisions.

2.2.1 The SMEFT Lagrangian

The SMEFT is an EFT generalisation of the SM, constructed from its fields and symmetries and under the assumption that the the observed Higgs-like boson is embedded in the $SU(2)$ Higgs doublet. The idea of the SMEFT is that any new physics which may be observed at the LHC will involve massive particles heavier than the Higgs vacuum expectation value of 246 GeV, with the scale of new physics typically characterised by some unknown scale Λ. Under these assumptions, we can write down the Lagrangian for the SMEFT as a power expansion in powers of the operator dimension

$$\mathcal{L}_{\text{SMEFT}} = \mathcal{L}_{\text{SM}} + \sum_{i}^{N_{d5}} \frac{c_i^{(5)}}{\Lambda} \mathcal{O}_i^{(5)} + \sum_{i}^{N_{d6}} \frac{c_i^{(6)}}{\Lambda^2} \mathcal{O}_i^{(6)} + \sum_{i}^{N_{d7}} \frac{c_i^{(7)}}{\Lambda^3} \mathcal{O}_j^{(7)} + \dots , \tag{2.33}$$

where $\mathcal{L}_{\text{SM}}$ is the SM Lagrangian, and $\mathcal{O}_i^{(\mathscr{D})}$ stands for the elements of the operator basis of mass dimension $\mathscr{D}$. The $c_i^{(\mathscr{D})}$ are operator-dependent Wilson coefficients which are unconstrained by the effective field theory.

For specific UV completions, the Wilson coefficients are fully determined by the parameters of the full BSM theory in which the EFT is embedded, such as its coupling constants and masses of the particles. An in-depth discussion of the matching procedure is discussed in Ref. [40]. In the matching, the Wilson coefficients in the EFT are determined at each loop order by requiring that the S-matrices in the UV theory and EFT match at Λ. The Wilson coefficients can then be evolved down to the weak scale using their RGEs. In this thesis we will not consider specific UV complete scenarios, leaving the coefficients undetermined. They therefore need to be constrained from experimental data.

The reason we can write the EFT Lagrangian as a power expansion can be justified using a simple power counting argument.

As with any QFT, we have a generic path integral

$$Z = \int \mathcal{D}\phi \, \mathrm{e}^{iS[\phi]} \,, \tag{2.34}$$

where the EFT action is the integral of a local Lagrangian density

$$S = \int \mathrm{d}^d x \, \mathcal{L}(x) \,, \tag{2.35}$$

such that in d dimensions, the Lagrangian density has mass dimension d,

$$[\mathcal{L}(x)] = d \,. \tag{2.36}$$

The Lagrangian density is therefore composed of local, gauge invariant operators $\mathcal{O}_i^{(\mathscr{D})}$ with coefficients $c_i^{(\mathscr{D})}$,

$$\mathcal{L}(x) = \sum_i c_i^{(\mathscr{D})} \, \mathcal{O}_i^{(\mathscr{D})}(x) \,, \tag{2.37}$$

where the operators have dimension

$$\left[\mathcal{O}_i^{(\mathscr{D})}\right] = \mathscr{D} \,, \tag{2.38}$$

and the coefficients have dimension

$$\left[c_i^{(\mathscr{D})}\right] = d - \mathscr{D} \,. \tag{2.39}$$

The Lagrangian can then be rewritten in the compact form

$$\mathcal{L}_{\text{SMEFT}} = \sum_{\mathscr{D}>0,i} \frac{\tilde{c}_i^{(\mathscr{D})} \mathcal{O}_i^{(\mathscr{D})}}{\Lambda^{\mathscr{D}-d}} \,, \tag{2.40}$$

where we have explicitly introduced a scale Λ to make the Wilson coefficients dimensionless, i.e. $\tilde{c}_i^{(\mathscr{D})} = \Lambda^{\mathscr{D}-d} c_i^{(\mathscr{D})}$, and is equivalent to Eq. (2.33).

The number of operators in the SMEFT is known to all orders [9, 41–47], as are the complete bases of operators up to $\mathscr{D} = 7$ [9, 44, 45]. The operator at dimension 5 affects only the neutrinos, and gives neutrinos their masses [9]. In

this thesis we will only be interested in the top quark sector of the SMEFT, and we will restrict ourselves to looking at $\mathscr{D} = 6$ operators. Operators with $\mathscr{D} = 5$ and $\mathscr{D} = 7$ violate lepton and/or baryon number conservation [48, 49] and $\mathscr{D} = 7$ operators are additionally power suppressed with respect to $\mathscr{D} = 6$.

At the matrix element level, we can write schematically

$$|\mathcal{M}|^2 = |\mathcal{M}_{\rm SM} + \mathcal{M}_{\rm SMEFT}|^2 \tag{2.41}$$

$$= |\mathcal{M}_{\rm SM}|^2 + 2\mathbb{R}\left(\mathcal{M}_{\rm SM}\mathcal{M}_{\rm SMEFT}\right) + |\mathcal{M}_{\rm SMEFT}|^2 . \tag{2.42}$$

The content of $\mathcal{M}_{\rm SMEFT}$ depends on whether the restriction to $\mathscr{D} = 6$ operators is imposed at the Lagrangian level or the cross section level. If we drop $\mathscr{D} > 6$ operators in the Lagrangian, then we have

$$|\mathcal{M}|^2 = |\mathcal{M}_{\rm SM}|^2 + 2\mathbb{R}\left(\mathcal{M}_{\rm SM}\mathcal{M}^{(6)}_{\rm SMEFT}\right) + |\mathcal{M}^{(6)}_{\rm SMEFT}|^2 , \tag{2.43}$$

whereas, if the restriction occurs at the cross section level, neglecting $\mathscr{D} = 5, 7$, we have

$$|\mathcal{M}|^2 = |\mathcal{M}_{\rm SM}|^2 + 2\mathbb{R}\left(\mathcal{M}_{\rm SM}\mathcal{M}^{(6)}_{\rm SMEFT}\right) + |\mathcal{M}^{(6)}_{\rm SMEFT}|^2 + 2\mathbb{R}\left(\mathcal{M}_{\rm SM}\mathcal{M}^{(8)}_{\rm SMEFT}\right) + \mathcal{O}(\Lambda^{-6}) . \tag{2.44}$$

If we perform the truncation at the cross section level, Eq. (2.44), the terms at dimension-6 which arise from the squared amplitudes of the SMEFT operators should formally be neglected. They appear at the same power of Λ as dimension-8 terms and should not be included if one does not take into account the dimension-8 operators which also enter at $\mathcal{O}\left(\Lambda^{-4}\right)$. We will drop $\mathscr{D} > 6$ operators at the Lagrangian level throughout, and neglect any $\mathcal{O}\left(\Lambda^{-4}\right)$ contributions from dimension-8 operators.

Therefore, in general, the effects of the $\mathscr{D} = 6$ operators in a given observable can be written as

$$\sigma = \sigma_{\rm SM} + \sum_i^{N_{d6}} \sigma_i \frac{c_i}{\Lambda^2} + \sum_{i,j}^{N_{d6}} \widetilde{\sigma}_{ij} \frac{c_i c_j}{\Lambda^4} , \tag{2.45}$$

where σ_{SM} indicates the SM prediction and the σ_i, σ_{ij} terms are process-dependent contributions from the different operators.

By performing the power expansion truncation at the Lagrangian level, we end up with $\mathcal{O}(\Lambda^{-4})$ terms at dimension-6. This has several advantages. Firstly, operators may appear only due to the $\mathcal{O}(\Lambda^{-4})$ effects, because the amplitudes do not interfere with the SM amplitudes. Additionally, in BSM models with large couplings the $\mathcal{O}(\Lambda^{-4})$ dimension-6 terms can become dominant [50–53]. Furthermore, from a computational point of view, when designing a fitting code, there is a complication caused by requiring one to fit the dimension-6 $\mathcal{O}(\Lambda^{-4})$ terms with 2 Wilson coefficients, as we end up with a large matrix of $c_i c_j$ terms which need to be separated and assigned to the correct degrees of freedom. This means that, once a complete basis for dimension-8 is computed, it is trivial to simultaneously fit the two sets of corrections, using Eq. (2.44). We will use as a baseline the fits including the $\mathcal{O}(\Lambda^{-4})$ terms, however we will compare with results computed with just the the $\mathcal{O}(\Lambda^{-2})$ effects.

2.2.2 The top quark sector

In this thesis, we present the SMEFiT methodology [2]. This proof-of-concept work was applied to the top sector of the SMEFT and we follow the strategy documented in the LHC Top Quark Working Group note [54]. As in the note, we impose a $U(2)_q \times U(2)_u \times U(2)_d$ flavour symmetry among the first two generations; this enforces the Yukawa couplings to be nonzero only for the top and bottom quarks, leaving us with 34 operators to fit. We additionally only consider CP-conserving degrees of freedom; adding CP-violating degrees of freedom would only add 8 more.

Whilst the flavour symmetry forces the light Yukawas to be zero, it still allows interactions between heavy and light quarks; for example, the operator

$$O_{qq}^{3(ii33)} = (\bar{q}_i \gamma^\mu \tau^a q_i)(\bar{Q} \gamma_\mu \tau^a Q) \tag{2.46}$$

is permitted, where τ^a are the Pauli matrices; $q\,(Q)$ is the left-handed light (heavy) $SU(2)$ quark doublet, $(u_L^i, d_L^i)^T$, flavour indices are labelled by i, j, k and l and right-handed light (heavy) fermion singlets by $u(t)$, $d(b)$. The operators which this flavour symmetry does remove are ones which involve new right-handed charged currents in the first two generations, such as the bilinear $(\bar{u}d)$, or operators which allow chirality to flip in the first two generations, such as the bilinear $(\bar{q}d)$. This restriction is not strictly necessary; however lifting the additional symmetries and exploring how the fits change is left to future work.

We can now define the degrees of freedom which will be used in the SMEFiT code. We will use the Warsaw basis [44] throughout; the Warsaw basis was the first minimal complete basis found at dimension-6. Let us define: $T^A \equiv \lambda^A/2$ where λ^A are Gell-Mann matrices; $\varepsilon \equiv i\tau^2$; the Higgs doublet by φ; $\tilde{\varphi} = \varepsilon\varphi^*$; $(\varphi^\dagger i\overleftrightarrow{D}_\mu \varphi) \equiv \varphi^\dagger(iD_\mu\varphi) - (iD_\mu\varphi^\dagger)\varphi$; $(\varphi^\dagger i\overleftrightarrow{D}^a_\mu \varphi) \equiv \varphi^\dagger\tau^a(iD_\mu\varphi) - (iD_\mu\varphi^\dagger)\tau^a\varphi$; $\sigma^{\mu\nu} = -\frac{i}{4}[\gamma^\mu, \gamma^\nu]$.

Within our assumptions, the dimension-6 four-heavy quark operators relevant for the interpretation of top quark measurements at the LHC are the following:

$$
\begin{aligned}
O_{qq}^{1(3333)} &= (\bar{Q}\gamma^\mu Q)(\bar{Q}\gamma_\mu Q), \\
O_{qq}^{3(3333)} &= (\bar{Q}\gamma^\mu \tau^a Q)(\bar{Q}\gamma_\mu \tau^a Q), \\
O_{qu}^{1(3333)} &= (\bar{Q}\gamma^\mu Q)(\bar{t}\gamma_\mu t), \\
O_{qu}^{8(3333)} &= (\bar{Q}\gamma^\mu T^A Q)(\bar{t}\gamma_\mu T^A t), \\
O_{qd}^{1(3333)} &= (\bar{Q}\gamma^\mu Q)(\bar{b}\gamma_\mu b), \\
O_{qd}^{8(3333)} &= (\bar{Q}\gamma^\mu T^A Q)(\bar{b}\gamma_\mu T^A b), \\
O_{uu}^{(3333)} &= (\bar{t}\gamma^\mu t)(\bar{t}\gamma_\mu t), \\
O_{ud}^{1(3333)} &= (\bar{t}\gamma^\mu t)(\bar{b}\gamma_\mu b), \\
O_{ud}^{8(3333)} &= (\bar{t}\gamma^\mu T^A t)(\bar{b}\gamma_\mu T^A b), \\
{}^{\ddagger}O_{quqd}^{1(3333)} &= (\bar{Q}t)\,\varepsilon\,(\bar{Q}b), \\
{}^{\ddagger}O_{quqd}^{8(3333)} &= (\bar{Q}T^A t)\,\varepsilon\,(\bar{Q}T^A b).
\end{aligned}
\tag{2.47}
$$

The operators which give rise to two-heavy-two-light quark interactions are

$$
\begin{aligned}
O_{qq}^{1(i33i)} &= (\bar{q}_i\gamma^\mu Q)(\bar{Q}\gamma_\mu q_i),\\
O_{qq}^{1(ii33)} &= (\bar{q}_i\gamma^\mu q_i)(\bar{Q}\gamma_\mu Q),\\
O_{qq}^{3(ii33)} &= (\bar{q}_i\gamma^\mu \tau^a q_i)(\bar{Q}\gamma_\mu \tau^a Q),\\
O_{qq}^{3(i33i)} &= (\bar{q}_i\gamma^\mu \tau^a Q)(\bar{Q}\gamma_\mu \tau^a q_i),\\
O_{qu}^{1(ii33)} &= (\bar{q}_i\gamma^\mu q_i)(\bar{t}\gamma_\mu t),\\
O_{qu}^{8(ii33)} &= (\bar{q}_i\gamma^\mu T^A q_i)(\bar{t}\gamma_\mu T^A t),\\
O_{qd}^{1(33ii)} &= (\bar{Q}\gamma^\mu Q)(\bar{d}_i\gamma_\mu d_i),\\
O_{qd}^{8(33ii)} &= (\bar{Q}\gamma^\mu T^A Q)(\bar{d}_i\gamma_\mu T^A d_i),\\
O_{uu}^{(i33i)} &= (\bar{u}_i\gamma^\mu t)(\bar{t}\gamma_\mu u_i),\\
O_{uu}^{(ii33)} &= (\bar{u}_i\gamma^\mu u_i)(\bar{t}\gamma_\mu t),\\
O_{ud}^{1(33ii)} &= (\bar{t}\gamma^\mu t)(\bar{d}_i\gamma_\mu d_i),\\
O_{ud}^{8(33ii)} &= (\bar{t}\gamma^\mu T^A t)(\bar{d}_i\gamma_\mu T^A d_i)\,.
\end{aligned}
\tag{2.48}
$$

Finally, the operators that contain two quarks coupled to Higgs fields or gauge boson fields:

$$
\begin{aligned}
{}^\ddagger O_{u\varphi}^{(33)} &= \bar{Q}t\tilde{\varphi}\,(\varphi^\dagger\varphi),\\
O_{\varphi q}^{1(33)} &= (\varphi^\dagger i\overleftrightarrow{D}_\mu\varphi)(\bar{Q}\gamma^\mu Q),\\
O_{\varphi q}^{3(33)} &= (\varphi^\dagger i\overleftrightarrow{D}^a_\mu\varphi)(\bar{Q}\gamma^\mu \tau^a Q),\\
O_{\varphi u}^{(33)} &= (\varphi^\dagger i\overleftrightarrow{D}_\mu\varphi)(\bar{t}\gamma^\mu t),\\
{}^\ddagger O_{\varphi ud}^{(33)} &= (\tilde{\varphi}^\dagger iD_\mu\varphi)(\bar{t}\gamma^\mu b),\\
{}^\ddagger O_{uW}^{(33)} &= (\bar{Q}\sigma^{\mu\nu}\tau^a t)\,\tilde{\varphi}W^a_{\mu\nu},\\
{}^\ddagger O_{dW}^{(33)} &= (\bar{Q}\sigma^{\mu\nu}\tau^a b)\,\varphi W^a_{\mu\nu},\\
{}^\ddagger O_{uB}^{(33)} &= (\bar{Q}_i\sigma^{\mu\nu} t)\,\tilde{\varphi}B_{\mu\nu},\\
{}^\ddagger O_{uG}^{(33)} &= (\bar{Q}\sigma^{\mu\nu}T^A t)\,\tilde{\varphi}F^a_{\mu\nu}\,,
\end{aligned}
\tag{2.49}
$$

where $W^a_{\mu\nu}$ and $B_{\mu\nu}$ are the field-strength tensors of the electroweak interaction

$$B_{\mu\nu} = \partial_\mu B_\nu - \partial_\nu B_\mu \,, \tag{2.50}$$

$$W^a_{\mu\nu} = \partial_\mu A^a_\nu - \partial_\nu A^a_\mu - g\varepsilon^{abc} A^b_\mu A^c_\nu \,, \tag{2.51}$$

and $F^a_{\mu\nu}$ is the QCD one, Eq. (2.4).

In Eqns. (2.47) and (2.49), non-Hermitian operators are indicated with a double dagger symbol. Complex conjugation is the same as the transposition of generation indices: $O^{(ij)*} = O^{(ji)}$ and by extension, for four-fermion operators, $O^{(ijkl)*} = O^{(jilk)}$.

The degrees of freedom c that we fit are defined in terms of the coefficients C in the Warsaw basis. We show in Table 2.1 the degrees of freedom we consider. We note that some of the degrees of freedom are defined as linear combinations of Warsaw basis coefficients. This is because these linear combinations are the ones which appear in the interferences with the SM amplitudes, and are therefore more easily constrained by experimental data. We will mention in Sec. 5.4 that it is a non-trivial task to project onto the Warsaw basis from a more natural basis relevant for phenomenological studies. It is therefore reasonable to ask whether there exists a more natural basis to use where these linear combinations of operators are independent of one another. Showing results in the Warsaw basis is done purely for convention as it is the most commonly used basis; in Ref. [55], bounds are shown also in the SILH basis [56, 57], so it is possible to convert our bounds into other bases.

The first grouping in Table 2.1, $QQQQ$, denotes degrees of freedom which involve four-heavy quarks. These operators can only be constrained from processes involving four-heavy quarks in the final state, such as $t\bar{t}t\bar{t}$ production or $t\bar{t}b\bar{b}$ production. The next group involves two-light quarks and two-heavy quarks. Inclusive $t\bar{t}$ and $t\bar{t}$ associated production can be used to constrain these $QQqq$ operators. The final group involves heavy quarks in association with bosons. These operators can be constrained either by single top production, or processes such

as $t\bar{t}V$ and tV. The degree of freedom $c_{t\varphi}$ can be constrained from cross section measurements for $t\bar{t}H$ production. We finally note that, as we only consider CP-conserving operators, we drop the imaginary parts of several degrees of freedom, as they are CP-violating.

RG running and mixing

A final point to note is that in general, the SMEFT operators will run with the scale and thus the coefficients c_i will depend on the typical momentum transfer of the process. This dependence can be evaluated using RGEs [58–60]. We will, however, ignore these effects, as we will only look at the top sector and therefore at processes with a similar energy scale, $E \simeq m_t$. Furthermore, we use NLO QCD for all SMEFT amplitudes where available [61–67] and it has been shown that including NLO corrections reduces the scale dependence [65, 68], even for differential distributions where significantly different scales are involved. In [65], RGE effects are calculated for $t\bar{t}H$ production over a scale ranging from 150 GeV to 2 TeV and it is found that RGE effects remain below the 10% level.

2.2.3 Fits of the Wilson coefficients

As discussed above, the Wilson coefficients in Eq. (2.33) are, when not considering specific UV completions, completely free parameters. In order to find potential areas of BSM physics, we therefore need to fit the coefficients using experimental data. As there is a huge number of parameters to fit, fitting groups often will limit themselves to particular sectors of interest in BSM physics, such as the top or Higgs sectors. The issue with doing this is that it can induce correlations between the coefficients, despite the fact that they are linearly independent. This is because by not considering the full parameter space, it may not be possible to fully distinguish between different operators as they may appear in amplitudes as

Class	Notation	Degree of Freedom	Operator Definition
$QQQQ$	OQQ1	c^1_{QQ}	$2C^{1(3333)}_{qq} - \frac{2}{3}C^{3(3333)}_{qq}$
	OQQ8	c^8_{QQ}	$8C^{3(3333)}_{qq}$
	OQt1	c^1_{Qt}	$C^{1(3333)}_{qu}$
	OQt8	c^8_{Qt}	$C^{8(3333)}_{qu}$
	OQb1	c^1_{Qb}	$C^{1(3333)}_{qd}$
	OQb8	c^8_{Qb}	$C^{8(3333)}_{qd}$
	Ott1	c^1_{tt}	$C^{(3333)}_{uu}$
	Otb1	c^1_{tb}	$C^{1(3333)}_{ud}$
	Otb8	c^8_{tb}	$C^{8(3333)}_{ud}$
	OQtQb1	c^1_{QtQb}	$\mathrm{Re}\{C^{1(3333)}_{quqd}\}$
	OQtQb8	c^8_{QtQb}	$\mathrm{Re}\{C^{8(3333)}_{quqd}\}$
$QQqq$	O81qq	$c^{1,8}_{Qq}$	$C^{1(i33i)}_{qq} + 3C^{3(i33i)}_{qq}$
	O11qq	$c^{1,1}_{Qq}$	$C^{1(ii33)}_{qq} + \frac{1}{6}C^{1(i33i)}_{qq} + \frac{1}{2}C^{3(i33i)}_{qq}$
	O83qq	$c^{3,8}_{Qq}$	$C^{1(i33i)}_{qq} - C^{3(i33i)}_{qq}$
	O13qq	$c^{3,1}_{Qq}$	$C^{3(ii33)}_{qq} + \frac{1}{6}(C^{1(i33i)}_{qq} - C^{3(i33i)}_{qq})$
	O8qt	c^8_{tq}	$C^{8(ii33)}_{qu}$
	O1qt	c^1_{tq}	$C^{1(ii33)}_{qu}$
	O8ut	c^8_{tu}	$2C^{(i33i)}_{uu}$
	O1ut	c^1_{tu}	$C^{(ii33)}_{uu} + \frac{1}{3}C^{(i33i)}_{uu}$
	O8qu	c^8_{Qu}	$C^{8(33ii)}_{qu}$
	O1qu	c^1_{Qu}	$C^{1(33ii)}_{qu}$
	O8dt	c^8_{td}	$C^{8(33ii)}_{ud}$
	O1dt	c^1_{td}	$C^{1(33ii)}_{ud}$
	O8qd	c^8_{Qd}	$C^{8(33ii)}_{qd}$
	O1qd	c^1_{Qd}	$C^{1(33ii)}_{qd}$
$QQ + V, G, \varphi$	OtG	c_{tG}	$\mathrm{Re}\{C^{(33)}_{uG}\}$
	OtW	c_{tW}	$\mathrm{Re}\{C^{(33)}_{uW}\}$
	ObW	c_{bW}	$\mathrm{Re}\{C^{(33)}_{dW}\}$
	OtZ	c_{tZ}	$\mathrm{Re}\{-\sin\theta_W C^{(33)}_{uB} + \cos\theta_W C^{(33)}_{uW}\}$
	Off	$c_{\varphi tb}$	$\mathrm{Re}\{C^{(33)}_{\varphi ud}\}$
	Ofq3	$c^3_{\varphi Q}$	$C^{3(33)}_{\varphi q}$
	OpQM	$c^-_{\varphi Q}$	$C^{1(33)}_{\varphi q} - C^{3(33)}_{\varphi q}$
	Opt	$c_{\varphi t}$	$C^{(33)}_{\varphi u}$
	Otp	$c_{t\varphi}$	$\mathrm{Re}\{C^{(33)}_{u\varphi}\}$

Table 2.1: The internal notation for the degrees of freedom and the corresponding definition in terms of the operators in the Warsaw basis.

linear combinations. For example, in the top sector, the operator

$$O_{\varphi q}^{3(33)} = (\varphi^\dagger i\overleftrightarrow{D}^a_\mu \varphi)(\bar{Q}\gamma^\mu \tau^a Q)\,, \tag{2.52}$$

only appears in linear combination with the operator

$$O_{\varphi q}^{1(33)} = (\varphi^\dagger i\overleftrightarrow{D}_\mu \varphi)(\bar{Q}\gamma^\mu Q)\,, \tag{2.53}$$

when modifying the SM coupling of the b quark to the Z, but the two operators can be individually determined by also fitting single top production and single top production in association with a W or Z.

There are many fitting groups who focus on different sectors. The top sector has been analysed by many different groups [65, 66, 69–73]. In particular, the TopFitter [74–77] and Sfitter [78, 79] groups have presented broad analyses of the top sector; the former group use the `PROFESSOR` [80] framework and the latter implement a Monte Carlo methodology for fitting. Several groups have performed fits to the electroweak precision observables (EWPO) or Higgs data, such as Gfitter [81], Zfitter [82] and HEPFit [83]. Sfitter have [84] performed non-marginalised (i.e., ignoring correlations between operators) fits to the EWPO and Higgs data simultaneously. Furthermore, in [55, 85], combined fits of EWPO, Higgs and diboson data were performed. In the flavour sector, the `smelli` code [86] provides the global likelihood for combined EWPO and flavour observables. Importantly, as they combine sectors with typical scales above and below the electroweak scale, they include the RG running of the Wilson coefficients.

In order to be able to perform global fits to the SMEFT, one needs to be able to combine data from many different sectors, such as the top and Higgs sectors. We should now be looking to build SMEFT analyses which are able to combine as many of the sectors as possible in order to do fully global fits. The limiting factor in doing so is the lack of a flexible and robust fitting methodology which scales easily with the number of parameters which need to be fitted. We will introduce in Chapter 4 the SMEFiT code, which was designed with this flexibility in mind,

as well as the ability to rigourously test the code methodology. In Chapter 5 we apply SMEFiT to the top sector.

CHAPTER 3

Determination of α_s from PDFs

In this chapter we introduce the NNPDF3.1 fit of α_s using the correlated replica method. In Sec. 3.2 we will discuss in detail both the correlated replica method, and the various methodological tools that were developed for this work, in order to compute a robust estimate of α_s and its uncertainty. We present the best-fit result in Sec. 3.3. We also discuss the impact on the central result of the various algorithms discussed in Sec. 3.2, and propagate the results into an estimate of the methodological uncertainty.

3.1 Introduction

The strong coupling constant, Eq. (2.13) is a required input to any theoretical calculation in perturbative QCD. It enters the calculation explicitly in the partonic cross sections as well as in the PDFs, due to the factorisation scale dependence caused by initial-state collinear divergences. A precise measurement of α_s is therefore deeply relevant for precision phenomenology at the LHC, however its value is a dominant source of uncertainty in, for example, Higgs production

cross sections [87]. Whilst the precision of partonic cross sections and PDFs has improved, the uncertainty on the α_s PDG average [21] remains substantially unchanged since 2010 [88].

The PDG determination of α_s is based on e^+e^- hadronic annihilation, electroweak precision fits, PDFs, and lattice computations, amongst others. The determination using the global electroweak fit [89] has the advantage that it has no dependence on the PDFs and is a very clean determination [90, 91], as there is no need to control for the parameterisation bias in PDFs which propagate onto the value of α_s. The other observables require additional models to be used, such as the lattice calculations used, Monte Carlo models, or, of course, the parameterisation of the PDFs. There is an advantage, however, of determining α_s with the PDFs, and that is due to the very large number of data points which enter a global PDF fit. The data points are from a wide range of different hadronic processes, and therefore uncertainties which may be correlated within a specific measurement are mostly uncorrelated with others. The main exception to this is the uncertainty on the luminosity at ATLAS and CMS, which is fully correlated amongst measurements taken at the same luminosity. This means that, whilst there may be an issue either with the theoretical prediction or the experimental measurement itself, in a combined fit to α_s and the PDFs, these will to some extent average out in the final result. Determinations of α_s using specific measurements, e.g. [92–98] will not have this advantage.

In this chapter we present a determination of α_s based on NNPDF3.1 [15], the most recent NNPDF set, and for the first time we use NNLO QCD theory for all predictions. This updates a previous determination of α_s [99, 100] based on NNPDF2.1 [101, 102]. The main advantage of the new determination is a new method, which we denote the correlated replica method. With the correlated replica method, both α_s and PDFs are determined from a simultaneous minimisation in their combined parameter space. This propagates all the components of the uncertainty on the PDFs into the result for α_s, including the

full experimental uncertainty on the data, and the uncertainty induced by the PDF fitting methodology. The previous determinations [99, 100] only accounted for effects in the central PDF, not on the error replicas and can lead to an underestimate of the uncertainty in α_s.

Using this strategy, α_s can be treated like any other quantity that depends on the PDFs. This allows for a determination of α_s with accurate experimental uncertainties, and negligible methodological uncertainties. We will discuss in detail the different types of methodological uncertainties which enter the α_s fit, as well as how we quantify their size. In this analysis we do not aim to accurately estimate theoretical uncertainties. We provide a conservative estimate of missing higher-order uncertainties (MHOUs), caused by the truncation of the perturbative expansion at NNLO. The inclusion of MHOUs in PDFs has only very recently been studied, and after this work was published [103, 104]; furthermore we do not attempt to estimate any other sources of theoretical uncertainty, such as higher twist effects, nuclear corrections and so on.

3.2 Fitting methodology

In this section we will briefly summarise the relevant aspects of the NNPDF methodology needed for the α_s fit; the full methodology is discussed in detail in the original literature [15]. We will then describe the main idea of the correlated replica method as well as the various methods developed to estimate finite size uncertainties.

3.2.1 NNPDF methodology

To perform a fit within the NNPDF methodology, we sample $N_{\rm rep}$ replicas from the probability distribution which describes the experimental data. These samples are called pseudodata replicas, and are simply Monte Carlo replicas of the original

data. Specifically, starting with $N_{\rm dat}$-component vector of experimental points D with components D_i, a set of $N_{\rm rep}$ replicas $D^{(k)}$ of the data is generated as

$$D_i^{(k)} = \left(1 + r_i^{{\rm nor},k}\sigma_i^{\rm nor}\right)\left(D_i + \sum_{p=1}^{N_{\rm sys}} r_{i,p}^{{\rm sys},k}\sigma_{i,p}^{\rm sys} + r_i^{{\rm stat},k}\sigma_i^{\rm stat}\right), \quad i = 1,\ldots,N_{\rm dat}\,, \tag{3.1}$$

where $k = 1,\ldots,N_{\rm rep}$; $\sigma_i^{\rm nor}$, $\sigma_i^{\rm sys}$ and $\sigma_i^{\rm stat}$ are normalisation, systematic and statistical uncertainties, and r_i are random numbers such that statistics over the replica sample reproduces the original statistical properties of the data in the limit of large $N_{\rm rep}$.

A PDF replica is then fitted to each data replica $D^{(k)}$. In the NNPDF approach, PDFs are parametrised using neural networks, in turn specified by a vector of parameters θ, henceforth called the PDF parameters. Thus, for each data replica $D^{(k)}$ a best-fit $\theta^{(k)}$ is found by minimising the χ^2

$$\chi^{2,(k)}(\{\theta\}, D, \alpha_s) = \frac{1}{N_{\rm dat}}\sum_{i,j}(T_i[\{\theta\},\alpha_s] - D_i^{(k)})\,C_{ij}^{-1}\,(T_j[\{\theta\},\alpha_s] - D_j^{(k)})\,. \tag{3.2}$$

Here, $T_i[\{\theta\},\alpha_s]$ is the theoretical prediction for the i-th datapoint and C is the covariance matrix used in the fit.

In order to not fit statistical fluctuations, a cross-validation procedure is used to avoid overfitting during the minimisation of the χ^2 [105]. The fitting procedure then consists of finding a minimum as

$$\chi^{2(k)}_{\rm min}[D,\alpha_s] = {\rm cv}\min_{f(\{\theta\})}\chi^{2(k)}[f(\{\theta\}),\alpha_s,D]|_{\alpha_s,D}\,, \tag{3.3}$$

or, equivalently,

$$\theta^{{\rm min}(k)} = {\rm cv}\,\arg\min[\chi^2(\{\theta\},D^{(k)})]\,, \tag{3.4}$$

where $f(\{\theta\})$ is the set of PDF replicas, and we retrieve the PDF replica that minimises the χ^2. The value of α_s and the data replica D is kept fixed during the minimisation. For each replica, the data is randomly split with equal probability into two disjoint sets, known as the training and validation sets where the random assignment of the data points is different for each replica. Only the training set is

used to compute the χ^2, while the data points in the validation set are monitored alongside the fit. The optimal stopping point of the fit is reached when the χ^2 evaluated on the validation set starts to increase. This is not equivalent to the absolute minimum of the error function evaluated on the training set. The function cv arg min means that the right hand side corresponds to the argument of the function (i.e. the values of θ) which minimises the χ^2 (through cross-validation).

The Monte Carlo approach used by NNPDF allows us to compute the central PDF replica as the mean over all replicas, and the PDF uncertainty is the standard deviation over replicas

$$f_0 = \langle f(\{\theta^{(k)}\})\rangle_k \quad k = 1, \ldots, N_{\text{rep}}\,, \tag{3.5}$$

$$\sigma_f = \text{std}\left(f(\{\theta^{(k)}\}\right)_k \quad k = 1, \ldots, N_{\text{rep}}\,. \tag{3.6}$$

In short, the NNPDF methodology produces a set of replicas $D^{(k)}$ of the original data, and uses them to construct a set of PDF replicas which correspond to parameters $\theta^{(k)}$. Furthermore, α_s and the quark masses at a given renormalisation scale, as well as the CKM matrix elements, are treated as fixed parameters.

3.2.2 The correlated replica method

In previous work [99, 100] by NNPDF (henceforth, the $\Delta\chi^2 = 1$ method), α_s was determined by producing PDF fits for a range of values of α_s. The χ^2 was found by taking the mean over all PDF replicas, and fitting a parabola as a function of α_s. The value of α_s was therefore the minimum of this parabola, and the error on α_s was the $\Delta\chi^2 = 1$ interval, or one sigma variation.

The downside to this methodology is that in the NNPDF procedure, the PDF uncertainty is determined from statistics over the replica sample, so a one sigma interval is determined by computing a standard deviation over replicas, Eq. (3.6). Whether or not this corresponds exactly to a $\Delta\chi^2 = 1$ interval is unclear. In fact, in some PDF determinations, the $\Delta\chi^2 = 1$ criterion is modified

by a suitable tolerance factor [106–108] when determining the PDF uncertainty. This tolerance factor then accounts for data inconsistencies or parametrisation bias. It is certainly possible that PDF uncertainties estimated in the NNPDF fits also include such a tolerance and therefore estimating the error on α_s as the $\Delta\chi^2 = 1$ interval may be inadequate.

What we would like to be able to do is to determine α_s so that is on the same footing as the PDF parameters and to perform the minimisation with respect to both α_s and θ. This then enables us to also elevate the uncertainty on α_s to be on the same footing as the PDF uncertainty, allowing us to properly estimate the probability distribution for α_s, marginalised with respect to the PDF parameters. This is actually quite difficult to do within the NNPDF framework, precisely because α_s appears within all of the theoretical predictions which enter the PDF fit. In order to maximise computational efficiency, all theoretical predictions are stored on grids called `APFELGRIDS` [109, 110] which are stored with fixed values of α_s. We therefore cannot make α_s a free parameter in the fit, as the partonic cross sections and coefficient functions are fixed.

To circumvent this problem, we use the correlated replica (or c-replica) method. The central idea of the correlated replica method is to find α_s by minimising the error function Eq. (3.3)

$$\alpha_s^{\min(k)}[D] = \arg\min_{\alpha_s} \chi^2[\alpha_s, D]\,. \tag{3.7}$$

Note that, unlike Eq. (3.4), we do want to find the absolute minimum value of the χ^2. The best-fit PDF parameters have to be found using cross-validation in order to avoid over-fitting. In this case, however, we are only looking for a single parameter, rather than a function, and therefore we do not use cross-validation. This means that in practice, $\alpha_s^{\min(k)}$ can be found by fitting a parabola to the discrete values of the χ^2, now for each PDF replica, and finding the minimum. We will discuss this point further in Sec. 3.3.1. Note that, as α_s is placed on the same footing as the PDF parameters, the minimisation is now over a larger parameter

space. As we are not able to directly perform fits in the (θ, α_s) space because we are not able to make α_s a free parameter, we instead perform multiple fits scanning across a range of values of α_s. We therefore end up with a $N_\alpha \times N_{\rm rep}$ table, where α is the number of α_s values scanned over, and rep the number of data replicas. The novel idea is that the same set of data replicas, D, is used as we scan across different values of α_s to find a minimum, hence the name correlated replicas.

We should note that determining the best-fit for the k-th correlated replica by first minimising with respect to θ and then minimising with respect to α_s is equivalent to simultaneously minimising in the (θ, α_s) space, so long as the same error function is used throughout. The absolute minimum in the (θ, α_s) space is the solution to the coupled equations

$$\frac{\partial}{\partial\theta}\chi^2(\alpha_s,\theta) = 0\,, \tag{3.8}$$

$$\frac{\partial}{\partial\alpha_s}\chi^2(\alpha_s,\theta) = 0\,. \tag{3.9}$$

This solution can also be found by first finding the solution $\theta(\alpha_s)$ to Eq. (3.8), determining $\chi^2(\alpha_s) = \chi^2(\alpha_s, \theta(\alpha_s))$, and solving

$$\frac{d}{d\alpha_s}\chi^2(\alpha_s) = \left(\frac{\partial}{\partial\alpha_s} + \frac{\partial\theta}{\partial\alpha_s}\frac{\partial}{\partial\theta}\right)\chi^2(\alpha_s,\theta) = 0\,. \tag{3.10}$$

This two stage procedure yields the same solution as the coupled Eqs. (3.8)–(3.9) because the second term in brackets on the r.h.s. of Eq. (3.10) vanishes since $\theta(\alpha_s)$ was the solution of Eq. (3.8).

One thus ends up, for each data replica $D^{(k)}$, with a best-fit value $(\theta^{\min(k)}, \alpha_s^{\min(k)})$ of both α_s and the PDF parameters. This ensemble of $\alpha_s^{\min(k)}$ values then provides a Monte Carlo representation of the probability distribution of α_s, just as in the case of standard NNPDF fits for $\theta^{\min(k)}$.

3.2.3 Implementation

In this section we will discuss how we implement the correlated replica method using parabolic fitting of the χ^2. We will then describe how we estimate finite

size effects due to a limited number of data replicas, and finally, we will see how we deal with the fact that not all data replicas converge during the minimisation, leading to undefined entries in the $N_\alpha \times N_{\text{rep}}$ table.

Fitting the error function

We mentioned above that we can use a parabola to find the minimum of the error function for each replica, k,

$$\chi^{2(k,\alpha)} = \chi^2_{\text{min}}\left[\alpha, D_k\right] , \tag{3.11}$$

for each α_s value, α. We can therefore determine $\chi^{2(k,\alpha_s)}$ performing a quadratic fit to the discrete set of values N_α used and find the minimum of the curve for each replica. We then end up with a set of parabolas

$$\chi^{2,(k)}(\alpha_s) = A^{(k)}\left[\alpha_s - \alpha_s^{\min(k)}\right]^2 + B^{(k)} . \tag{3.12}$$

We can then determine $\alpha_s^{\min(k)}$, the minimum of the parabola, as the best value of α_s for the $k-$th replica. What we end up with is a set of $\{\alpha_s^{\min(k)}\}$, which describe the fluctuations on α_s caused by fluctuations in the data, propagating the PDF uncertainty onto α_s.

Finite size effects

One source of uncertainty is due to the finite size effects due to a limited number of replicas. We can in principle remove this uncertainty by producing a very large number of replicas as the finite size uncertainty is purely due to limited computational resources. As we cannot in fact produce an unlimited number of replicas, we instead estimate the uncertainty using a case resampling bootstrapping procedure, with the sample being the set of replicas [111]. Bootstrapping entails constructing a large number $N_{\text{resamples}}$ of resamples with replacement of the original set of replicas (i.e. the original sample, $\{\alpha_s^{\min(k)}\}$), where each resample is of size N_{rep}. In other words, each resample is obtained by picking replicas at random,

allowing replicas to appear multiple times in the resample until each one is of size $N_{\rm rep}$. We can then estimate the finite size uncertainty by first computing the central value of α_s for each resample m,

$$\alpha_s^{(\text{central},m)} = \left\langle \{\alpha_s^{\min(k)}\} \right\rangle_k \quad k = 1, \ldots, N_{\rm rep}\,. \tag{3.13}$$

The finite size uncertainty on α_s is then obtained as the standard deviation over the set of resamples

$$\Delta_{\alpha_s} = \text{std}\left(\left\langle \{\alpha_s^{\min(k),m}\} \right\rangle_k \right)_m \quad k = 1, \ldots, N_{\rm rep} \quad m = 1, \ldots, N_{\rm resamples}\,. \tag{3.14}$$

The finite size uncertainty on the α_s uncertainty Δ_σ can be similarly computed by first determining the standard deviation over replicas for each resample

$$\sigma_\alpha^{(\text{resamples},m)} = \text{std}\left(\{\alpha_s^{\min(k),m}\} \right)_k \quad k = 1, \ldots, N_{\rm rep}\,, \tag{3.15}$$

which is the α_s uncertainty for each resample, and then computing the standard deviation of the ensuing uncertainties

$$\Delta_\sigma = \text{std}\left(\text{std}\left(\{\alpha_s^{\min(k),m}\} \right)_k \right)_m \quad k = 1, \ldots, N_{\rm rep} \quad m = 1, \ldots, N_{\rm resamples} \tag{3.16}$$

$$= \text{std}\left(\sigma_\alpha^{(\text{resamples},m)} \right)_m \quad m = 1, \ldots, N_{\rm resamples}\,. \tag{3.17}$$

We find that results become independent of the random seed up to the first two significative figures in the uncertainties Eqs. (3.14)-(3.16) used to generate the bootstrapping resamples when $N_{\rm resamples} = 10000$. We use the finite size uncertainties on the mean, Eq. (3.14), as a way to determine how many replicas are needed to determine α_s, in order to ensure that PDF uncertainties dominate. The uncertainty on the uncertainty, Eq. (3.16) is used in order to determine which replicas should be discarded as outliers, which we will discuss below.

Batch minimisation

When determining the best-fit PDF parameters in the NNPDF methodology, there is an observed dependence on the random seed used in the minimisation, causing

fluctuations in the parabolic fits to the error function. This means that some of the χ^2 parabolas are not very smooth – it is therefore advantageous to introduce an algorithm, called batch minimisation, to help smooth the parabolic fits.

The idea of batch minimisation is to construct several sets of fits (batches), $f_{(1)}^{(\alpha,k)}, f_{(2)}^{(\alpha,k)}$, which differ only in the random seeds used in the minimisation, but the pseudodata is exactly the same. We can then compare the batches

$$f^{(\alpha,k)} = \min_{\left\{f_{(1)}^{(\alpha,k)}, f_{(2)}^{(\alpha,k)}\right\}} \left\{ \chi^{2(\alpha,k)}\left[f_{(1)}^{(\alpha,k)}\right], \chi^{2(\alpha,k)}\left[f_{(2)}^{(\alpha,k)}\right] \right\} \tag{3.18}$$

and, for each replica, pick the batch which minimises the error function. We also require that at least two of the batches for a given replica have converged under the NNPDF requirements, in order mitigate the influence of outliers that only just pass the NNPDF criteria (see Sec. 3.3.2 of Ref. [105]), which require that the PDFs are positive, that the fit has converged, and that the χ^2 to the data for each replica is satisfactory. Note that this can extend to an arbitrary number of batches, but we still require at least two replicas from two batches to have passed. We will discuss in Sec. 3.3.2 the impact of the results on the number of batches used.

Replica selection

After batch minimisation, we may still end up with a set of replicas where some of the α_s values are missing, because all batches failed to pass the NNPDF criteria and there is therefore a reduced number of points with which to do the parabolic fitting. A given curve for fitting is kept, only if the number of α_s values for which the replica has passed the fit criteria is larger than some threshold $N_{\min}$. We must therefore determine the threshold $N_{\min}$. Let us denote by N_{curves} the number of replicas which pass the selection criteria. Curves with too few points in α_s lead to an unreliable parabolic fit, and consequently, an unreliable determination of α_s for that replica. This leads to outlier values of $\alpha_s^{\min(k)}$ and the uncertainty on the determination is spuriously large. Requiring a curve to have many points, however, reduces the number of replicas which are retained, leading to a large finite size

uncertainty. The number of points required is therefore a trade-off between the uncertainty on α_s from parabolic fitting, and the finite size uncertainty.

To assess the influence of outliers, and determine $N_{\min}$, we minimise the bootstrapping estimate of the finite size effects on the α_s uncertainty Δ_σ Eq. (3.16). We expect the uncertainty to decrease when increasing the number of allowed curves. However $N_{\min}$ controls the trade-off between outliers allowed in the distribution and size of the sample. Specifically, we minimise Δ_σ (and not Eq. (3.14)) because an increase in Δ_σ despite allowing curves with fewer points (i.e., increasing the number of curves), is a clear indication that the sample is contaminated with poorly fitted parabolas, warranting a tighter selection by increasing $N_{\min}$. Eq. (3.14) simply tells us that we have sufficient statistics that the χ^2 profiles of α_s are smooth; in order to ensure the standard deviation of α_s is reliable (i.e., not contaminated by outliers), we need to minimise the finite size effects on the α_s uncertainty.

In order to allow for the fact that having too tight a selection criteria means we end up with fewer curves which are themselves affected by large statistical uncertainties, we do not minimise Δ_σ itself. We multiply Δ_σ by a penalty factor that depends on the number of points, determined as the 99% confidence level factor from a two sided Student-t distribution. Multiplying by the penalty factor minimises the effects of outliers being used in the final determination of α_s. The Student-t distribution is defined as a probability distribution which arises when estimating the mean of a distribution (in our case, the estimate calculated using the resamples, Eq. (3.19)), with unknown standard distribution. We use a Student-t distribution, as the difference between the bootstrapped sampled central value

$$\left\langle \sigma_\alpha^{(\text{resamples},m)} \right\rangle_m \quad m = 1, \ldots, N_{\text{resamples}}\,; \tag{3.19}$$

which is the mean over resamples of Eq. (3.15), and the true central value for the standard deviation, follows a Student-t distribution with $N_{\text{curves}} - 1$ degrees of freedom, zero mean and scale parameter $\sigma = \Delta_\sigma / \sqrt{N_{\text{curves}}}$.

A given confidence level around the mean is equal to the standard deviation $\Delta_\sigma T_{\mathrm{CL},(N_{\mathrm{curves}}-1)}$, where $T_{\mathrm{CL},N}$ is the percentile at CL confidence level for the two-sided confidence factor of the Student-t distribution with N degrees of freedom. We choose a 99% confidence level, and we determine N_{min} as

$$N_{\mathrm{min}} = \arg\min \Delta_\sigma T_{0.99,(N_{\mathrm{curves}}-1)} \,. \tag{3.20}$$

We will discuss in Sec. 3.3.2 the impact of the precise settings of the selection criteria on the final determination of α_s.

Final equations

We can finally specify how we determine α_s and its uncertainty in the correlated replica approach. For each curve which passes all the selection criteria, the central value of α_s is

$$\alpha_s = \langle \alpha_s^{(k)} \rangle_k \quad k = 1, \ldots, N_{\mathrm{curves}} \,, \tag{3.21}$$

and the α_s uncertainty is

$$\sigma_\alpha = \mathrm{std}\left(\alpha_s^{(k)}\right)_k \quad k = 1, \ldots, N_{\mathrm{curves}} \,. \tag{3.22}$$

3.3 The strong coupling constant from NNPDF3.1

We can now present the determination of α_s based on the methodology discussed in Sec. 3.2. It is standard practice to quote the value of α_s at some scale, as it can be determined at any other scale using its RGE Eq. (2.16). The PDG quotes $\alpha_s(M_Z)$ [21], therefore we will accordingly determine α_s at the Z mass. We will first present the best-fit result for $\alpha_s(M_Z)$ determined through the correlated replica method. We then discuss methodological and theoretical uncertainties. We finally collect our final result and briefly compare it to other recent determinations from PDF fits and to the PDG average.

3.3.1 Results

The PDF fits we use for the $\alpha_s(M_Z)$ determination are similar to those used in the NNPDF3.1 analysis [15], with one difference. The inclusive jet production datasets are now computed using exact NNLO theory [112] for the ATLAS [113] and CMS [114] inclusive jet measurements at 7 TeV. All other jet datasets in NNPDF3.1 which are not available at NNLO are discarded.

We generate 400 data replicas, from which we generate a set of 400 c-replicas, each with 21 values of α_s, corresponding to a total of 8400 PDF replicas. The c-replicas are generated for $\alpha_s(M_Z)$ ranging between 0.106 and 0.130, varied in steps of $\Delta_{\alpha_s} = 0.002$ between 0.106 and 0.112 and between 0.128 and 0.130, and in steps of $\Delta_{\alpha_s} = 0.001$ between 0.112 and 0.128, adding up to the total of 21 values.

At NNLO we find

$$\alpha_s^{\rm NNLO}(m_Z) = 0.11845 \pm 0.0005^{\alpha_s}\ (0.4\%)\,. \tag{3.23}$$

This result is based on a total of $N_{\rm curves} = 379$ c-replicas after batch minimisation of three batches, using the minimisation and selection methods described in Sec. 3.2.3. At NLO we find

$$\alpha_s^{\rm NLO}(m_Z) = 0.12067 \pm 0.0006^{\alpha_s}\ (0.5\%)\,. \tag{3.24}$$

In this case, the sample includes $N_{\rm curves} = 108$ c-replicas selected after batch minimisation with two batches. The smaller number of c-replicas selected at NLO is explained by the requirement (see Sec. 3.2.3) that two batches have converged for the given α_s value, which is of course less severe when three batches are available.

The 379 c-replicas selected for the NNLO determination are shown in Fig 3.1. Each curve shows the error function as a function of $\alpha_s(M_Z)$ obtained by combining the three batches. The colour scale of each curve indicates the best-fit $\alpha_s^{\min(k)}(M_Z)$ value for each replica, Eq. (3.7). The probability distributions at NLO and NNLO are shown in Fig. 3.2, where the markers indicate the value of $\alpha_s^{(k)}(M_Z)$ for each

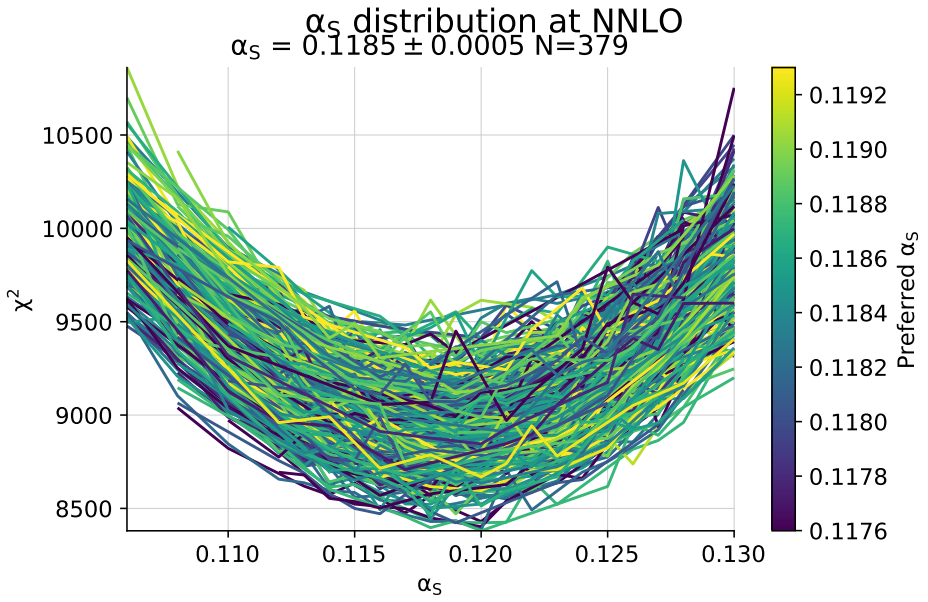

Figure 3.1: The χ^2 profiles for each of the c-replicas used for the NNLO determination of $\alpha_s(M_Z)$. Each curve is fitted to the error function Eq. (3.12).

specific c-replica. We can see that the probability distribution is broader at NLO than at NNLO, and the best-fit is higher. The decrease of the best-fit value of $\alpha_s(M_Z)$ when going from NLO to NNLO has been repeatedly observed before (see Table 1 of Ref. [115] for an extensive set of examples), and the broadening of the distribution is due to the poorer quality of the fit at NLO.

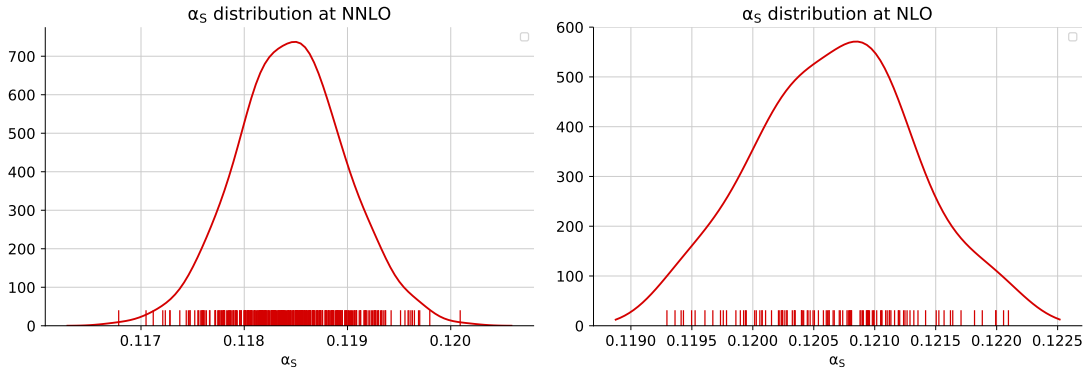

Figure 3.2: The probability distributions for the best-fit $\alpha_s^{\min(k)}(M_Z)$ values Eq. (3.7) at NNLO (left) and at NLO (right).

Impact of individual datasets

We can try to approximate the impact of different types of input data on the determination of $\alpha_s(M_Z)$. This allows us to gain a rough estimate of how each type of process impacts the global best-fit determination. To do this, we assess the impact of the different datasets on the error function by determining the partial χ^2_p for a process, p, defined as the error function Eq. (3.2), where the summation is now just over data belonging to process p. Neglecting correlations between processes, the error function is additive, and we are therefore able to gain a qualitative understanding of how different datasets pull on the global best-fit. The fit procedure then proceeds as normal, just using the partial χ^2_p instead of the global one.

Note that the error function Eq. (3.2) does in fact depend on the total dataset due to the luminosity correlations in the covariance matrix. Furthermore, when doing this analysis, we are using the PDFs defined as the best fit using the global data set, which is not equivalent to the best fit PDF that has been optimised for each process. We therefore can in no way state that the partial χ^2_p gives us the best fit result for that process, as we are not using optimised PDFs. We emphasise this is a qualitative test to see roughly what is the impact of LHC data on the global best fit $\alpha_s(M_Z)$ by looking at the value of $\alpha_s(M_Z)$ obtained for individual processes, however still using the global PDF fit. A more quantitive discussion of this can be found in [116].

We group processes into 8 general categories: top production, the Z p_T distributions, collider and fixed target Drell-Yan, inclusive jets, and DIS either at HERA or at fixed-target experiments, in the latter case separating charged lepton and neutrino beams. The number of data points corresponding to each is shown in Table 3.1. The minima of the partial χ^2 for each process is shown in Fig. 3.3. The central value and uncertainty shown are respectively determined as the median and 68% symmetric confidence level interval from the corresponding partial

	NLO	NNLO
Fixed-target charged lepton DIS	973	973
Fixed-target neutrino DIS	908	908
Collider DIS (HERA)	1221	1211
Fixed Target Drell-Yan	189	189
Collider Drell-Yan	378	388
Inclusive jets	164	164
Z p_T	120	120
Top quark pair production	26	26
Total	3979	3979

Table 3.1: Number of data points at NLO and NNLO corresponding to the different subsets of the input experimental data considered.

$\alpha_{s,p}^{\min(k)}(M_Z)$. This is because the analogue of Fig. 3.2 for individual processes turns out to be highly non-Gaussian, so we instead use the 68% confidence level interval.

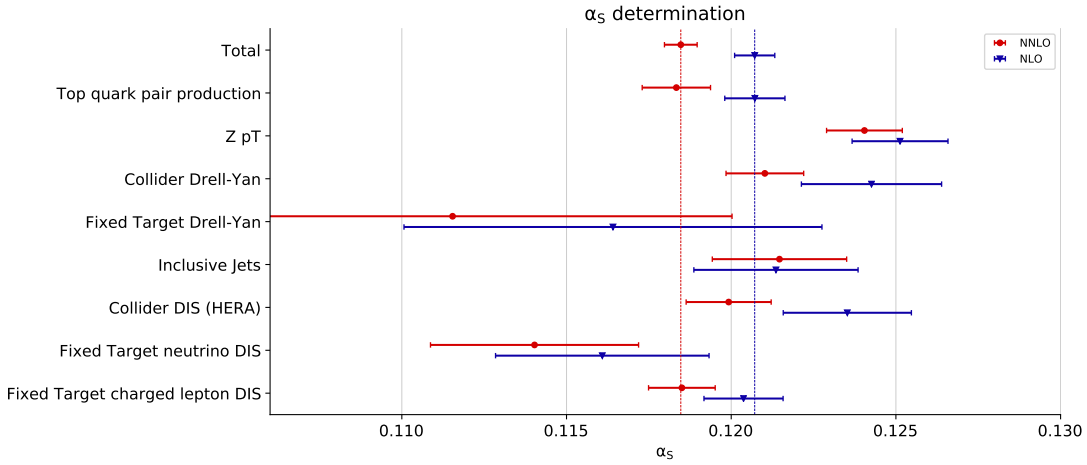

Figure 3.3: The values of the partial $\alpha_s(M_Z)$ and the 68% confidence level intervals determined from χ^2_p for the 8 groups of processes p of Table 3.1 at NLO and NNLO.

Another way in which we can see how each process contributes to the best-fit result for $\alpha_s(M_Z)$, is to look at the contribution of the partial χ^2_p to the total error function, χ^2. In Fig. 3.4 we show the cumulative difference between the χ^2_p for

each process and its value computed at the global best-fit using the central PDF from ones of the batches, and again neglecting correlations between processes. We see that both at NNLO and NLO the LHC data contributes significantly to constraining $\alpha_s(M_Z)$. In particular, we note that the 13 datapoints from top-pair production lead to a significant contribution to the χ^2 away from the best-fit region, even though the full dataset is nearly 4000 points. This implies that there is a small range of possible values of $\alpha_s(M_Z)$ where the top data is consistent with the rest of the data entering the fit. We note that the impact of the top data is expected to decrease if we were to keep track of the correlation between α_s and the top mass, m_t, which itself has an associated uncertainty.

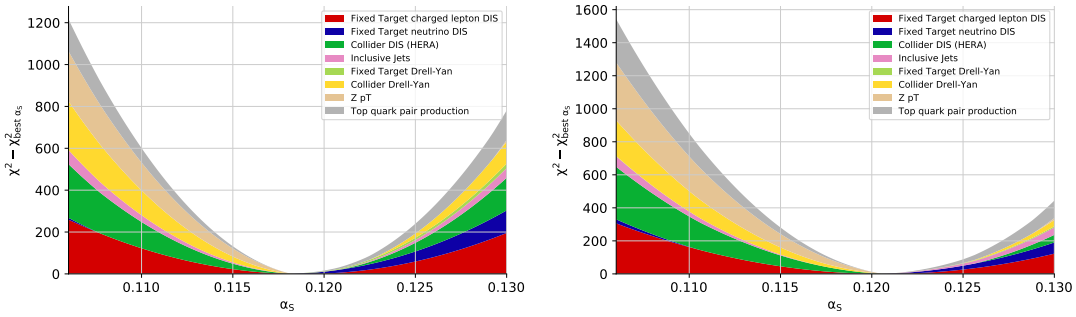

Figure 3.4: Difference between the χ^2_p at $\alpha_s(M_Z)$ and its value at the central best-fit α_s at NNLO (left) and NLO (right).

$\Delta\chi^2 = 1$ method

We can finally compare the current determination with the one found using the previous NNPDF methodology of Refs. [99, 100]. We compute the mean PDF replica for each value of $\alpha_s(M_Z)$, without correlating the data samples across values of $\alpha_s(M_Z)$. We can then proceed as usual and fit a parabola to the total $\chi^2(\alpha_s(M_Z))$, determine $\alpha_s^{\min}(M_Z)$ and the $\Delta\chi^2 = 1$ interval.

Using this method we find

$$\begin{aligned} \alpha_s^{\rm NNLO}(m_Z) &= 0.1180 \pm 0.0004^{\alpha_s}\ (0.3\%)\,, \\ \alpha_s^{\rm NLO}(m_Z) &= 0.1203 \pm 0.0004^{\alpha_s}\ (0.3\%)\,. \end{aligned} \tag{3.25}$$

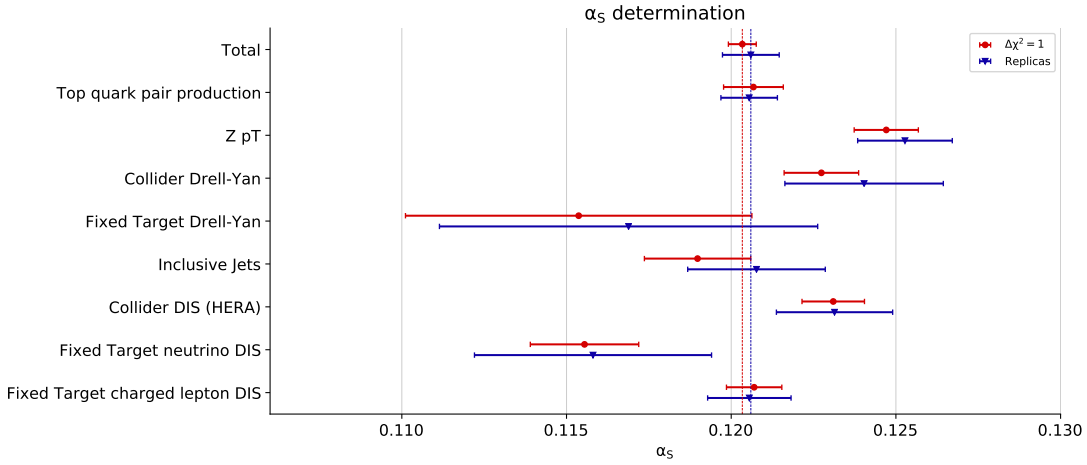

Figure 3.5: The values of the partial $\alpha_s(M_Z)$ at NLO using the $\Delta\chi^2 = 1$ method and the c-replica method.

As before, we can look at the partial χ^2_p for the data subsets, to see how each dataset affects the global determination. In Fig. 3.5 we compare the values of the partial $\alpha_s(M_Z)$ obtained at NLO for the two methods. Unsurprisingly, the $\alpha_s(M_Z)$ values agree well, both in the full determination Eq. (3.25), as well for the individual processes.

3.3.2 Methodological uncertainties

Our determination of $\alpha_s(M_Z)$ leads to an α_s uncertainty of 0.4% at NNLO; given how small the uncertainty is, we need to assess possible additional sources of uncertainty due to our methodology described in Sec. 3.2. The selection algorithm discussed in Sec. 3.2 has some element of arbitrariness associated to it, specifically in the range of $\alpha_s(M_Z)$ used and in the criteria used to determine the minimum number of points needed to fit. We will discuss each of these in turn by varying the settings in a reasonable range to assess their impact on the overall result. We use as default the combined result obtained from three batches of fits at NNLO, which was used to obtain our main result, Eq. (3.23).

Replica selection

The replica selection algorithm determines, in an automated way, the optimal value of $N_{\min}$ for which results must be available for a c-replica to be selected. To probe the impact of this value, we manually vary $N_{\min}$ from 3 (the minimum number of points needed to fit a parabola) to 18 (meaning that at most three values α_s can be missing in order for a c-replica to be retained). Results for the number of c-replicas passing the criterion and the ensuing value of $\alpha_s(M_Z)$ are collected in Table 3.2. The results show that the dependence on the central result with the number of selected curves is always smaller than the α_s uncertainty. These variations are an estimate of the uncertainty on the α_s uncertainty itself. The α_s uncertainty decreases significantly when we require 18 points to fit the parabola, but at the cost of vastly reduced statistics as only 12 c-replicas remain.

$N_{\min}$	$\alpha_s(M_Z)$	$N_{\rm rep}$	Δ_{α_s}
18	0.11842 ± 0.00031 (0.3%)	12	0.00009
15	0.11844 ± 0.00044 (0.4%)	92	0.00005
6	$\mathbf{0.11845 \pm 0.00052}$ (**0.5**%)	**379**	**0.00003**
3	0.11844 ± 0.00056 (0.5%)	400	0.00003

Table 3.2: Dependence of the NNLO determination of $\alpha_s(M_Z)$ on the minimum number of α_s values per c-replica $N_{\min}$ (see Sect. 3.2.3). The chosen value of $N_{\min}$, along with the associated determination of $\alpha_s(M_Z)$ is given in bold.

For the value selected by the algorithm, the finite size uncertainty is almost a factor 20 smaller than the α_s uncertainty Eq. (3.23) and it does not decrease further even when all c-replicas are kept. We therefore conclude that the value of $\alpha_s(M_Z)$ and the α_s uncertainty are very stable, within reasonable ranges of $N_{\min}$. The reason for this is that each c-replica consists of at least $N_{\min}$ correlated PDF replicas, that is, each determination in Table 3.2 is obtained from $N_{\min} \times N_{\rm rep}$ PDF replicas. The methodological uncertainty due to the replica selection algorithm is therefore of order $\Delta_{\alpha_s} = 0.00003$ (0.03%).

We also check the dependence on the values of $\alpha_s(M_Z)$ that are the furthest from the best-fit value. We expect our best-fit to be independent of the PDF fits which have extreme $\alpha_s(M_Z)$ values, so long as the parabolic behaviour can be resolved within statistical fluctuations. To ensure this is the case, we repeat the fitting after removing a number of $\alpha_s(M_Z)$ values furthest from the best-fit $\alpha_s^{\rm NNLO}(M_Z)$, i.e. removing values from the fit where $|\alpha_s(M_Z) - \alpha_s^{\rm NNLO}(M_Z)|$ is greatest. The results are presented in Table 3.3. We see that the central values are consistent within uncertainties even if we only fit half of the points, and the uncertainties only begin to increase when we trim the 15 most distant values of $\alpha_s(M_Z)$, which leaves us with only 10 curves to fit.

$N_{\rm trim}$	fitted $\alpha_s(M_Z)$ range	$\alpha_s(M_Z)$	$N_{\rm rep}$
0	$[\mathbf{0.106}, \mathbf{0.130}]$	$\mathbf{0.11845 \pm 0.00052}$ $(\mathbf{0.4}\%)$	**379**
2	$[0.108, 0.128]$	0.11846 ± 0.00045 (0.4%)	218
5	$[0.110, 0.126]$	0.11852 ± 0.00051 (0.4%)	290
10	$[0.114, 0.124]$	0.11869 ± 0.00046 (0.4%)	32
15	$[0.115, 0.120]$	0.11822 ± 0.00079 (0.7%)	10

Table 3.3: Results for the NNLO determinations of $\alpha_s(M_Z)$ when the $N_{\rm trim}$ outer values of α_s are not used and the fit is restricted to a smaller range. The row in bold corresponds to our final result Eq. (3.23).

Parabolic fitting

The final aspect of the methodology which we would like to check is the independence of the procedure on the parabolic fit. As we saw in Fig. 3.1, the parabolic approximation is likely very good, however it is important to check that methodological uncertainties in this approximation are under control. Any transformation of the χ^2 of the form

$$\chi^2(\alpha_s) \to \chi^2(f(\alpha_s))\,, \tag{3.26}$$

where f is sufficiently smooth and monotonic, should lead to the same best-fit value of α_s. The results of fitting α_s from the transformed profiles Eq. (3.26) with $f(\alpha_s) = \exp(\alpha_s)$ and $f(\alpha_s) = \ln(1+\alpha_s)$ are shown in Table 3.4, finding the results are consistent within α_s uncertainties. We can estimate the uncertainty related to the parabolic approximation as the largest shift observed in Table 3.3, neglecting the cases with $N_{\rm rep} < 100$ which are dominated by the finite size uncertainty,

$$\Delta_{\rm par} = 0.00010 \ (0.08\%) \, . \tag{3.27}$$

	$\alpha_s(M_Z)$	$N_{\rm rep}$
default	$\mathbf{0.11845 \pm 0.00052}$ **(0.4%)**	**379**
ln	0.11845 ± 0.00052 (0.4%)	379
exp	0.11849 ± 0.00052 (0.4%)	379

Table 3.4: Comparing the default parabolic fitting of the $\chi^2(\alpha_s)$ profiles with $\chi^2\left(\ln(1+\alpha_s)\right)$ and $\chi^2\left(\exp(\alpha_s)\right)$.

In summary, we conservatively estimate methodological uncertainties by adding in quadrature the finite size uncertainty $\Delta_{\alpha_s} = 0.00003$ and the uncertainty related to the parabolic approximation $\Delta_{\rm par} = 0.00010$

$$\sigma^{\rm meth} = 0.0001 \ (0.09\%) \, . \tag{3.28}$$

Therefore, we find that, at NNLO, methodological uncertainties are smaller than the experimental uncertainties Eq. (3.23) by a factor of five.

3.3.3 Theoretical uncertainties from missing higher orders

The theoretical uncertainties related to a determination of $\alpha_s(M_Z)$ include MHOU, electroweak effects, nuclear corrections, higher-twist corrections, and others. This work was limited to understanding more thoroughly the interplay between PDFs

and α_s, and, as such, we do not attempt to provide a realistic determination of any of the theoretical uncertainties. We can, however, obtain a rough bound on the MHOU by comparing the results at NLO and NNLO

$$\Delta\alpha_s^{\text{pert}} \equiv |\alpha_s^{\text{NNLO}}(M_Z) - \alpha_s^{\text{NLO}}(M_Z)| = 0.0022\,, \tag{3.29}$$

and taking half the difference. We assume that the N^{3}LO corrections are smaller than the NLO $\to$ NNLO ones, so we conservatively estimate the MHOU to be

$$\Delta\alpha_s^{\text{th}} = 0.0011\ (0.9\%)\,. \tag{3.30}$$

This is significantly larger than the α_s uncertainty and suggests that the theoretical uncertainties are at least comparable to the α_s ones, as we neglect all other sources of theory uncertainty. Recent work by MMHT [103] and NNPDF [104] shows that encorporating MHOU into PDF fits is possible, and may allow for more realistic estimates for the MHOU on extracting α_s from a PDF fit in the future.

3.4 Final results

We can now collect results. Combining the NNLO value and experimental uncertainty Eq. (3.23), the methodological uncertainty Eq. (3.28) and the theoretical uncertainty Eq. (3.30) we get

$$\alpha_s^{\text{NNLO}}(m_Z) = 0.1185 \pm 0.0005^{\alpha_s} \pm 0.0001^{\text{meth}} \pm 0.0011^{\text{th}} = 0.1185 \pm 0.0012\ (1\%)\,, \tag{3.31}$$

where in the last step we have added all uncertainties in quadrature.

In Fig. 3.6 we compare the NNLO result to our previous result [100], to the current PDG average [21], and to two recent determinations obtained from simultaneous fit of PDFs and $\alpha_s(M_Z)$, ABMP16 [117] and MMHT2014 [118]. We find good agreement with the PDG average as well as with the MMHT14 and NNPDF2.1 determinations, although the former do not include theory uncertainties

in their determination. The larger experimental uncertainty found by MMHT is likely due to the lack of recent LHC data in the fit, as the MMHT result is approximately four years older than the NNPDF3.1 result. Interestingly, the $\alpha_s(M_Z)$ determination from the NNPDF3.1 fit is higher than any other recent determination from PDF fits. Inspection of Figs. 3.3 and 3.4 strongly suggests that this increase is driven by the high-precision LHC data, especially for gauge boson production (including the Z p_T distribution) but also for top and jet production.

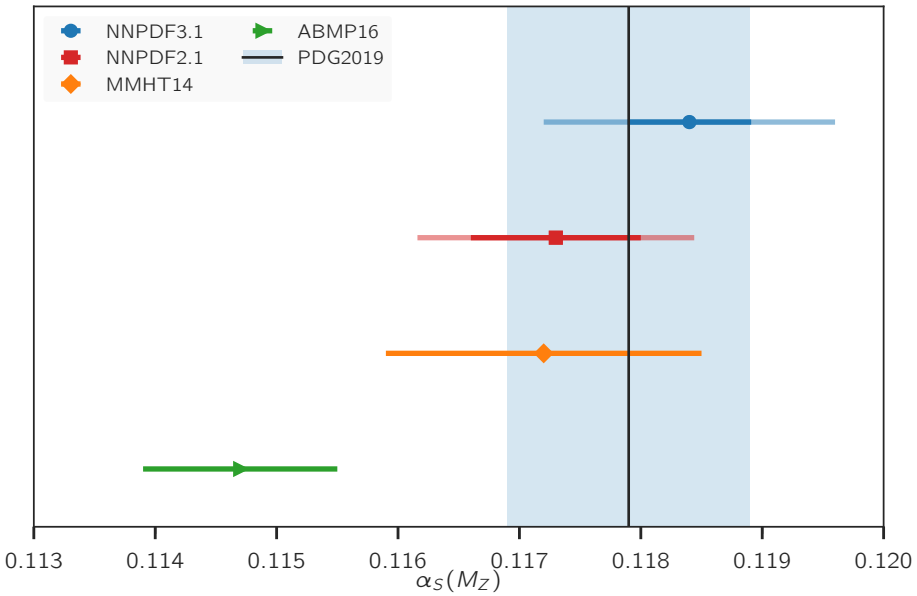

Figure 3.6: Comparison of the new NNLO determination of $\alpha_s(M_Z)$ with the PDG average and with the previous ABMP16, MMHT14, and NNPDF2.1 results. For the NNPDF values, the darker error bars correspond to PDF uncertainties, while the lighter one indicates the sum in quadrature of PDF and theoretical uncertainties.

CHAPTER 4

The SMEFiT framework

From a methodological point of view, a global fit of the Wilson coefficients in the SMEFT requires a robust fitting framework, in conjunction with precise theoretical predictions and experimental measurements. In particular, a fitting framework should not make any further assumptions about the structure of either the theory or experimental measurements, and should be minimal in methodological uncertainties. In this chapter, we will introduce the SMEFiT methodology, first discussed in [2], but we will discuss improvements and changes which have been made since and will appear in a future paper [3].

The SMEFiT framework is based on the idea that, using Monte Carlo methods, we can construct a sampling of the probability distribution in the space of the experimental data. This then translates into a sampling of the probability distribution in the space of the Wilson coefficients by means of the fitting procedure. We will discuss in turn two separate methods; the Monte Carlo replica method, and Nested Sampling (NS). As a baseline methodology we will use the Monte Carlo replica method and Nested Sampling will only be mentioned in this chapter.

The two methods are both based on a Monte Carlo implementation, but are distinct, and enable us to test our baseline fitting methodology.

4.1 Monte Carlo representations

In this section we will describe the SMEFiT fitting approach using the Monte Carlo replica method and Nested Sampling. We will introduce the two methodologies in turn, and discuss the construction of the χ^2 used in both methodologies.

4.1.1 The Monte Carlo replica method

The central idea behind the replica method is that by doing Monte Carlo sampling of the experimental data, we can propagate experimental uncertainties to the fitted Wilson coefficients. To do this, we construct a sampling of the probability distribution in the space of the experimental data, which then translates into a sampling of the probability distribution in the space of the Wilson coefficients. This can be implemented by generating a large number $N_{\rm rep}$ of artificial replicas of the original data, as discussed in Sec. 3.2.1.

This methodology is in fact inspired by the NNPDF methodology, where now our unknown parameters are the Wilson coefficients, not the PDF parameters. As before, we generate artificial data replicas of the experimental data according to Eq. (3.1), such that with sufficient replicas we can reproduce the original statistical properties of the data. We find that with 500 artificial replicas, the results for the Wilson coefficients become independent of $N_{\rm rep}$; therefore to be conservative, in all cases we will show results where $N_{\rm rep} = 1000$. The main advantage of this method is that it does not require any assumption about the underlying probability distribution of the parameters, and in particular it is not restricted to Gaussian distributions. Moreover, it is suited to problems where the parameter space is large and complicated, with a large number of flat directions.

4.1.2 Minimisation

Similarly to the case of the α_s fit, the χ^2 is given for the replica method by

$$\chi^{2(k)}(\{c\}, D) = \frac{1}{N_{\rm dat}} \sum_{i,j} \left(T_i[\{c\}] - D_i^{(k)}\right) C_{ij}^{-1} \left(T_j[\{c\}] - D_j^{(k)}\right) \,, \tag{4.1}$$

where $T_i[\{c\}]$ is the theoretical prediction for the $i-$th cross section. We can then perform statistics over the samples of the Wilson coefficients, in order to compute central values and errors.

We need to consider how to best perform the minimisation in the large parameter space of the Wilson coefficients. We use an algorithm implemented in `SciPy`, optimised for constrained minimisation for large parameter spaces. Similarly with PDFs, we also need to take into account the fact that we are fitting a functional form, Eq. (2.45), with statistical fluctuations from the replicas, and we therefore need to be wary of over-fitting. We therefore employ cross-validation, such that the best-fit parameters are found as

$$c^{\min(k)} = \text{cv} \arg\min[\chi^2(\{c\}, D^{(k)})] \,. \tag{4.2}$$

As discussed in Sec. 3.2.1, the stopping point of the fit is taken to be at the absolute minimum of the validation set, not the training set. We will discuss the importance of cross-validation in Sec. 4.3, where we will see that fits without cross-validation lead to spuriously tight errors on poorly bounded coefficients.

Assuming that theoretical uncertainties follow an underlying Gaussian distribution, and that they are uncorrelated to the experimental uncertainties, it can be shown [119] that the total covariance matrix can be expressed as

$$C_{ij} = C_{ij}^{(\rm exp)} + C_{ij}^{(\rm th)} \,, \tag{4.3}$$

that is, as the sum of the experimental and theoretical covariance matrices. There are at least two main classes of theoretical uncertainties that are in principle relevant for the present fits; MHOU and PDF uncertainties. We do not yet take

into account the MHOU; to alleviate the effect of their size, we take into account NNLO QCD corrections for most of the data points, in particular for $t\bar{t}$ and single-top production. Furthermore, when available, the NLO QCD calculation is used for the SMEFT contributions.

In this work, we use as input to all our theory calculations the NNPDF3.1 NNLO no-top PDF set [15], which differs from the NNPDF3.1 baseline set only for the exclusion of the top-quark pair production data from the dataset; this is necessary to avoid double-counting in the fit as the top data used in NNPDF3.1 overlaps with the data used in our analysis.

With this motivation, we construct the theoretical covariance matrix from the contributions of the PDF uncertainty as

$$C_{ij}^{(\mathrm{th})} = \left\langle T_i^{(r)} T_j^{(r)} \right\rangle_{\mathrm{rep}} - \left\langle T_i^{(r)} \right\rangle_{\mathrm{rep}} \left\langle T_j^{(r)} \right\rangle_{\mathrm{rep}} , \tag{4.4}$$

where the theoretical predictions are computed using the SM theory and the r-th replica from the NNPDF3.1NNLO no-top PDF set, and averages $\langle\cdot\rangle_{\mathrm{rep}}$ are performed over the $\widetilde{N}_{\mathrm{rep}} = 100$ replicas of this PDF set. Note that replicas in the PDF set are not directly related to replicas in the SMEFT set, since the two sets represent different probability distributions.

In general, the theoretical covariance matrix, Eq. (4.4), induces correlations between all the datasets included in the fit. However we account for them only within a given dataset, in the same way as for experimental measurements. The inclusion of the PDF correlations between datasets is instead left to future work, as they can be a significant source of correlation in fits to the top sector, due to the high-x gluon. If the PDF-induced correlations between data points i and j are neglected, Eq. (4.4) reduces to

$$C_{ii}^{(\mathrm{th})} = \left\langle \left(T_i^{(r)} \right)^2 \right\rangle_{\mathrm{rep}} - \left\langle T_i^{(r)} \right\rangle_{\mathrm{rep}}^2 , \tag{4.5}$$

and vanishes for $i \neq j$. This corresponds to adding the PDF error in quadrature to the experimental uncertainties.

For consistency, PDF uncertainties should be included in the fit not only via the covariance matrix but also in the replica generation. That is, the generation of the data replicas includes an additional source of fluctuation determined from the theoretical covariance matrix, Eq. (4.5). Since in general the number of SMEFT replicas, $N_{\rm rep} = 1000$, is much larger than the number of PDF replicas, $\widetilde{N}_{\rm rep} = 100$, we bootstrap with replacement over the PDF replicas.

4.1.3 Nested sampling

The second methodology which we implement is Nested Sampling [120, 121] implemented using `MultiNest` [122]. To introduce NS let us first briefly review Bayesian inference. Bayes's theorem states that we can estimate a set of parameters Θ in a model H, given data D by

$$\mathrm{P}(\Theta|D,H) = \frac{\mathrm{P}(D|\Theta,H)\mathrm{P}(\Theta|H)}{\mathrm{P}(D|H)}\,, \tag{4.6}$$

where $\mathrm{P}(\Theta|D,H)$ is the posterior probability of the model parameters, $\mathrm{P}(D|\Theta,H) \equiv \mathscr{L}(\Theta)$ is the likelihood of the data and $\mathrm{P}(\Theta|H) \equiv \pi(\Theta)$ is our prior. $\mathrm{P}(D|H) \equiv \mathscr{Z}$, called the Bayesian evidence, represents the factor needed to normalise the posterior over the domain of Θ, i.e.

$$\mathscr{Z} = \int \mathscr{L}(\Theta)\pi(\Theta)\mathrm{d}\Theta\,. \tag{4.7}$$

NS estimates the Bayesian evidence by transforming the multi-dimensional integral over the prior density $\mathrm{d}\Theta$ into a one-dimensional integral, by first defining

$$X(\lambda) = \int_{\{\Theta:\mathscr{L}(\Theta)>\lambda\}} \pi(\Theta)\mathrm{d}\Theta\,, \tag{4.8}$$

where $X(\lambda)$, often called the prior mass, is the amount of the prior density associated with likelihoods greater than λ, and by construction, as λ increases, X decreases from 1 to 0. The integral extends over the regions of parameter

space contained within the likelihood contour $\mathscr{L}(\Theta) = \lambda$. We then have our one-dimensional integral

$$\mathscr{Z} = \int_0^1 \mathscr{L}(X)\mathrm{d}X \tag{4.9}$$

for $\mathscr{L}(X)$ defined as the inverse of $X(\lambda)$, so long as the likelihood is continuous. Accomplishing this transformation from Θ to X involves dividing the unit prior mass into tiny elements, and sorting them by likelihood.

By then defining a decreasing sequence of values of the prior volume

$$1 = X_0 > X_1 > ...X_\infty = 0\,, \tag{4.10}$$

we can calculate the likelihood at each value $\mathscr{L}_i = \mathscr{L}(X_i)$ and, as we have a positive function, we can numerically sum up all the points to find the total evidence. As the likelihood is in generally not known or very complex, we have to revert to Monte Carlo techniques for computing the summation. We draw N_{live} points from the prior, $\pi(\Theta)$, and begin at X_0. As we decrease X_i, the point with the lowest likelihood value, $\mathscr{L}_i$, is removed from the set, and replaced with another point drawn from the prior under the constraint that its likelihood is larger than $\mathscr{L}_i$. The sampling process is repeated until the entire hypervolume of the prior parameter space is covered, with the live particles being in nested shells of constrained likelihood as the prior volume is reduced. Although the algorithm is designed specifically to estimate the Bayesian evidence, we end up with a set of parameters, Θ, which maximise the likelihood, $\mathscr{L}$, just as in the case of the Monte Carlo replica method.

We can use the fact that, for Gaussian distributions, the log-likelihood is related to the χ^2, Eq. (4.1) and use this as our estimate of the likelihoods at each iteration. For NS, we do not need the replica generation and in Eq. (4.1), we use the experimental data itself and not the data replicas. Consequently, there is no need for cross-validation, as we are looking for the absolute maximum of the likelihood; this is because, in NS, there is no issue with over-fitting to noise in the data as none has been introduced.

Despite the obvious advantages of NS, we will not use it as our baseline fitting methodology. This is because it is not suited to arbitrarily large parameter spaces, and preliminary work has shown it struggles once the 20 or so additional degrees of freedom from Higgs calculations are included into SMEFiT. The replica method has no such limitations, and we therefore proceed with only using NS as a methodological check.

4.2 Closure testing

A reliable fitting framework should be able to fit a wide range of different datasets without tuning the methodology and without biasing the results. Validating a new methodology can be complicated by issues such as potential inconsistencies (internal or external) in the experimental data, or by limitations in the theoretical calculations. To validate the fitting methodology used in this SMEFT analysis, we carry out a series of closure tests, based on pseudodata generated with a known underlying physical law. Closure tests were first developed in the context of PDF fits; see [105] for more details.

The basic idea underlying a closure test is to test the SMEFT fitting procedure by performing fits where the "correct" result is known, i.e. by fitting pseudodata generated from a fixed reference set of values for the SMEFT degrees of freedom, $\{c^{(\mathrm{ref})}\}$. Closure testing in the SMEFiT framework is therefore much simpler than the PDF case, as the pseudodata are generated by simply choosing $\{c^{(\mathrm{ref})}\}$ and creating replicas in the same way as in Sec. 4.1.1. In all of the closure tests, we use the same statistics as used in the real fits to data, i.e. $N_{\mathrm{rep}} = 1000$. Closure tests allow one to check that the fitting methodology can reproduce the underlying law, which is known by construction.

The SM and SMEFT theory calculations can be assumed to be exact, since we use the same theory settings to generate and fit the pseudodata. As a consequence, the theoretical uncertainties associated to MHOs and PDFs do not enter closure

tests, where only methodological and experimental uncertainties are checked. In the case of SMEFT fits, we can perform a closure test assuming that the underlying truth is the SM, i.e. $\{c^{(\mathrm{ref})} = 0\}$, or any BSM scenario, i.e. $\{c^{(\mathrm{ref})} \neq 0\}$. This allows for the validation of potential BSM anomalies identified in the SMEFT fit to the actual experimental data.

In the following, we will only closure test the Monte Carlo replica method, as it is our baseline methodology. The NS methodology is itself a separate methodological check of the replica method, and we do therefore not consider closure tests of NS. The comparison of NS with the replica method is discussed in Sec. 4.3.1. We consider three levels of closure tests according to the type of pseudodata that is used as input to the fit.

Level 0 In a level zero (L0) closure test the pseudodata coincides with the true underlying law, without any additional fluctuations. Then N_{rep} fits are performed to exactly the same pseudodata, with the only difference being the random initial conditions in each case. The initial conditions are defined by first performing individual fits to each degree of freedom, to obtain the non-marginalised bounds. We then require the global fit to initialise at some value within each individual bound, broadened by 4σ from the mean.

If the pseudodata is generated with the SM hypothesis $\{c^{(\mathrm{ref})} = 0\}$, then the same values should be reproduced at the fit level within uncertainties. At L0, the training/validation partition is not necessary, since the information contained in both sets would be identical.

We also expect the χ^2 to tend to zero for a large enough number of iterations. Therefore, direct evidence that a L0 test is successful is to show how the error function decreases with the number of iterations. A L0 closure test therefore allows one to check that the minimiser is efficient enough to properly explore the entire parameter space.

Level 1 In a level one (L1) closure test, one adds noise on top of the pseudodata. Two types of noise may be added; in a L1a closure test we generate Monte Carlo replicas of the data generated in a L0 closure test in the same way as in a real fit to data. Alternatively, in a L1b closure test one adds stochastic noise directly to the data, in order to replicate experimental uncertainties included in the fits to data. In this work we adopt a L1a-type closure test. We note that adopting a L1a-type test over L1b simply means that a different type of uncertainty is being probed at L1 - we discuss the various types of uncertainty in Sec. 4.2.3 where we characterise the types of fit uncertainties.

In comparison to a L0 closure test, a L1 closure test propagates the experimental uncertainties into the fitted coefficients, and can therefore be used to demonstrate that the quoted uncertainties in the fit parameters admit a robust statistical interpretation. One expects $\chi^2/N_{\rm dof} \sim 1$ for a successful closure test.

Level 2 In a level two (L2) closure test, one adds the L1b noise on top of the Monte Carlo replicas included in the L1a closure test. This statistical noise is generated according to the experimental covariance matrix of the real data. A L2 closure test is therefore equivalent to a fit to the real data, the only difference being that data and theory are perfectly consistent by construction.

4.2.1 L0 closure tests

First of all, we want to demonstrate that the optimiser is efficient enough to explore the full parameter space. In Fig. 4.1 we show the χ^2 for L0 closure tests based on the SM scenario as a function of the number of iterations in the minimiser for three replicas. We see how the χ^2 decreases with the number of iterations, approaching the limit $\chi^2 \to 0$ which corresponds to the case where the fit results reproduce the reference values $\{c = 0\}$.

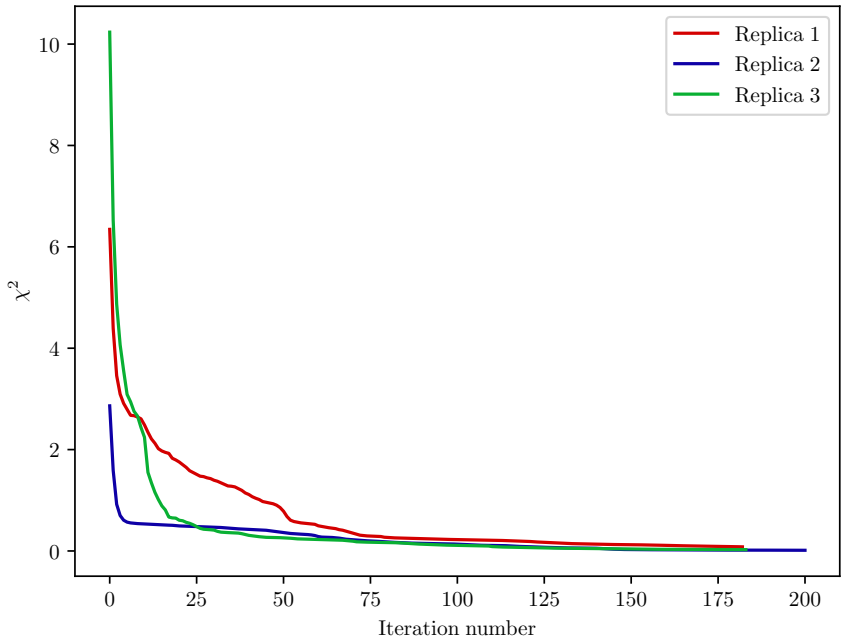

Figure 4.1: The χ^2 for L0 closure tests as a function of the number of iterations.

In Fig. 4.2 we show the central values and 95% confidence level (CL) intervals for the $N_{\rm op} = 34$ degrees of freedom included in the fit. We find that the central values are all very close to zero, and that the uncertainties are in general very small. For several of the degrees of freedom, namely the four-heavy quark ones, we observe that the uncertainties are substantially larger than the others. This is simply due to the lack of data constraining these degrees of freedom; so long as the level 1 and 2 closure tests find larger uncertainties for them, then we are satisfied that the level 0 closure test has been successful.

4.2.2 L2 closure tests

We can now compare our L0 results with L2, as here we add both kinds of fluctuations. In this case we compare the results based on two different hypotheses for the underlying theory; one in which all degrees of freedom are set to their SM values; and another in which all degrees of freedom are set to their SM

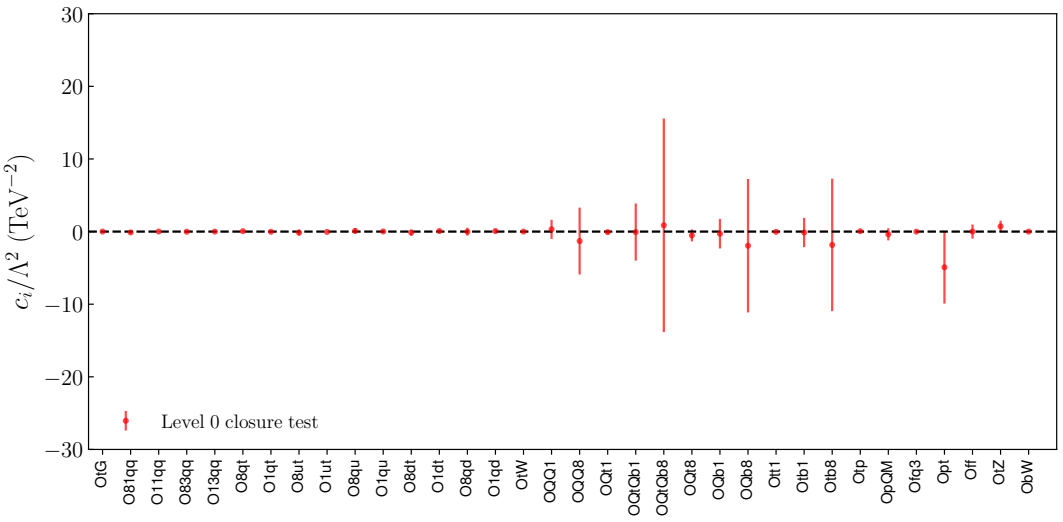

Figure 4.2: Central value and 95% confidence level intervals for the 34 SMEFT degrees of freedom included in the fit for the L0 closure test.

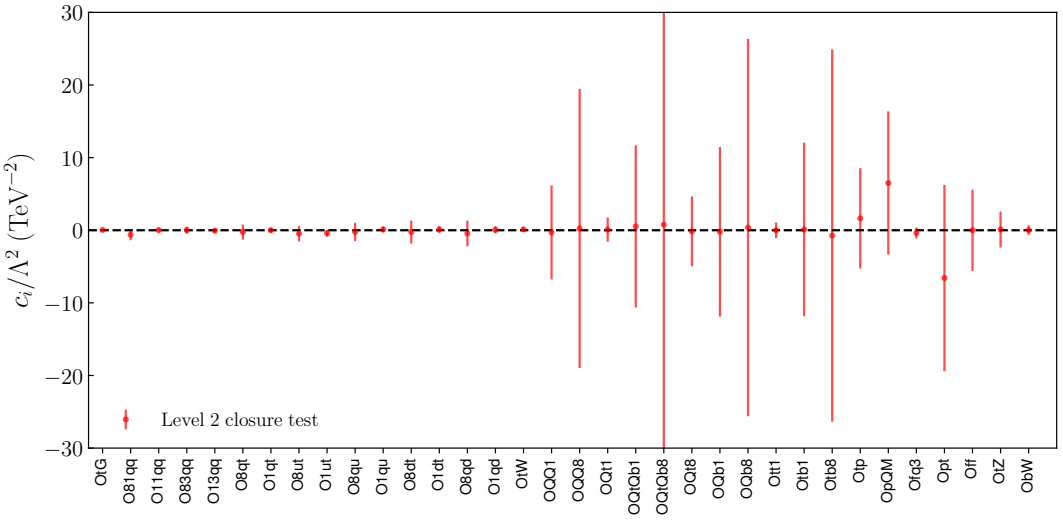

Figure 4.3: Same as in Fig. 4.2, but now for the L2 closure tests.

values, except $c_{tu}^8/\Lambda^2 = 20$ TeV^{-2}. The goal of this exercise is to verify if the fit can successfully identify a BSM deviation once it is built into the pseudodata. The results of the L2 closure test to the SM is shown in Fig. 4.3; we find that the fit manages to reproduce the underlying law, with the expected increase in uncertainty with respect to L0.

In Fig. 4.4 we show fit residuals for the L2 closure test in the BSM scenario

where one has set $c_{tu}^8/\Lambda^2 = 20$ TeV^{-2}. They are defined as

$$r_i \equiv \frac{\left(\langle c_i \rangle - c_i^{(\text{ref})}\right)}{\delta c_i}\,, \tag{4.11}$$

where $\langle c_i \rangle$ and δc_i indicate the expectation value and the 95% confidence level interval. By setting $c_{tu}^8/\Lambda^2 = 20$ TeV^{-2} this allows us to ensure the starting point of the fit is BSM for this operator, but is not so far away from the SM as to make the closure test redundant. We find that the central value lies about 2σ away from the SM in this case. Importantly, the residual for this degree of freedom is larger in magnitude than any other one. However, the result is not statistically significant; with 34 degrees of freedom, it is reasonable for one or two of them to have residuals corresponding to a 2σ deviation.

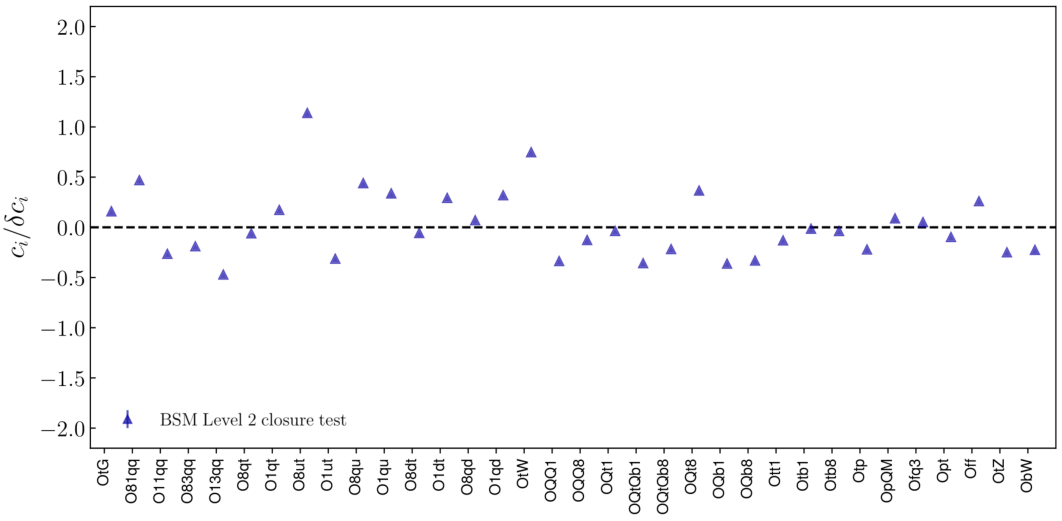

Figure 4.4: The fit residuals, where δc_i corresponds to the 95% confidence level interval, for the L2 closure test in the BSM scenario where one has set $c_{tu}^8/\Lambda^2 = 20$ TeV^{-2}.

It is important to note that the degrees of freedom are not entirely independent of each other, since some degrees of freedom are (anti-)correlated. To quantify this, in Fig. 4.5 we show the values of the correlation coefficient between the different degrees of freedom c_i for the L2 closure test with SM reference values. The correlation coefficient between two of the degrees of freedom in the fit c_i and

c_j is computed using the standard Monte Carlo expression, namely

$$\rho\left(c_i, c_j\right) = \frac{\frac{1}{N_{\rm rep}} \sum_{k=1}^{N_{\rm rep}} c_i^{(k)} c_j^{(k)} - \left\langle c_i \right\rangle \left\langle c_j \right\rangle}{\delta c_i \delta c_j} \,. \tag{4.12}$$

From this comparison we see that some degrees of freedom are very correlated, for example the chromomagnetic operator `OtG` is highly anti-correlated with the two-heavy-two-light operators `O81qq` and `O13qq`. The same pattern is also apparent at leading order, which means that it is the four-heavy quark datasets that induce this correlation. We will discuss in detail in Sec. 5.1 the datasets which enter the fit, but we will just mention here that only two of these four-heavy quark datasets are currently included, and one expects that the correlation between `OtG` and `O81qq` and `O13qq` should be lifted upon the addition of more data.

We show in Fig. 4.6 the same as Fig. 4.4, but now turning off the correlations between the degrees of freedom. This means that we enforce that the 34 degrees of freedom are independent variables, by assuming all but one coefficient is SM-like at a time. We see that, not only are the residuals now more spread out around the SM point, but also the deviation for the BSM point is more significant; closer to a 4σ deviation. In other words, the reduced spread of the residuals in the global fit is a genuine effect, arising from the correlations and degeneracies in the explored SMEFT parameter space, rather than an artefact of the fit.

4.2.3 Characterising fit uncertainties

Comparing closure tests at different levels allows one to identify the different components that build up the total uncertainty on the fit parameters. To begin with, L0 closure test results might have interpolation and extrapolation uncertainties; even if the fit to the data points is perfect, there will be non-zero uncertainties in-between and outside the data region. These uncertainties, however, vanish at L0, since the associated parameter space is discretised over the $N_{\rm op} = 34$ independent degrees of freedom, and additional directions are never explored. The uncertainties at L0 are then just from the different initial start points of the fits.

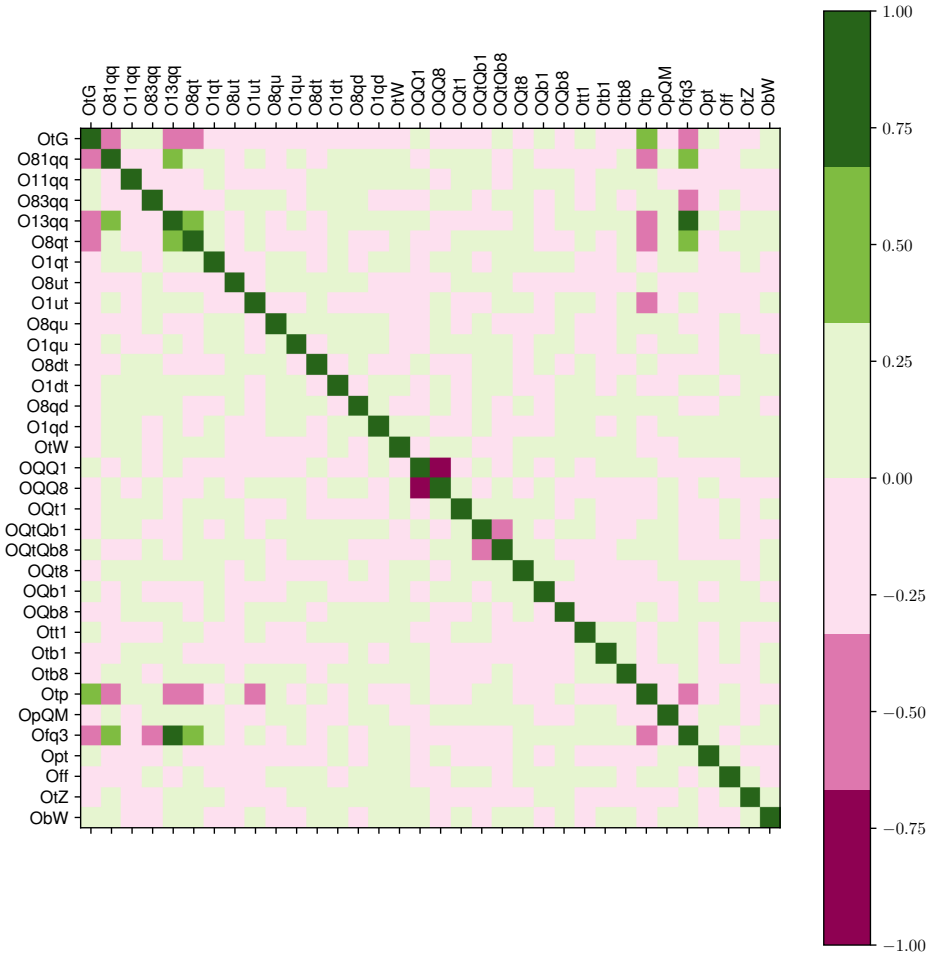

Figure 4.5: The values of the correlation coefficient between the different degrees of freedom c_i, Eq. (4.12), for the L2 closure test with SM reference values.

For well constrained degrees of freedom, such as `OtG`, the uncertainty is very low as it is very well constrained by many datapoints, and so the initial starting points of the fit do not fluctuate much between replicas.

The comparison between the values of δc_i in L1 and L2 closure tests is more subtle. In the L1 case, the data uncertainty is propagated into the fit. Therefore, the component of δc_i that L1 closure tests identify is associated to the finite precision of the input experimental measurements, and hence we call this the experimental component of the uncertainty. At L2, we additionally account for the fact that there are infinite different sets of $\{c\}$ that optimise the χ^2 equally well. The spread among these solutions represent the irreducible redundant component

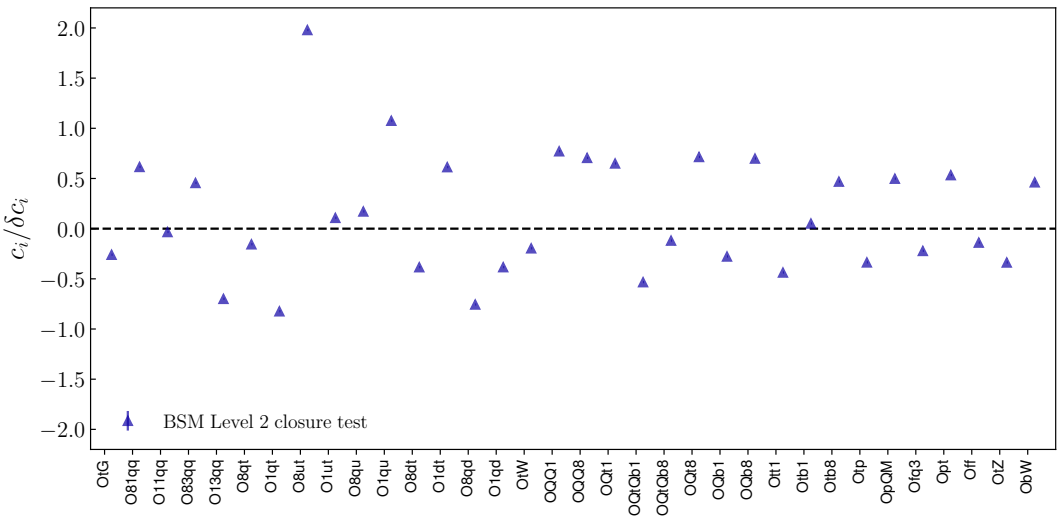

Figure 4.6: Same as Fig. 4.4 for the closure tests in which each of the operators has been constrained separately from all the others.

of the uncertainty.

To illustrate the relative weight of these two components on the overall size of δc_i, in Fig. 4.7 we show the bounds that are obtained in L0, L1 and L2 closure tests. We find that there is a significant increase in the size of δc_i when going from L0 to L1, but then there is only a very slight increase when going from L1 to L2.

4.3 Methodological variations

We now turn to study the robustness of the baseline results with respect to a number of variations in the fitting methodology. In particular we compare: (i) the Monte Carlo method we use to fit; (ii) the impact of cross-validation for the replica method and (iii) the role of $\mathcal{O}\left(\Lambda^{-4}\right)$ corrections. We will always assume the SM; as we have shown above, closure tests will likewise work in the case of BSM scenarios.

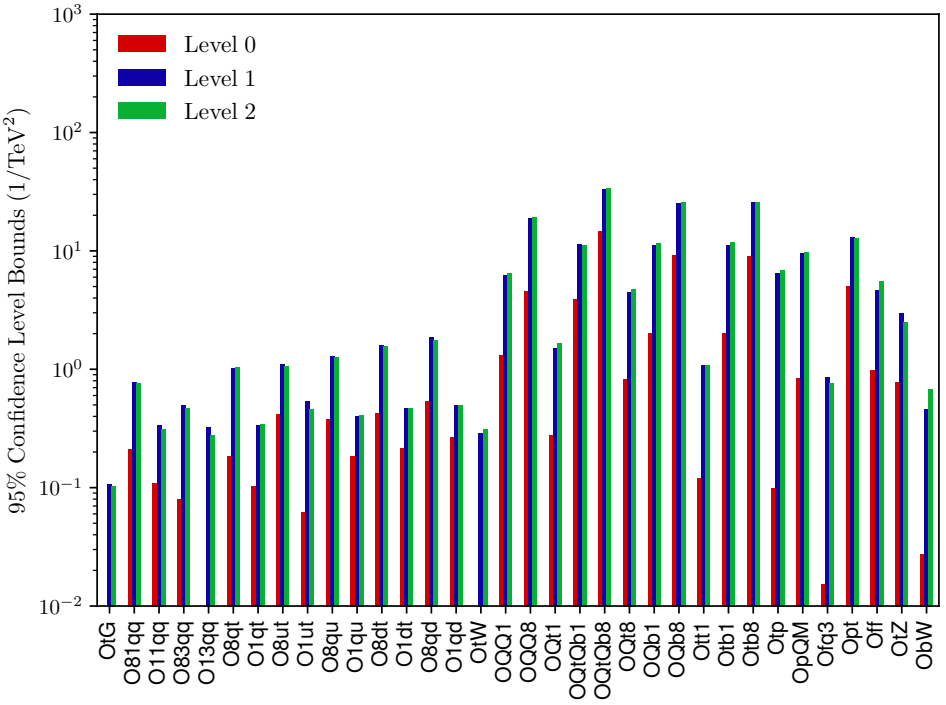

Figure 4.7: The symmetrised 95% CL bounds for the fit parameters, δc_i, obtained in the closure tests at levels 0, 1 and 2.

4.3.1 Fitting methodology

We first want to compare results from NS with the Monte Carlo replica method. We show in Fig. 4.8 the 95% CL intervals for the two methods, and the central values with the error intervals using the baseline settings in both cases. The Monte Carlo replica method includes as its baseline the use of cross-validation; we discuss below the impact of using cross-validation in the fit.

We see that there is excellent agreement between the two methodologies; the degrees of freedom with the largest difference in bounds are from the four-heavy quark operators, as can be seen more clearly in the bottom plot. For these degrees of freedom, there are large statistical fluctuations in both methodologies, due to the small number of data points which constrain them. Therefore, we see that the two independent methodologies agree within uncertainties. This test is highly non-trivial; although both fitting methods employ Monte Carlo techniques, they

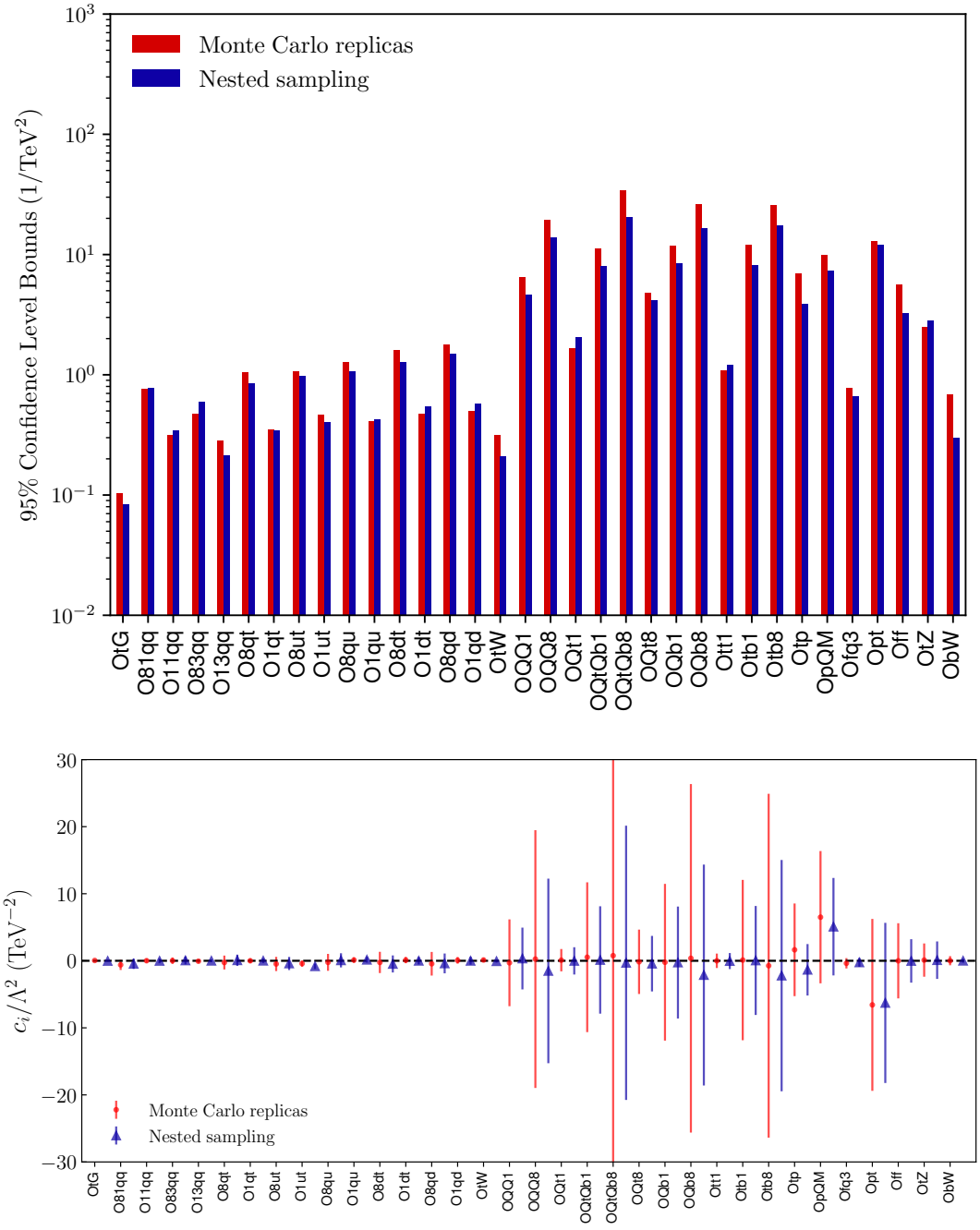

Figure 4.8: Top: 95% confidence level intervals for the a L2 closure test and a Nested Sampling fit. Bottom: The central value and 95% confidence level intervals for the two fits.

are completely different methods, and this is a very strong test of the robustness of our fitting code.

4.3.2 Cross-validation

As discussed in Sec. 4.1.2, when using the Monte Carlo replica method, it is important to ensure that over-fitting is avoided so we adopt cross-validation. To quantify the role that cross-validation plays on fit results, we perform two L2 closure tests, with the only difference that cross-validation is absent in one of them. In Fig. 4.9 we compare the fit residuals and the 95% CL of the fit parameters obtained from the two closure tests.

When cross-validation is absent, we get artificially tight constraints on the four-heavy quark degrees of freedom, which in the global fit, is compensated by vastly loosening the bound on `Otp`. These very tight bounds can be more clearly seen in the bottom plot; there is nearly an order of magnitude reduction in some of the bounds. Whilst a loose bound on `Otp` is not in itself an issue, the tight bounds on the four-heavy quark degrees of freedom are, as they are only constrained by a couple of data points in the fit. It is therefore unrealistic to expect $\mathcal{O}(1)$ uncertainties on such poorly constrained degrees of freedom. We see that, for well constrained degrees of freedom, cross-validation is in good agreement with the baseline fit. This suggests that the over-fitting is only occurring in the regions of parameter space which are able to accommodate large fluctuations. These regions are poorly constrained by the lack of data points in the four-heavy quark case. For `Otp`, however, the lack of sensitivity is caused by large cancellations between the linear and quadratic terms in Eq. (2.45) as the quadratic corrections are of the same size as the linear ones, but with opposite sign.

4.3.3 The role of $\mathcal{O}\left(\Lambda^{-4}\right)$ corrections

Closure tests can also be used to assess the dependence of the fit results upon variations of the details of the theory calculations. Specifically, we are interested in the role played by $\mathcal{O}\left(\Lambda^{-4}\right)$ corrections in the determination of the bounds on the fitted degrees of freedom. We will discuss in detail in Sec. 5.2 the interplay

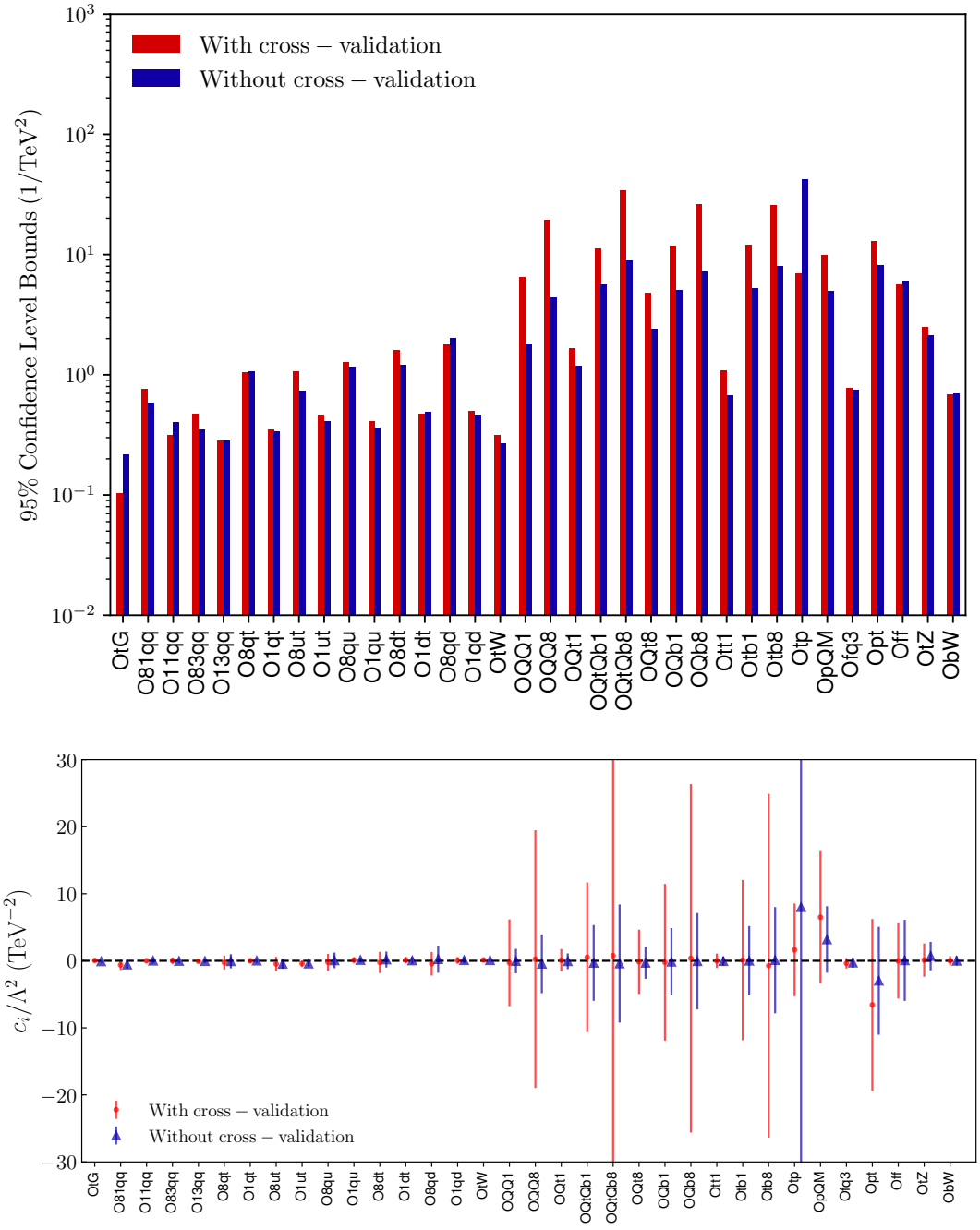

Figure 4.9: Top: The 95% confidence level intervals for two L2 closure tests with and without cross-validation. Bottom: The central value and 95% confidence level intervals for the two fits.

between experimental measurements and the $\mathcal{O}\left(\Lambda^{-4}\right)$ corrections. It is sufficient for now to state that excluding the higher order corrections removes 4 degrees of freedom from our consideration, `OQtQb1`, `OQtQb8`, `Off` and `ObW`.

In Fig. 4.10 we show the comparison of the bounds (top) and central values (bottom) for L2 closure tests between two fits that differ only for the inclusion (or not) of the $\mathcal{O}\left(\Lambda^{-4}\right)$ terms. From this comparison, we see that the bounds on the coefficients δc_i generally improve when $\mathcal{O}\left(\Lambda^{-4}\right)$ corrections are included in the theoretical calculation. The slight worsening observed for the bounds on some operators is consistent with statistical fluctuations due to the lack of data points, both at $\mathcal{O}\left(\Lambda^{-2}\right)$ and $\mathcal{O}\left(\Lambda^{-4}\right)$, and is expected to go away upon the addition of more experimental data. We can see that the bound for `Otp` is slightly improved if we do not include the $\mathcal{O}\left(\Lambda^{-4}\right)$ corrections but this is at the level of statistical fluctuations.

In Fig. 4.11 we show the histograms for the 30 degrees of freedom which enter excluding the higher order corrections in red. In blue, we show the level 2 closure test for the baseline settings. We see that the histograms are in general significantly less Gaussian than the baseline, leading to, in general, wider bounds. This is a strong argument in favour of using pure Monte Carlo approaches, which do not require any assumption about the probability distribution of the Wilson coefficients. We still have distributions which are highly non Gaussian for the baseline, for example for `ObW`; this is because `ObW` only enters at $\mathcal{O}\left(\Lambda^{-4}\right)$, and is therefore poorly constrained by the fit.

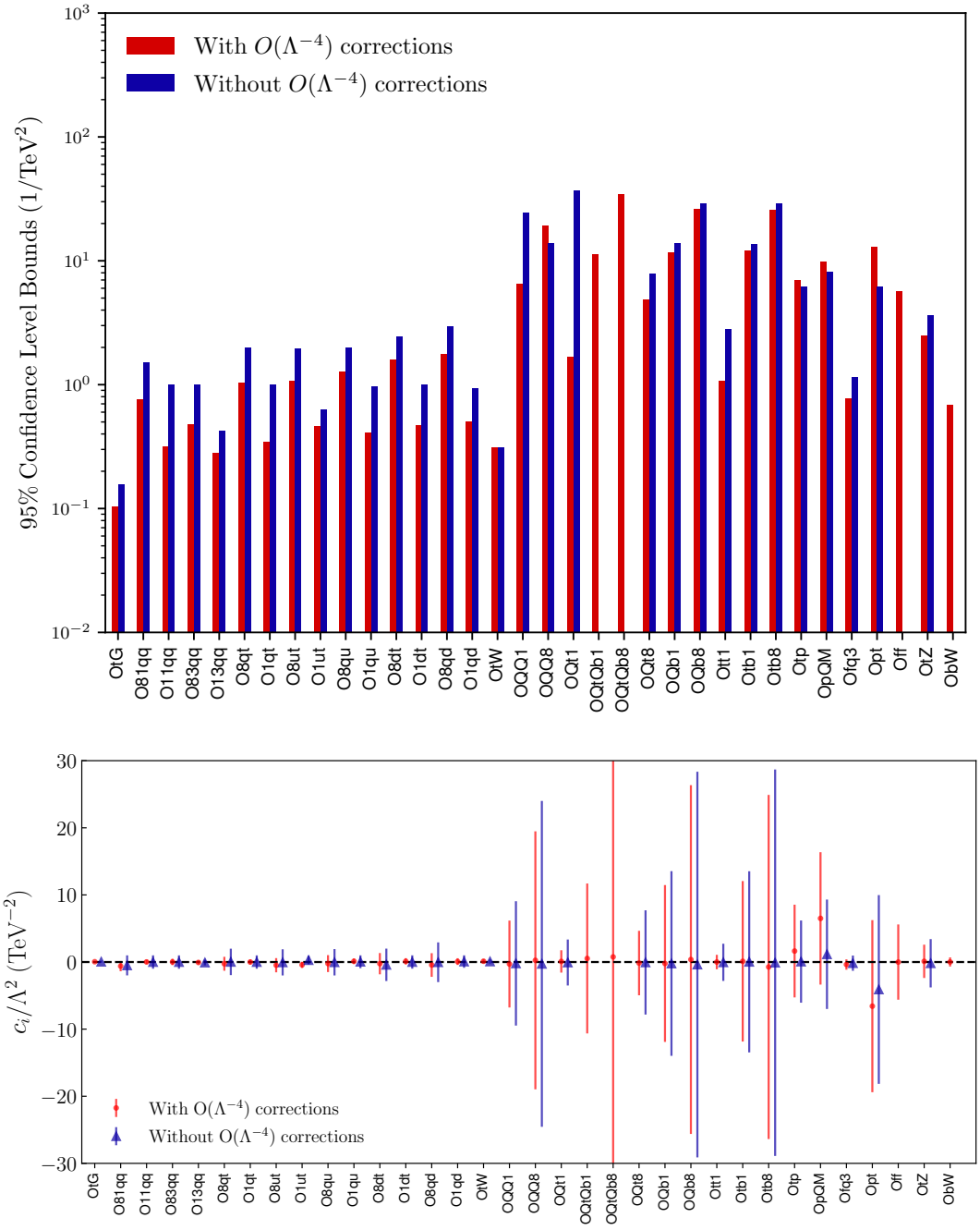

Figure 4.10: Top: The 95% confidence level intervals for two L2 closure test fits with and without $\mathcal{O}\left(\Lambda^{-4}\right)$ SMEFT corrections. Bottom: The central value and 95% confidence level intervals for the two fits.

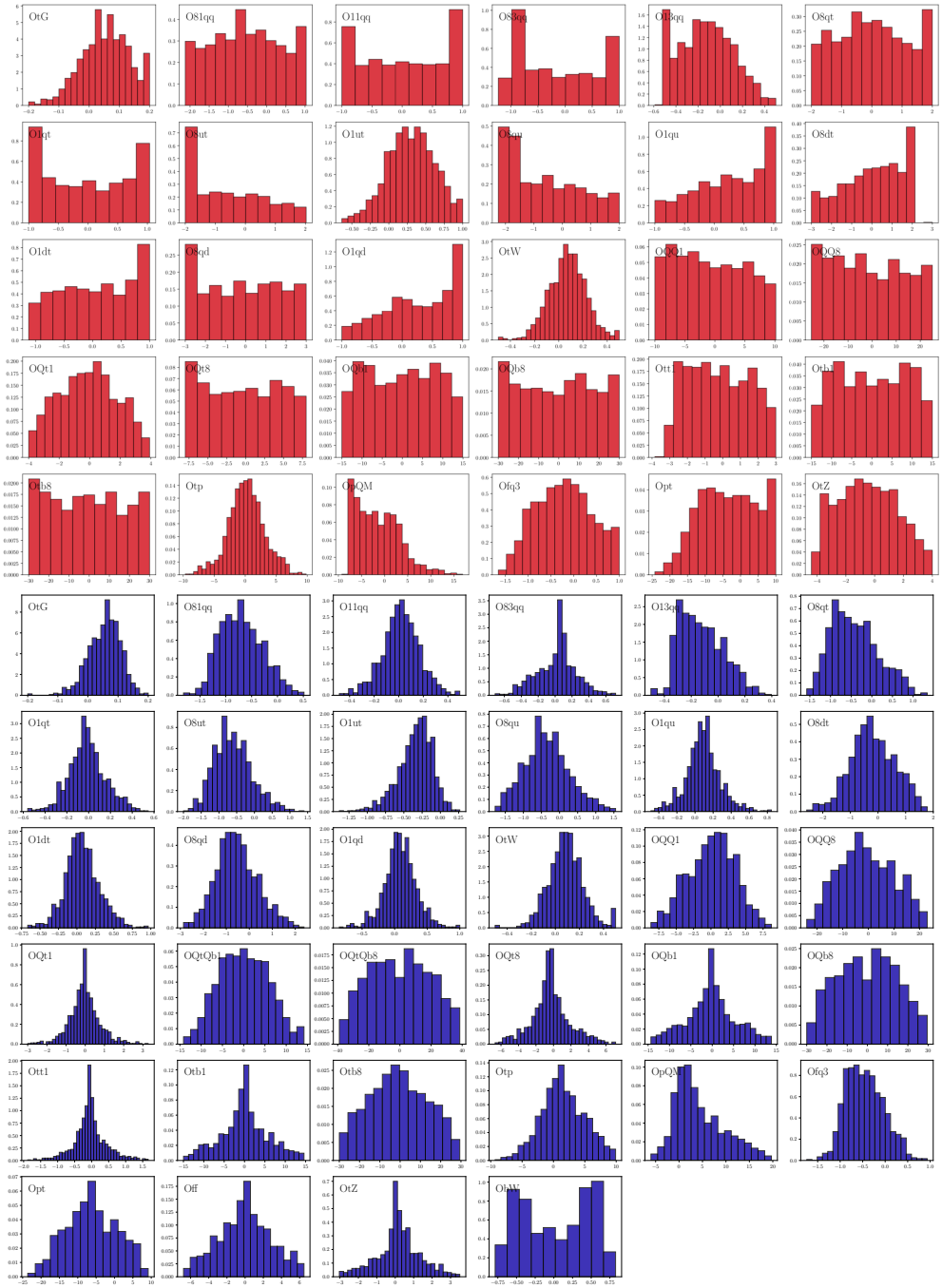

Figure 4.11: Red: Histograms showing the value found by 1000 replicas of a level 2 closure test for each degree of freedom excluding $\mathcal{O}\left(\Lambda^{-4}\right)$ corrections. Blue: Histograms showing the value found by 1000 replicas of a level 2 closure test for each degree of freedom including $\mathcal{O}\left(\Lambda^{-4}\right)$ corrections.

CHAPTER 5

SMEFiT analysis of the top sector

In this chapter we will apply the SMEFiT methodology to the top sector at dimension-6. We discussed in Sec. 2.2 the baseline theoretical framework we will use for our SMEFT analysis; namely the flavour symmetries we impose in order to reduce the number of parameters we need to fit. Whilst this is a suitable approach to take for the proof-of-concept work we will present here, it is quite restrictive to impose constraints on the kinds of new physics we expect, whilst simultaneously trying to determine its existence.

We therefore emphasise that, while the results we will present in this chapter currently constitute the widest fit to SMEFT operators performed, this is a first step towards a fully global fit. We discussed in Chapter 4 that SMEFiT is designed to be as flexible as possible, with no constraints on the number of operators that can be fitted. It is therefore trivial from the fitting point of view to relax the flavour constraints we imposed here, in order to fit all possible operators, and we will not discuss this further.

5.1 Experimental data and theoretical calculations

In this section we describe the experimental measurements which will be used to constrain the SMEFT operators related to the top sector. For each dataset we discuss its main features, the information that it provides on the SMEFT effects, and the treatment of experimental uncertainties.

5.1.1 Top quark production at the LHC

We constrain the top quark sector of the SMEFT by using experimental measurements from the LHC Run I at $\sqrt{s} = 8$ TeV and from Run II at $\sqrt{s} = 13$ TeV. We do not consider previous, less precise data at $\sqrt{s} = 7$ TeV nor data from the Tevatron. The measurements of top quark production at the LHC 7 TeV are superseded by the more precise 8 and 13 TeV ones and there is no loss of information incurred by not including them. There is a valid reason, however, for including Tevatron data as it provides information of the $q\bar{q}$ production channel of $t\bar{t}$ pair production. In this work we have focused on LHC data and leave the inclusion of the Tevatron constraints to a future iteration of our analysis.

The various experimental datasets used as input in this work are summarised in Tables 5.1, 5.2 and 5.3, for inclusive top quark pair production, $t\bar{t}$ production in association with gauge and Higgs bosons, and single top production measurements, respectively. For each dataset, we indicate the type of process, the centre-of-mass energy $\sqrt{s}$, the available observables, the number of data points $N_{\rm dat}$, and the corresponding publication reference.

In Fig. 5.1 we display representative Feynman diagrams at the Born level for the production of top quarks at the LHC in the channels that we consider in this analysis. Specifically, we show top quark pair production; single-top production in association with a W or Z boson and in the t- and s-channels; $t\bar{t}$ production in

Process	Dataset	$\sqrt{s}$	Observables	$N_{\rm dat}$	Ref
$t\bar{t}$	ATLAS_tt_8TeV_ljets	**8 TeV**	$d\sigma/d\|y_t\|$, $d\sigma/dp_t^T$, $d\sigma/dm_{t\bar{t}}$, $d\sigma/d\|y_{t\bar{t}}\|$	5, 8, 7, 5	[123]
$t\bar{t}$	CMS_tt_8TeV_ljets	**8 TeV**	$d\sigma/dy_t$, $d\sigma/dp_t^T$, $d\sigma/dm_{t\bar{t}}$, $d\sigma/dy_{t\bar{t}}$	10, 8, 7, 10	[124]
$t\bar{t}$	CMS_tt2D_8TeV_dilep	**8 TeV**	$d^2\sigma/dy_t dp_t^T$, $d^2\sigma/dy_t dm_{t\bar{t}}$, $d^2\sigma/dp_{t\bar{t}}^T dm_{t\bar{t}}$, $d^2\sigma/dy_{t\bar{t}} dm_{t\bar{t}}$	16, 16, 16, 16	[125]
$t\bar{t}$	CMS_tt_13TeV_ljets	**13 TeV**	$d\sigma/d\|y_t\|$, $d\sigma/dp_t^T$, $d\sigma/dm_{t\bar{t}}$, $d\sigma/d\|y_{t\bar{t}}\|$	7, 9, 8, 6	[126]
$t\bar{t}$	CMS_tt_13TeV_ljets2	**13 TeV**	$d\sigma/d\|y_t\|$, $d\sigma/dp_t^T$, $d\sigma/dm_{t\bar{t}}$, $d\sigma/d\|y_{t\bar{t}}\|$	11, 12, 10, 10	[127]
$t\bar{t}$	CMS_tt_13TeV_dilep	**13 TeV**	$d\sigma/dy_t$, $d\sigma/dp_t^T$, $d\sigma/dm_{t\bar{t}}$, $d\sigma/dy_{t\bar{t}}$	8, 6, 6, 8	[128]
$t\bar{t}$	ATLAS_WhelF_8TeV	**8 TeV**	F_0, F_L, F_R	3	[129]
$t\bar{t}$	CMS_WhelF_8TeV	**8 TeV**	F_0, F_L, F_R	3	[130]

Table 5.1: The experimental measurements of inclusive top quark pair production at the LHC considered in the present analysis to constrain the coefficients of the SMEFT dimension-6 operators in the top sector.

association with $t\bar{t}$ or $b\bar{b}$; and $t\bar{t}$ production in association with a W or Z gauge boson or with the Higgs boson H.

From these diagrams, one can see that measurements of inclusive top quark pair production will be particularly sensitive to SMEFT operators that induce or modify interactions of the form $gt\bar{t}$ and $ggt\bar{t}$, such as the chromomagnetic operator c_{tG}. Top-pair production in association with either a top-pair or a bottom-pair should provide direct information on operators involving four-heavy quarks, such as c_{QQ}^1 and c_{QQ}^8. Likewise, single-top production and associated tW and tZ production will constrain SMEFT operators that involve both top quarks and electroweak gauge bosons, such as c_{tW}.

Process	Dataset	$\sqrt{s}$	Observables	$N_{\rm dat}$	Ref
$t\bar{t}b\bar{b}$	CMS_ttbb_13TeV	**13 TeV**	$\sigma_{\rm tot}(t\bar{t}b\bar{b})$	1	[131]
$t\bar{t}t\bar{t}$	CMS_tttt_13TeV	**13 TeV**	$\sigma_{\rm tot}(t\bar{t}t\bar{t})$	1	[132]
$t\bar{t}Z$	CMS_ttZ_8_13TeV	**8+13 TeV**	$\sigma_{\rm tot}(t\bar{t}Z)$	2	[133, 134]
$t\bar{t}Z$	ATLAS_ttZ_8_13TeV	**8+13 TeV**	$\sigma_{\rm tot}(t\bar{t}Z)$	2	[135, 136]
$t\bar{t}W$	CMS_ttW_8_13TeV	**8+13 TeV**	$\sigma_{\rm tot}(t\bar{t}W)$	2	[133, 134]
$t\bar{t}W$	ATLAS_ttW_8_13TeV	**8+13 TeV**	$\sigma_{\rm tot}(t\bar{t}W)$	2	[135, 136]
$t\bar{t}H$	CMS_tth_13TeV	**13 TeV**	$\mu_{t\bar{t}H}$	1	[137]
$t\bar{t}H$	ATLAS_tth_13TeV	**13 TeV**	$\sigma_{\rm tot}(t\bar{t}H)$	1	[138]

Table 5.2: Same as Table 5.1 now for $t\bar{t}$ in association with heavy quarks, with weak vector bosons, and with the Higgs boson.

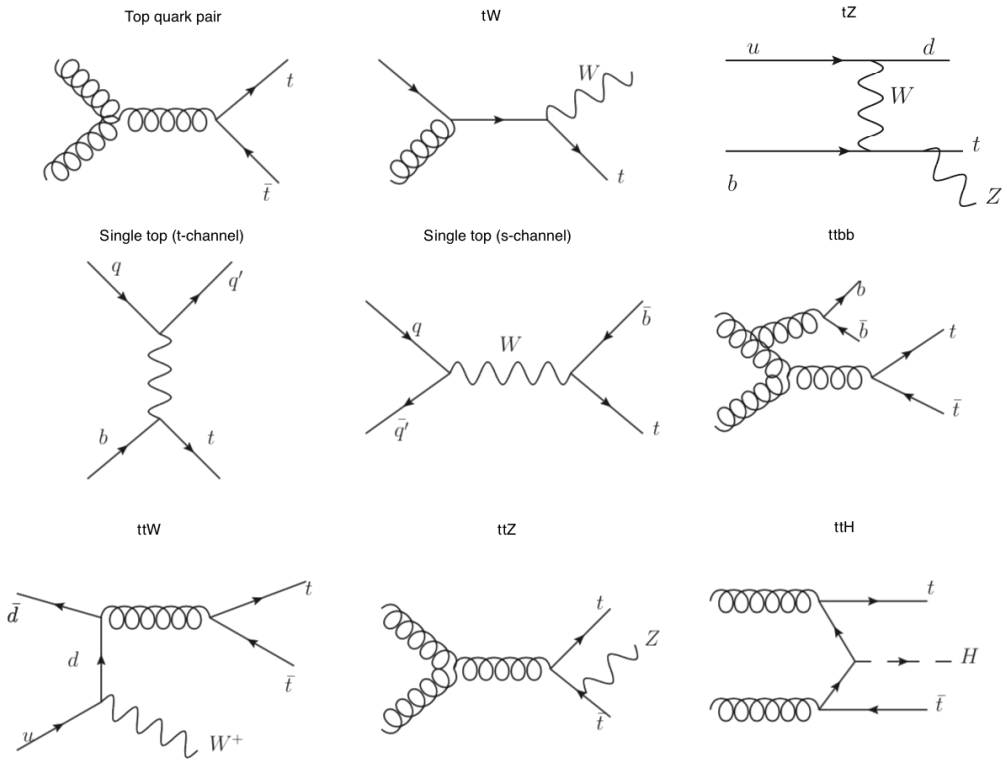

Figure 5.1: Representative Feynman diagrams at the Born level for the dominant production channels of top quarks at the LHC that are considered in the present SMEFT analysis.

Top-quark pair production

At the LHC, the dominant mechanism for the production of top quarks is through the production of $t\bar{t}$ pairs. The inclusive $t\bar{t}$ process is dominated by the gluon-

Process	Dataset	$\sqrt{s}$	Observables	$N_{\rm dat}$	Ref
Single t	CMS_t_tch_8TeV_inc	**8 TeV**	$\sigma_{\rm tot}(t), \sigma_{\rm tot}(\bar{t})$ (R_t)	2 (1)	[139]
Single t	CMS_t_sch_8TeV	**8 TeV**	$\sigma_{\rm tot}(t+\bar{t})$	1	[140]
Single t	ATLAS_t_sch_8TeV	**8 TeV**	$\sigma_{\rm tot}(t+\bar{t})$	1	[141]
Single t	ATLAS_t_tch_8TeV	**8 TeV**	$d\sigma(tq)/dp_T^t, d\sigma(\bar{t}q)/dp_T^{\bar{t}}$ $d\sigma(tq)/dy_t, d\sigma(\bar{t}q)/dy_t$	5, 4 4, 4	[142]
Single t	ATLAS_t_tch_13TeV	**13 TeV**	$\sigma_{\rm tot}(t), \sigma_{\rm tot}(\bar{t})$ (R_t)	2 (1)	[143]
Single t	CMS_t_tch_13TeV_inc	**13 TeV**	$\sigma_{\rm tot}(t+\bar{t})$ (R_t)	1 (1)	[144]
Single t	CMS_t_tch_8TeV_dif	**8 TeV**	$d\sigma/dp_T^{(t+\bar{t})}$, $d\sigma/d\lvert y^{(t+\bar{t})}\rvert$	6 6	[145]
Single t	CMS_t_tch_13TeV_dif	**13 TeV**	$d\sigma/dp_T^{(t+\bar{t})}$, $d\sigma/d\lvert y^{(t+\bar{t})}\rvert$	4 4	[146]
tW	ATLAS_tW_inc_8TeV	**8 TeV**	$\sigma_{\rm tot}(tW)$	1	[147]
tW	CMS_tW_inc_8TeV	**8 TeV**	$\sigma_{\rm tot}(tW)$	1	[148]
tW	ATLAS_tW_inc_13TeV	**13 TeV**	$\sigma_{\rm tot}(tW)$	1	[149]
tW	CMS_tW_inc_13TeV	**13 TeV**	$\sigma_{\rm tot}(tW)$	1	[150]
tZ	CMS_tZ_inc_13TeV	**13 TeV**	$\sigma_{\rm fid}(Wbl^+l^-q)$	1	[151]
tZ	ATLAS_tZ_inc_13TeV	**13 TeV**	$\sigma_{\rm tot}(tZq)$	1	[152]

Table 5.3: Same as Table 5.1, now for inclusive single t production and single t production in association with vector bosons.

gluon initial state, with a small admixture of the quark-antiquark partonic luminosity [153, 154]. In this analysis, we will limit ourselves to parton-level distributions, for which NNLO QCD corrections are available in the SM [155]. For all the inclusive $t\bar{t}$ processes computed here, the SM prediction is computed up to NNLO in the QCD coupling. Theoretical predictions are obtained at NLO with `Sherpa` [156], for 8 TeV measurements, and with `MCFM` [157], for 13 TeV measurements, and are then supplemented with the NNLO QCD K-factors computed in Ref. [158].

In the present analysis we include the ATLAS and CMS differential distribu-

tions from $t\bar{t}$ production at $\sqrt{s} = 8$ TeV in the lepton+jets final state [123, 124]. In addition, we take into account the constraints from the double-differential distributions from CMS at 8 TeV, which provide a good handle on the underlying partonic kinematics [125]. Note that this dataset is based on the dilepton final state, therefore it does not overlap with the dataset used in [124], which instead is based on the lepton+jets channel. We also include the CMS differential distributions at $\sqrt{s} = 13$ TeV in the lepton+jets [126] and dilepton [128] final states based on an integrated luminosity of $\mathcal{L} = 2.3$ fb^{-1}, as well as the more recent measurements in the lepton+jet channel based on $\mathcal{L} = 35.8$ fb^{-1} [127]. A measurement based on the same dataset but with the dilepton final state was presented in [159]. Double-differential distributions from CMS at 13 TeV [126] are excluded since they overlap with the single-inclusive distributions from the lepton+jets datasets.

We do not include ATLAS measurements at 13 TeV since the published differential cross sections at 13 TeV in the lepton+jets [160] and dilepton [161] channels are provided at the particle level. Note that in principle ATLAS measurements at 13 TeV are also available for the fully hadronic final state in the highly boosted regime [162]. These measurements are not considered here since their analysis requires jet substructure information alongside the consistent inclusion of electroweak [163] and threshold resummation [164] corrections.

A further window on the underlying dynamics of top quark pair production is provided by the measurement of observables sensitive to the spin structure of top quark production and decay. Among them, W helicity fractions provide direct constraints on the structure of the tWb vertex. In this work, we include the helicity fractions F_L, F_0, and F_R of the W bosons from the decay of top quarks measured by ATLAS [129] and CMS [130] at $\sqrt{s} = 8$ TeV. The helicity fraction variables are defined by the decomposition of the cross section of the W in its rest frame

$$\frac{1}{\sigma}\frac{\mathrm{d}\sigma}{\mathrm{d}\cos\theta^*} = \frac{3}{4}\left(1-\cos^2\theta^*\right)F_0 + \frac{3}{8}(1-\cos\theta^*)^2 F_L + \frac{3}{8}(1+\cos\theta^*)^2 F_R\,, \quad (5.1)$$

where θ^* is the angle between the direction of the down-type quark or charged lepton arising from the W decay and the reversed direction of the top quark.

$t\bar{t}V$ production

In this analysis we also include data for the production of a $t\bar{t}$ pair in association with either a Z or a W boson, which is directly sensitive to the top quark couplings with the gauge bosons (see Fig. 5.1). Specifically, we include the measurements of the total inclusive cross sections for $t\bar{t}Z$ and $t\bar{t}W$ production at $\sqrt{s} = 8$ TeV and $\sqrt{s} = 13$ TeV from ATLAS [135, 136] and CMS [133, 134]. Note that for $t\bar{t}W$, the W boson is often emitted from initial-state light quarks, however, when it is emitted from a final-state leg, it becomes sensitive to operators involving only one heavy quark, which is a unique feature of this process. We do not include the $t\bar{t}\gamma$ production measurements [165–167], whose interpretation is hampered by issues related to photon isolation and fragmentation, as well as to initial- and final-state radiation. We finally note that, the updated CMS measurement of $t\bar{t}Z$ production [168] will be included in a future iteration of the analysis.

Higgs production in association with a $t\bar{t}$ pair

The production of a $t\bar{t}$ pair together with a Higgs boson allows for a direct probe of the Yukawa coupling of the top quark, as illustrated by the dominant mechanism indicated in Fig. 5.1. Recently, 5σ evidence for this production mode was presented by both the ATLAS and CMS collaborations [137, 138]. In the CMS case [137], we utilise their measurement of the signal strength $\mu_{t\bar{t}H}$ at $\sqrt{s} = 13$ TeV (normalised to the SM prediction), rather than the cross section, because the latter is obtained by combining data at different centre-of-mass energies. In the ATLAS case [138], we utilise their measurement of the total cross section for $t\bar{t}H$ production at $\sqrt{s} = 13$, extrapolated to the full phase space.

$t\bar{t}b\bar{b}$ and $t\bar{t}t\bar{t}$ production

The production of a top quark pair in association with a $b\bar{b}$ pair is a purely QCD process, where a $b\bar{b}$ pair is radiated either from a gluon emitted from the initial state or from the final state (see Fig. 5.1). The production of four top quarks at the LHC, $t\bar{t}t\bar{t}$, obeys a similar underlying mechanism in the SM, with the cross section now being rather smaller due to the heavier top quark mass. The relevance of this process on the top quark sector of the SMEFT has been discussed in Ref. [72].

Concerning $t\bar{t}b\bar{b}$, the total cross section for $t\bar{t}b\bar{b}$ production, extrapolated to the full phase space at 13 TeV, is available from CMS [131], together with the corresponding ratio to $t\bar{t}jj$ production. This single data point is included in our fit. Differential cross sections for $t\bar{t}b\bar{b}$ production at $\sqrt{s} = 8$ TeV have also been presented as a function of the kinematics of the b-jets [169]. These measurements, however, are not included in the fit. While there is a priori no reason why these measurements of $t\bar{t}$ production in association with jets cannot be used in a SMEFT fit [170], this would require to interface the parton level calculation to a Monte Carlo shower program. In this work, we have chosen to focus on inclusive observables, and we have deferred more exclusive observables to future work.

The ATLAS collaboration has presented the results of the measurements of top quark pair production in association with multiple b-jets at $\sqrt{s} = 13$ TeV. Fiducial cross sections for $t\bar{t}$ in association with more than two b quarks, both in the lepton+jets and in the dilepton channels, are provided [171], which supersede a previous measurement at 8 TeV [172]. We do not include these results in the fit as the cuts needed to simulate the cross sections are not fully provided, and are therefore not reproducible.

Concerning $t\bar{t}t\bar{t}$, a first measurement of its cross section at $\sqrt{s} = 13$ TeV has been presented by CMS [132], albeit with a statistical significance of only 1.6σ. This measurement supersedes previous upper bounds at 8 TeV [173] and 13 TeV [174]. In the case of ATLAS, upper bounds based on the 2015 dataset at

13 TeV were presented in [175] and then updated in [176] from the 2016 dataset. In this analysis we utilise the CMS cross section measurement of [132]. The recent CMS measurements of $t\bar{t}t\bar{t}$ and $t\bar{t}b\bar{b}$ [177–179] will be included in a future analysis of the top sector.

Inclusive single top quark production

There exist three main modes to produce single top quarks [180]: by means of the exchange of a $W^{\pm}$ boson, either in the t-channel or in the s-channel, and by means of the associated production with a $W^{\pm}$ (Z) boson that leads to the $q't$, $t\bar{b}$, and $tW^{\pm}$ (tZq) Born-level final states. Representative diagrams for these three modes are shown in Fig. 5.1.

In this work, we include all relevant single top production datasets at the parton level in the $t-$ and $s-$channels from ATLAS and CMS at 8 and 13 TeV, see Table 5.3. From ATLAS, we include the differential cross sections at $\sqrt{s} = 8$ TeV [143], specifically the $d\sigma(tq)/dp_T^t$ and $d\sigma(tq)/dy_T^t$ distributions, as well as the corresponding measurements for anti-top quarks. From CMS, we include the inclusive cross sections for t and for $\bar{t}$ production at $\sqrt{s} = 8$ TeV [139], as well as the corresponding differential distributions in $p_T^{(t+\bar{t})}$ and $|y_{t+\bar{t}}|$ [145].

We now move to single top t-channel based on the Run II dataset at $\sqrt{s} = 13$ TeV. We include the transverse momentum $p_T^{t+\bar{t}}$ and rapidity $|y_{t+\bar{t}}|$ differential distributions for single top production from CMS [146], the ATLAS and CMS measurements of the total inclusive cross sections for single t and $\bar{t}$ production [143, 144]. The differential cross section measurements by CMS at 13 TeV [181] are additionally going to be included in a future analysis.

We include the CMS total cross sections in the s-channel at 8 TeV [140]. We also include the total cross sections at 8 TeV from ATLAS [141]. No measurements of s-channel single top production at 13 TeV are available from either experiment. Neither the ATLAS nor the CMS differential distributions at the time

of the analysis were provided with a full breakdown of experimental systematic uncertainties. Therefore, we sum all statistical and systematic uncertainties in quadrature. For both inclusive and differential single-top measurements in the t-channel which were published (i.e. not notes), NNLO QCD corrections have been computed [182]. For unpublished measurements, we use NLO QCD, as the NNLO results are not available.

tV associated production

Measurements of tW associated production have been presented by ATLAS and CMS. Here we include the ATLAS measurements at 8 and 13 TeV of the total $\sigma(tW)$ cross section [147,149] extrapolated to the full phase space. A measurement of differential distributions at 13 TeV based on a luminosity of $\mathcal{L} = 36$ fb^{-1} [183] was also presented by ATLAS. However, this measurement is at particle level (of leptons and b-jets from the W and top quark decays), therefore we do not include it in the fit. We also include the CMS measurements of $\sigma_{\rm tot}(tW)$ at 8 and 13 TeV [148, 150]. These measurements supersede the previous ones at 7 and 8 TeV [148, 184].

For tW production both the SM and SMEFT part is for consistency computed with the DR1 scheme [185]. We refer the reader to Ref. [186] for a detailed discussion of the differences between the various diagram subtraction/removal schemes. At the inclusive level the difference between the schemes is about 10% but this is greatly reduced with fiducial cuts. This uncertainty is comparable to the scale and PDF uncertainties and we do not expect it to significantly alter our findings.

The associated production of a single top quark in association with a Z boson, shown in Fig. 5.1, is also an interesting probe of the top quark sector of the SMEFT. The tZ production cross section has been measured by CMS at 13 TeV in the Wbl^+l^-q final state, where the dilepton pair arise from the decay of the Z

boson [151] (see [187] for an update based on $\mathcal{L} = 77.4$ fb^{-1}). The tZ production cross section has been measured at 13 TeV by ATLAS in the tri-lepton final state and extrapolated to the full phase space [152]. We use these two measurements as data points in the fit, for a total of four tV input cross sections. The combined ATLAS and CMS result for tW, $t-$ and $s-$channel production at 8 TeV [188] will be included in the future SMEFiT analysis.

5.2 Theory overview

In Table 5.4, we summarise the details of the theoretical calculations used for the description of the LHC top quark production measurements included in the present analysis. We indicate, for both the SM and the SMEFT contributions to the cross sections in Eq. (2.45), the perturbative accuracy and the codes used to produce the corresponding predictions. We do not include top quark data in the NNPDF PDF fit used as input, as the datasets used in NNPDF are also used in the current SMEFT fit. Adding $t\bar{t}$ distributions into both fits would cause us to double-count the data and it would require us to keep track of correlations between the replicas used in the PDF and SMEFT fits.

In Table 5.5 we indicate the sensitivity of each of the LHC processes included in the present analysis along with the degrees of freedom in our fitting basis (for their definition, see Table 2.1). A check mark outside (inside) brackets indicates that a given process constrains the corresponding operator $\mathcal{O}(\Lambda^{-2})$ ($\mathcal{O}(\Lambda^{-4})$). A check mark in square brackets indicates that the operator enters at $\mathcal{O}(\Lambda^{-2})$ but only at NLO.

The comparison in Table 5.5 illustrates the importance of a global approach to the SMEFT analysis of top quark production. On the one hand, several operators are constrained by many different processes, and this allows independent and complementary constraints. For instance, the chromomagnetic operator c_{tG} is

Process	SM	Code	SMEFT	Code
$t\bar{t}$	NNLO QCD	`MCFM/SHERPA` NLO + NNLO K-factors	NLO QCD	`MG5_aMC`
single-t (t-ch)	NNLO QCD	`MCFM` NLO + NNLO K-factors	NLO QCD	`MG5_aMC`
single-t (s-ch)	NLO QCD	`MCFM`	NLO QCD	`MG5_aMC`
tW	NLO QCD	`MG5_aMC`	NLO QCD	`MG5_aMC`
tZ	NLO QCD	`MG5_aMC`	LO QCD + NLO SM K-factors	`MG5_aMC`
$t\bar{t}W(Z)$	NLO QCD	`MG5_aMC`	LO QCD + NLO SM K-factors	`MG5_aMC`
$t\bar{t}h$	NLO QCD	`MG5_aMC`	LO QCD + NLO SM K-factors	`MG5_aMC`
$t\bar{t}t\bar{t}$	NLO QCD	`MG5_aMC`	LO QCD + NLO SM K-factors	`MG5_aMC`
$t\bar{t}b\bar{b}$	NLO QCD	`MG5_aMC`	LO QCD + NLO SM K-factors	`MG5_aMC`

Table 5.4: Summary of the theoretical calculations used for the description of the LHC top production cross-sections included in the present analysis.

relevant for the description of all the input processes with the exception of single-top production. On the other hand, other operators are constrained by one or two processes at most, so that information on them can be obtained only by including a wide range of different input observables. For instance, `Otp`, constrained only by $t\bar{t}H$ production; `ObW`, sensitive only to single-top production at $\mathcal{O}\left(\Lambda^{-4}\right)$; and the four-heavy quark operators for which the only available information is from $t\bar{t}b\bar{b}$ and $t\bar{t}t\bar{t}$. We also observe that adding the $\mathcal{O}(\Lambda^{-4})$ contributions from the dimension-6 operators increases the sensitivity of many different processes. The `OQtQb1`, `OQtQb8`, `ObW` and `Off` degrees of freedom can only be constrained once $\mathcal{O}(\Lambda^{-4})$ terms are included in the fit.

Notation	Sensitivity at $\mathcal{O}(\Lambda^{-2})$ ($\mathcal{O}(\Lambda^{-4})$)								
	$t\bar{t}$	single-top	tW	tZ	$t\bar{t}W$	$t\bar{t}Z$	$t\bar{t}H$	$t\bar{t}t\bar{t}$	$t\bar{t}b\bar{b}$
OQQ1								✓	✓
OQQ8								✓	✓
OQt1								✓	✓
OQt8								✓	✓
OQb1									✓
OQb8									✓
Ott1								✓	
Otb1									✓
Otb8									✓
OQtQb1									(✓)
OQtQb8									(✓)
O81qq	✓				✓	✓	✓	✓	✓
O11qq	[✓]				[✓]	[✓]	[✓]	✓	✓
O83qq	✓	[✓]		[✓]	✓	✓	✓	✓	✓
O13qq	[✓]	✓		✓	[✓]	[✓]	[✓]	✓	✓
O8qt	✓				✓	✓	✓	✓	✓
O1qt	[✓]				[✓]	[✓]	[✓]	✓	✓
O8ut	✓					✓	✓	✓	✓
O1ut	[✓]					[✓]	[✓]	✓	✓
O8qu	✓					✓	✓	✓	✓
O1qu	[✓]					[✓]	[✓]	✓	✓
O8dt	✓					✓	✓	✓	✓
O1dt	[✓]					[✓]	[✓]	✓	✓
O8qd	✓					✓	✓	✓	✓
O1qd	[✓]					[✓]	[✓]	✓	✓
OtG	✓		✓		✓	✓	✓	✓	✓
OtW		✓	✓	✓					
ObW		(✓)	(✓)	(✓)					
OtZ				✓		✓			
Off		(✓)	(✓)	(✓)					
Ofq3		✓	✓	✓					
OpQM				✓		✓			
Opt				✓		✓			
Otp							✓		

Table 5.5: The sensitivity of each of the LHC processes included in the present analysis with each of the $N_{\rm obs} = 34$ dimension-six SMEFT operators that constitute our fitting basis (see Table 2.1 for their definition).

5.2.1 NLO QCD effects in the SMEFT calculation

In Eq. (2.45), the coefficients σ_i and $\widetilde{\sigma}_{ij}$ can be evaluated at either leading order in both the QCD and electroweak couplings, or by also including higher-order perturbative corrections. Given the high precision of available top quark measurements, particularly from the LHC Run II, as well as the further improvements expected at Run II and during the High-Luminosity (HL) LHC, it is important to take into account the NLO QCD corrections to SMEFT effects. This is necessary for a number of reasons, including:

- The corrections can be quite large and taking them into account results in general in a more realistic estimation of the bounds on the Wilson coefficients.
- NLO QCD corrections reduce the theoretical uncertainties from scale variations, which is helpful in discriminating between different BSM scenarios.
- QCD corrections can distort the distributions of key observables. Given that differential distributions play an important role in SMEFT global fits, providing reliable predictions for them is crucial. For instance, it is shown in Ref. [63] that in the presence of a deviation from the SM, missing QCD corrections to certain differential distributions could lead us to make incorrect conclusions on the nature of BSM physics.
- The experimental sensitivity to SM deviations can be improved by using the most accurate SMEFT predictions. However, the large QCD corrections at the LHC make this improvement unrealistic without consistently taking into account NLO predictions.

Motivated by the above considerations, theoretical calculations in the SMEFT at NLO in the QCD perturbative expansion have started to appear. For instance, computations including higher dimensional operators for top-related processes have been presented in [61–67], and those for Higgs and electroweak processes

in [189–195]. In particular, based on the machinery of automatic computations in `MadGraph5_aMC@NLO`, a systematic framework for including higher-dimensional operators at NLO has been established through the studies of Refs. [61–67], and the implementation of the full set of dimension-6 SMEFT operators is currently being studied.

We will exploit this framework and include the theoretical predictions at NLO in QCD whenever possible. This allows us to obtain the most accurate bounds on the coefficients of the SMEFT operators affecting the top quark couplings. Furthermore, by switching on and off the NLO QCD corrections in the fit, we can understand better the importance of the higher-order corrections in the SMEFT calculation when constraining different operators.

Of all the degrees of freedom relevant in this work, the operators involving only two fermion fields have been fully automated already in this framework. It is therefore possible to straightforwardly evaluate their associated NLO QCD corrections. Four-fermion operators are being studied, and their complete implementation is expected to be publicly available in a short timescale. In this work we will include the NLO QCD corrections to the four-fermion operators only in the inclusive single top and top-pair production processes, which are the most accurately measured processes.

One practical difficulty in obtaining stable numerical results at NLO is that the residual uncertainties arising from the numerical Monte Carlo integration of the cross sections, for the interference terms σ_i and in the cross terms $\widetilde{\sigma}_{ij}, i \neq j$ can be large. Given the large number of SMEFT operators relevant for the description of top quark measurements, a full simulation at NLO QCD would be very time consuming.

In this work, we adopt the following strategy:

- For $t\bar{t}$ and single top production, the experimental measurements exhibit the highest precision. We therefore use the full NLO simulation.

- For associated production processes, the measurements are less accurate. We generate the full LO predictions using the implementation provided in [54]. We then apply K-factors from previous calculations of $t\bar{t}Z$, $t\bar{t}H$ and tZj production, wherever available [64–66]. For contributions or processes that have not been previously calculated (e.g. contributions from the four-fermion operators, and $t\bar{t}b\bar{b}$ and $tt\overline{tt}$ processes), we simply apply the SM K-factor.

- The W-helicity in top quark decay is available at NLO in the form of analytical results [196].

In Sec. 5.3.3 we will assess the stability of our results with respect to the inclusion or not of NLO QCD corrections to the SMEFT dimension-6 effects.

5.3 The top quark sector of the SMEFT at NLO

In this section we will present the main results of this chapter; presenting the constraints on the $N_{\rm op} = 34$ SMEFT dimension-6 degrees of freedom relevant for the interpretation of top quark production measurements at the LHC. We will first assess the fit quality and then present the best-fit values, the 95% confidence level intervals and the correlations for these degrees of freedom, and we will compare our results with other related analyses in the literature. We will then study the impact that both NLO QCD perturbative corrections and quadratic $\mathcal{O}\left(\Lambda^{-4}\right)$ terms have on the results. Finally, we assess the dependence of the fit results on the choice of input dataset.

5.3.1 Fit quality

As discussed in Chapter 4, our baseline fit is based on $N_{\rm rep} = 1000$ Monte Carlo replicas and includes both NLO QCD corrections for the SMEFT contributions and the quadratic $\mathcal{O}\left(\Lambda^{-4}\right)$ higher order terms.

In Table 5.6 we indicate the values of the χ^2 per datapoint for each of the datasets included in the fit. In each case, we indicate the values of $\chi^2/n_{\rm dat}$ first when the theory calculations include only the SM contributions (second column) and then once they account for the SMEFT corrections after the fit (third column). In the last column, we indicate the number of data points $n_{\rm dat}$ for each dataset. The datasets are classified into three groups following the structure of Tables 5.1–5.3: inclusive $t\bar{t}$, $t\bar{t}$ in association with V, H, or heavy quarks, and single top production. In the case of datasets consisting of multiple differential distributions, we indicate the one that has been included in this analysis.

We find that the overall fit quality to the $n_{\rm dat} = 103$ data points included in the fit is satisfactory, with $\chi^2/n_{\rm dat} = 1.04$ (1.11) after (before) the fit. We find therefore a slight improvement in the overall fit quality once the dimension-6 SMEFT corrections are taken into account. For most of the datasets, the SM description of the input measurements is already good to begin with. In several cases, the χ^2, Eq. (4.1), decreases once the SMEFT corrections are accounted for. For instance, the CMS $m_{t\bar{t}}$ distribution at 13 TeV improves from $\chi^2/n_{\rm dat} = 1.87$ to 0.93, and the CMS tW cross section improves from $\chi^2/n_{\rm dat} = 4.29$ to 2.63.

As expected in a global fit for some datasets the overall fit quality is unchanged or worsened as compared to the SM prediction, to allow for the addition of the Wilson coefficients. From Table 5.6, we notice that the only experiment for which the $\chi^2/n_{\rm dat}$ worsens significantly after the fit is the CMS $t\bar{t}Z$ cross section measurement at 8 TeV, whose SM value of $\chi^2/n_{\rm dat} = 0.04$ increases to 2.65 after the fit. The origin of this poor χ^2 value can be traced back to some tension between the ATLAS and CMS measurements of the same observable. At 13 TeV, however, both the ATLAS and CMS datasets are more poorly described upon the addition of the SMEFT contribution, beyond the level expected by statistical fluctuations. We will return to this point when we discuss the fits with theoretical variations.

Dataset	$\chi^2/n_{\rm dat}$ (prior)	$\chi^2/n_{\rm dat}$ (fit)	$n_{\rm dat}$
ATLAS_tt_8TeV_ljets [$m_{t\bar{t}}$]	1.51	1.45	7
CMS_tt_8TeV_ljets [$y_{t\bar{t}}$]	1.17	1.02	10
CMS_tt2D_8TeV_dilep [$(m_{t\bar{t}}, y_t)$]	1.38	1.38	16
CMS_tt_13TeV_ljets2 [$m_{t\bar{t}}$]	1.09	1.24	8
CMS_tt_13TeV_dilep [$m_{t\bar{t}}$]	1.34	1.40	6
CMS_tt_13TeV_ljets_2016 [$m_{t\bar{t}}$]	1.87	0.93	10
ATLAS_WhelF_8TeV	1.98	1.43	3
CMS_WhelF_8TeV	0.31	0.55	3
CMS_ttbb_13TeV	5.00	4.84	1
CMS_tttt_13TeV	0.05	0.03	1
ATLAS_tth_13TeV	1.61	1.60	1
CMS_tth_13TeV	0.34	0.89	1
ATLAS_ttZ_8TeV	1.32	0.23	1
ATLAS_ttZ_13TeV	0.01	1.24	1
CMS_ttZ_8TeV	0.04	2.65	1
CMS_ttZ_13TeV	0.91	1.69	1
ATLAS_ttW_8TeV	1.34	1.87	1
ATLAS_ttW_13TeV	0.82	0.95	1
CMS_ttW_8TeV	1.54	1.99	1
CMS_ttW_13TeV	0.03	0.20	1
CMS_t_tch_8TeV_dif	0.11	0.37	6
ATLAS_t_tch_8TeV [y_t]	0.91	0.40	4
ATLAS_t_tch_8TeV [$y_{\bar{t}}$]	0.39	0.33	4
ATLAS_t_sch_8TeV	0.08	0.03	1
ATLAS_t_tch_13TeV	0.02	0.06	2
CMS_t_tch_13TeV_dif [y_t]	0.46	0.51	4
CMS_t_sch_8TeV	1.26	1.50	1
ATLAS_tW_inc_8TeV	0.02	0.01	1
CMS_tW_inc_8TeV	0.00	0.03	1
ATLAS_tW_inc_13TeV	0.52	0.69	1
CMS_tW_inc_13TeV	4.29	2.63	1
ATLAS_tZ_inc_13TeV	0.00	0.03	1
CMS_tZ_inc_13TeV	0.66	0.63	1
Total	**1.11**	**1.04**	**103**

Table 5.6: The values of the χ^2 per data point for each of the datasets included in the fit. In the case of datasets made of multiple differential distributions, we indicate the one that has been used in the analysis.

5.3.2 Baseline results

We now present the fit results for the central values and the corresponding 95% CL uncertainties, δc_i, for the $N_{\rm op} = 34$ dimension-6 SMEFT degrees of freedom relevant for the interpretation of top quark production measurements at the LHC. We also study the cross-correlations between these degrees of freedom. They provide an important piece of information since we know from the closure tests of Sec. 4.2 that these correlations might be large because of flat directions in the parameter space.

In Fig. 5.2 we display the best-fit values and 95% confidence intervals of the $N_{\rm op} = 34$ degrees of freedom. In the bottom plot we show the associated fit residuals r_i, Eq. (4.11), which measure the deviation of the fit results with respect to the SM in units of the uncertainties. We find that, for most of the coefficients, there is very good agreement with the SM, with the fit residuals generally satisfying $|r_i| \leq 0.5$, which approximately corresponds to the 68% confidence level interval. A clear deviation from this is the coefficient associated to `O1ut`; the residual for this coefficient is ~ -2.0. We can see the reason for this apparent deviation from the SM in the top plot of Fig. 5.2, the central value is, like with many of the operators, $\neq 0$, but the uncertainty is so small on this degree of freedom that the 95% confidence intervals also do not touch the SM line.

Whilst naively one might rejoice and claim that we have officially found BSM physics in the top sector at the 4σ level (since we are in units of the 95% confidence interval, which roughly corresponds to 2σ), one must look at this result with a critical eye. We discussed in Sec. 4.1.2 that we do not account for MHOU in our framework, which, while we aim to reduce their impact by using high order theory, still play a role. Furthermore, `O1ut` is constrained by $t\bar{t}b\bar{b}$ production and the χ^2 from Table 5.6 for the SM datapoint is 5.00, with the experimental cross section being $4.0 \pm 0.6^{(\rm stat)} \pm 1.3^{(\rm syst)}$ pb [131], whereas the central SM theory point is 7.2 pb. Importantly, the χ^2 does not significantly decrease upon the addition

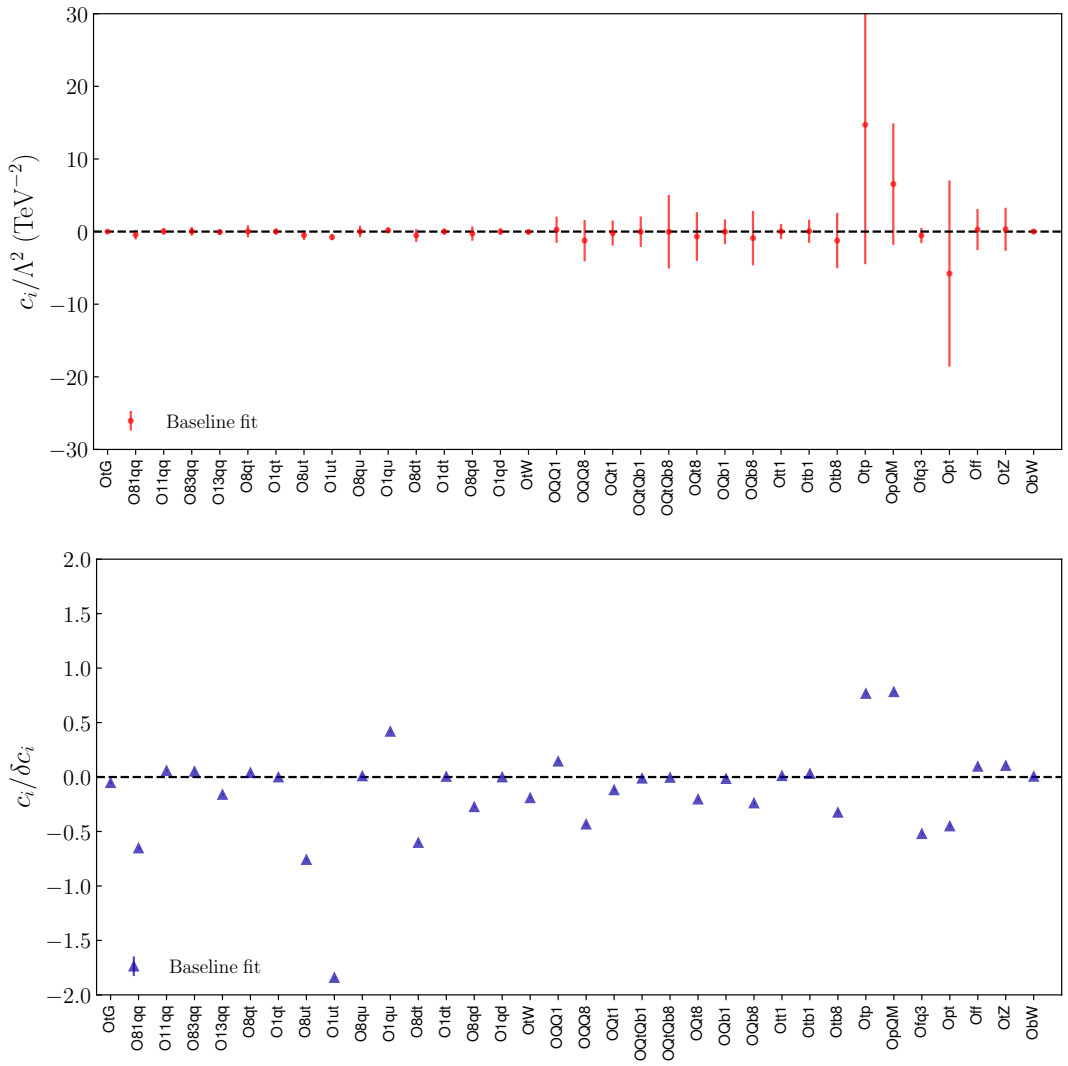

Figure 5.2: Top: Central value and 95% confidence level intervals for the baseline fit to the top sector. Bottom: the associated fit residuals where δc_i corresponds to the 95% confidence level interval.

of the SMEFT operators, it only goes down to 4.84. This means that this poor description of the data point is not caused by new physics in the top sector (at least in our framework), but rather due to a poor agreement between experiment and the theory. This means we expect this discrepancy to go away upon the addition of additional data which constrain `O1ut`.

We can also see from Fig. 5.2 that there is a wide range of values for the fit uncertainties obtained for the different degrees of freedom. For example, a

very small uncertainty is found for the coefficients associated to `OtG` and the two-heavy-two-light quark degrees of freedom, while much larger uncertainties are obtained for the fit coefficients associated to other degrees of freedom, including the four-heavy quark operators, such as `OQQ1`, and for some of the degrees of freedom including gauge bosons, such as `Opt` and `Otp`. The origin of these differences in the size of the uncertainties can be traced back to Table 5.5. Different degrees of freedom are constrained by different processes, and in each case the available amount of experimental information varies widely. Most of the data points in our analysis are from $t\bar{t}$ pair production differential distributions, which constrain `OtG` and the two-heavy-two-light quark degrees of freedom. In addition, the four-heavy quark operators are constrained by only two data points (the $t\bar{t}b\bar{b}$ and $t\bar{t}t\bar{t}$ cross sections), hence the large uncertainties of the associated coefficients. Likewise, `Otp` is only constrained from the $t\bar{t}H$ cross section measurements and `Opt` from tZ and $t\bar{t}Z$.

The interpretation of the 95% CL uncertainties shown in Fig. 5.2 requires some care. The reason is that the available data on top production at the LHC, summarised in Tables 5.1–5.3, does not allow us to fully separate all possible independent directions in the SMEFT parameter space. As a consequence, as illustrated in Sec. 4.2 at the closure test level, there will be in general large (anti-)correlations between the fit parameters, reflecting this degeneracy in the parameter space. To quantify this point, in Fig. 5.3 we show a heat map indicating the values of the correlation coefficient, Eq. (4.12), between the 34 degrees of freedom constrained from the fit. We find that overall there are only a few degrees of freedom which are significantly (anti-)correlated, suggesting we are able to separate the majority of the independent directions in the parameter space. By adding different types of processes to the fit we will be able to break the remaining degeneracies; for example, adding jet data will enable us to constrain `OtG` separately from other degrees of freedom.

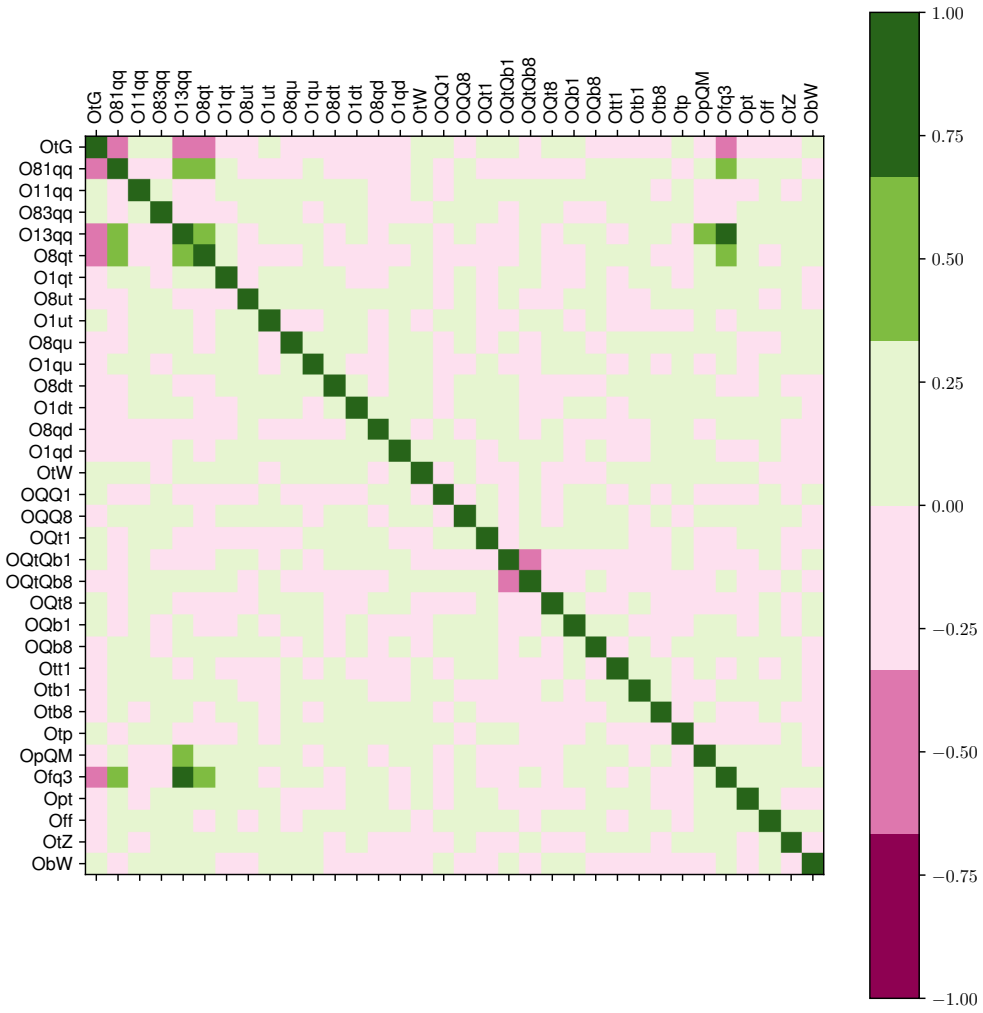

Figure 5.3: Heat map indicating the values of the correlation coefficient $\rho(c_i, c_j)$ between the $N_{\rm op} = 34$ fitted coefficients shown in Fig. 5.2.

Given the overall agreement between the fit results and the SM, it becomes possible to interpret the uncertainties as upper bounds on the parameter space of the SMEFT degrees of freedom. Such upper bounds provide important information for BSM model building, since they need to be satisfied for any UV-complete theory at high energies that has the SM as the low-energy effective theory. These bounds can also be compared with previous SMEFT studies of the top quark sector reported in the literature. Whilst on the one hand our global SMEFT analysis is based on a wider LHC dataset than previous analyses of top quark production, it explores a larger parameter space with reduced model assumptions.

Therefore, a priori, one could either expect stronger (from the larger dataset) or weaker (from the reduction in model assumptions) bounds as compared to previous studies: only performing the actual fit itself can shed light on this question.

In order to compare with previous results, we will follow here the discussion in Appendix A of the Top LHC Working Group EFT note [54], to which we direct the reader for further details. We note that the results quoted in [54] are in many cases restricted to fitting one operator at a time, or at most marginalising over a small subset of operators, and thus these limits might be too optimistic due to neglecting correlations with other directions in the SMEFT parameter space. We will quote here both the direct limits obtained from the top quark measurements, and the indirect limits derived from non-top processes such as low-energy observables, the decays of B mesons, electroweak precision observables, and Drell-Yan production.

In Table 5.7 we report the values of the 95% confidence level bounds for the coefficients derived from the marginalisation of the results of the SMEFiT global analysis. We compare our results with those obtained elsewhere in the literature either from the direct analysis of top quark production ("direct") or from indirect bounds from other processes not involving top quarks ("indirect"). We note that for several degrees of freedom, such as for `Off` and for many of the four-heavy quark degrees of freedom, the bounds reported here have been obtained for the first time.

Notation	DoF	**SMEFiT** (marginalised)	Direct (other)	Indirect (other)
OQQ1	c_{QQ}^{1}	$[-1.5, 1.9]$		
OQQ8	c_{QQ}^{8}	$[-4.1, 2.0]$		
OQt1	c_{Qt}^{1}	$[-1.9, 1.7]$	$[-5.0, 4.9]$ [197]	
OQt8	c_{Qt}^{8}	$[-3.7, 2.4]$	$[-10.3, 9.3]$ [197]	
OQb1	c_{Qb}^{1}	$[-1.7, 1.3]$		
OQb8	c_{Qb}^{8}	$[-4.5, 3.1]$		
Ott1	c_{tt}^{1}	$[-1.0, 1.0]$	$[-2.9, 2.8]$ [197]	
Otb1	c_{tb}^{1}	$[-1.8, 1.3]$		
Otb8	c_{tb}^{8}	$[-4.7, 2.5]$		
OQtQb1	c_{QtQb}^{1}	$[-3.1, 2.0]$		
OQtQb8	c_{QtQb}^{8}	$[-4.7, 5.1]$		
O81qq	$c_{Qq}^{1,8}$	$[-1.1, 0.2]$	$[-6.9, 4.9]$ [197]	
O11qq	$c_{Qq}^{1,1}$	$[-0.4, 0.5]$	$[-3.1, 3.2]$ [197]	
O83qq	$c_{Qq}^{3,8}$	$[-0.6, 0.6]$	$[-6.1, 6.7]$ [197]	
O13qq	$c_{Qq}^{3,1}$	$[-0.5, 0.3]$	$[-0.7, 1.2]$ [75]	
O8qt	c_{tq}^{8}	$[-0.8, 0.9]$	$[-6.8, 3.5]$ [197]	
O1qt	c_{tq}^{1}	$[-0.4, 0.4]$	$[-2.8, 2.8]$ [197]	
O8ut	c_{tu}^{8}	$[-1.1, 0.2]$	$[-8.0, 4.8]$ [197]	
O1ut	c_{tu}^{1}	$[-1.2, -0.3]$	$[-3.6, 3.5]$ [197]	
O8qu	c_{Qu}^{8}	$[-0.7, 0.8]$	$[-8.1, 4.0]$ [197]	
O1qu	c_{Qu}^{1}	$[-0.2, 0.6]$	$[-3.3, 3.4]$ [197]	
O8dt	c_{td}^{8}	$[-1.4, 0.4]$	$[-12, 9.3]$ [197]	
O1dt	c_{td}^{1}	$[-0.4, 0.4]$	$[-4.9, 5.0]$ [197]	
O8qd	c_{Qd}^{8}	$[-1.2, 0.8]$	$[-11.8, 9.4]$ [197]	
O1qd	c_{Qd}^{1}	$[-0.4, 0.5]$	$[-5.0, 5.0]$ [197]	
OtG	c_{tG}	$[-0.1, 0.1]$	$[-1.3, 1.2]$ [75]	
OtW	c_{tW}	$[-0.3, 0.2]$	$[-4.0, 3.5]$ [75]	$[-2.8, 2.0]$ (EW)
ObW	c_{bW}	$[-0.3, 0.3]$		$[-15, 37]$ (EW)
OtZ	c_{tZ}	$[-2.7, 3.2]$	c_{tB}: $[-4.1, 4.1]$ [198]	c_{tB}: $[-5.8, 15.4]$ (EW)
Off	$c_{\varphi tb}$	$[-2.6, 3.1]$		
Ofq3	$c_{\varphi Q}^{3}$	$[-1.6, 0.5]$	$[-4.1, 2.0]$ [75]	
OpQM	$c_{\varphi Q}^{-}$	$[-1.7, 14.5]$	$c_{\varphi Q}^{1}$: $[-3.1, 3.1]$ [75]	$[-3.4, 7.4]$ (EW)
Opt	$c_{\varphi t}$	$[-19.1, 7.4]$	$[-9.7, 8, 3]$ [75]	$[-2.0, 5.6]$ (EW)
Otp	$c_{t\varphi}$	$[-4.4, 33.8]$		

Table 5.7: The 95% confidence level bounds for the coefficients of the 34 SMEFT degrees of freedom used in the analysis. We also quote results obtained from the direct and indirect analyses.

SMEFiT individual bounds (single-operator fits)

Notation	DoF	Baseline	$\mathcal{O}(\Lambda^{-2})$ only	LO QCD
OQQ1	c_{QQ}^{1}	$[-3.5, 3.3]$	$[-54, 33]$	$[-4.0, 3.7]$
OQQ8	c_{QQ}^{8}	$[-10.3, 9.2]$	$[-200, 18]$	$[-11.8, 10.5]$
OQt1	c_{Qt}^{1}	$[-2.8, 2.8]$	$[-610, 210]$	$[-3.4, 3.4]$
OQt8	c_{Qt}^{8}	$[-8.7, 8.4]$	$[-69, 28]$	$[-7.3, 6.4]$
OQb1	c_{Qb}^{1}	$[-10.6, 10.3]$	$[-1.9 \cdot 10^{3}, -100]$	$[-9.2, 9.6]$
OQb8	c_{Qb}^{8}	$[-23.7, 19.0]$	$[-260, -14]$	$[-21.6, 17.7]$
Ott1	c_{tt}^{1}	$[-1.7, 1.6]$	$[-26, 41]$	$[-2.1, 1.9]$
Otb1	c_{tb}^{1}	$[-10.2, 10.5]$	$[-2.1 \cdot 10^{4}, -1.4 \cdot 10^{3}]$	$[-9.5, 9.2]$
Otb8	c_{tb}^{8}	$[-25.3, 20.0]$	$[-270, -15]$	$[-21.9, 17.7]$
OQtQb1	c_{QtQb}^{1}	$[-8, 7, 8.4]$	$*$	$[-7.5, 7.5]$
OQtQb8	c_{QtQb}^{8}	$[-22.4, 22.6]$	$*$	$[-19.4, 19.4]$
O81qq	$c_{Qq}^{1,8}$	$[-1.0, 0.2]$	$[-0.8, 0.2]$	$[-1.1, 0.1]$
O11qq	$c_{Qq}^{1,1}$	$[-0.0, 0.0]$	$[-0.0, 0.0]$	$[-0.0, 0.0]$
O83qq	$c_{Qq}^{3,8}$	$[-0.6, 0.0]$	$[-0.6, 0.0]$	$[-0.6, 0.0]$
O13qq	$c_{Qq}^{3,1}$	$[-0.0, 0.0]$	$[-0.0, 0.0]$	$[-0.0, 0.0]$
O8qt	c_{tq}^{8}	$[-0.6, 0.5]$	$[-0.8, 0.9]$	$[-1.0, 0.1]$
O1qt	c_{tq}^{1}	$[-0.0, 0.0]$	$[-0.0, 0.0]$	$[-0.0, 0.0]$
O8ut	c_{tu}^{8}	$[-1.5, 0.0]$	$[-1.6, -0.7]$	$[-1.2, 0.0]$
O1ut	c_{tu}^{1}	$[-1.6, 0.0]$	$[-1.7, 0.0]$	$[-1.7, 0.0]$
O8qu	c_{Qu}^{8}	$[-0.9, 0.5]$	$[-3.4, 0.4]$	$[-1.3, 0.1]$
O1qu	c_{Qu}^{1}	$[-0.2, 0.4]$	$[0.0, 1.9]$	$[-0.3, 0.3]$
O8dt	c_{td}^{8}	$[-1.4, 0.4]$	$[-4.0, -0.3]$	$[-1.5, 0.2]$
O1dt	c_{td}^{1}	$[-0.4, 0.3]$	$[-3.6, 1.2]$	$[-0.5, 0.3]$
O8qd	c_{Qd}^{8}	$[-1.4, 0.6]$	$[-3.2, 0.7]$	$[-1.5, 0.3]$
O1qd	c_{Qd}^{1}	$[-0.3, 0.4]$	$[-1.2, 3.2]$	$[-0.3, 0.5]$
OtG	c_{tG}	$[-0.0, 0.0]$	$[-0.0, 0.0]$	$[-0.0, 0.0]$
OtW	c_{tW}	$[-0.0, 0.0]$	$[-0.0, 0.0]$	$[-0.0, 0.0]$
ObW	c_{bW}	$[-0.4, 0.0]$	$*$	$[-0.4, 0.0]$
OtZ	c_{tZ}	$[-2.0, 2.1]$	$[-18.4, 5.3]$	$[-2.2, 2.2]$
Off	$c_{\varphi tb}$	$[-3.5, 3.5]$	$*$	$[-3.7, 3.7]$
Ofq3	$c_{\varphi Q}^{3}$	$[-0.6, 0.3]$	$[-0.6, 0.3]$	$[-0.6, 0.3]$
OpQM	$c_{\varphi Q}^{-}$	$[-2.7, 2.4]$	$[-3.0, 2.1]$	$[-3.1, 2.6]$
Opt	$c_{\varphi t}$	$[-18.6, -9.1]$	$[-3.2, 4.9]$	$[-21.0, -11.2]$
Otp	$c_{t\varphi}$	$[-4.0, 0.7]$	$[-4.5, 0.7]$	$[-4.3, 0.8]$

Table 5.8: Comparing the results obtained using different theory settings for individual fits. Bounds which are $[-0, 0]$ indicate the bound is tighter than the precision shown.

As recommended in [54], it is important to also quote the bounds derived from fitting individual coefficients, one at a time, in order to compare them with the global fit results. The results from such single-operator fits are provided in Table 5.8 using the same settings as in the baseline global fit (as well as by varying the theory settings, which we will discuss in Sec. 5.3.3).

The four-heavy quark operators are all affected by a large numerical instability, due to the fact that all of these operators are constrained by at most two data points. This can clearly be seen in Fig. 5.4 where we compare the results of the baseline global and individual fits, with those reported in [54]. We see that, for the four-heavy quark degrees of freedom, the individual bounds are in all cases looser than the global bounds. This is not a true feature of the fits but rather a bug, as within the single-operator fits one is neglecting cross-correlations between the different fitted degrees of freedom and therefore must always have tighter bounds, within statistical fluctuations.

For the purposes of visualisation only, we have symmetrised the bounds; that is, if a given operator has a 95% CL bound of $\left[\delta c_i^{(\min)}, \delta c_i^{(\max)}\right]$, then we show

$$\overline{\delta c_i} \equiv \left(\delta c_i^{(\max)} - \delta c_i^{(\min)}\right)/2\,. \tag{5.2}$$

As the bounds obtained for the four-heavy quark degrees of freedom are unreliable, given the small number of data points, we will focus on other bounds. We find that for some of the fitted degrees of freedom our bounds are stronger than those reported in previous studies, in some cases such as for `ObW` by nearly two orders of magnitude. Furthermore we see roughly an order of magnitude reduction in the bounds across the two-heavy-two-light quark sector compared to previous results. As discussed above, the individual bounds are not expected to be significantly tighter for these degrees of freedom, due to the lack of correlations in this sector of the SMEFT for our dataset.

In the boson+top sector, we also find an improvement in nearly all bounds with respect to the Top WG note. The individual bound for `OtG` is below the

level of precision which we quote, which is why it is absent in Fig. 5.4. This is because, as shown in the heat map in Fig. 5.3, `OtG` is strongly (anti-)correlated to several other degrees of freedom, which means the individual bound for `OtG` will be significantly tighter than its marginalised one. Looking to the rest of the sector, there are several constraints which were not reported in the Top WG note. For those where we do have a comparison, we find tighter bounds for all degrees of freedom except for `Opt` which is constrained by tZ and $t\bar{t}Z$ production. The bound reported in the note is that of the TopFitter group [75]; they include $t\bar{t}\gamma$ production measurements, and therefore are much more sensitive to the degrees of freedom which are additionally constrained by this process.

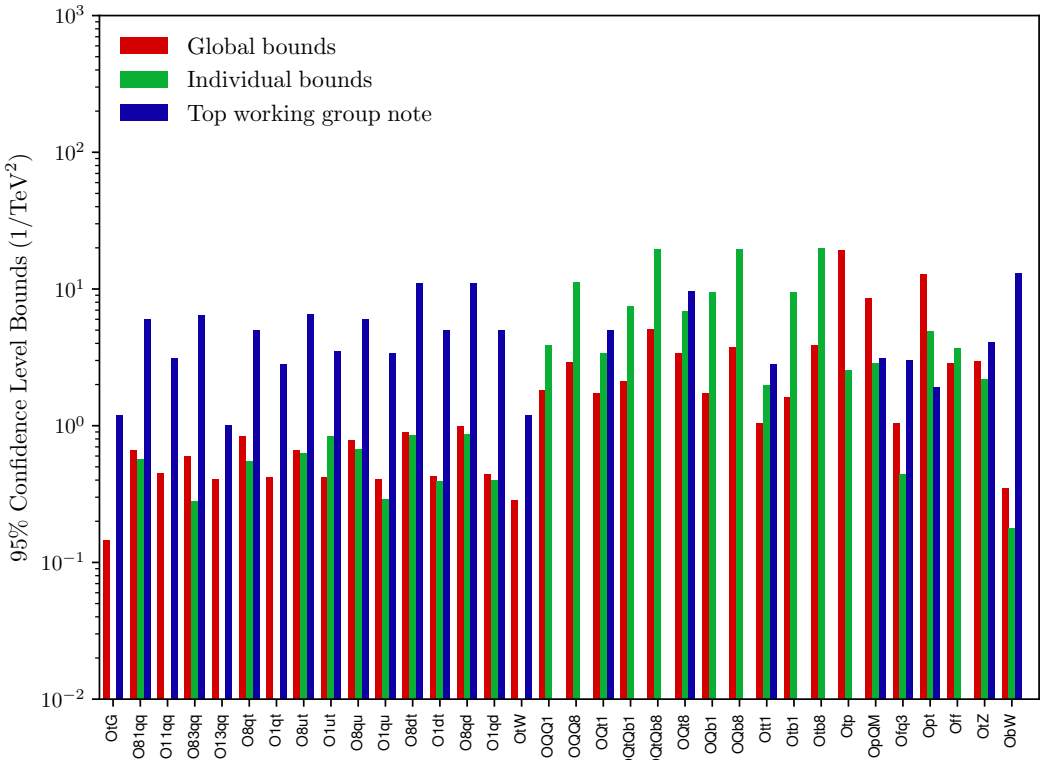

Figure 5.4: Graphical representation of the results of Tables 5.7and 5.8, where we compare the 95% CL bounds on the 34 degrees of freedom included the present analysis, both in the marginalised (global) and in the individual fit cases, with the bounds reported in the LHC Top WG EFT note [54].

Another useful way to present our results is by representing the bounds on $\Lambda/\sqrt{|c_i|}$ that are derived from the fit. This is interesting because, assuming UV

completions where the values of the fitted degrees of freedom c_i are $\mathcal{O}(1)$, plotting the results this way indicates the approximate reach in energy that is being achieved by the SMEFT global analysis. This comparison is shown in Fig. 5.5, now only for the marginalised bounds from the global fit. We find that for the degrees of freedom that are better constrained we achieve sensitivity up to scales as high as $\Lambda \simeq 3$ TeV, in particular thanks to the chromomagnetic operator `OtG` which is well determined from the differential measurements of top quark pair production. Future measurements based on larger statistics should allow us to probe even higher scales, in particular by means of the high-luminosity LHC datasets.

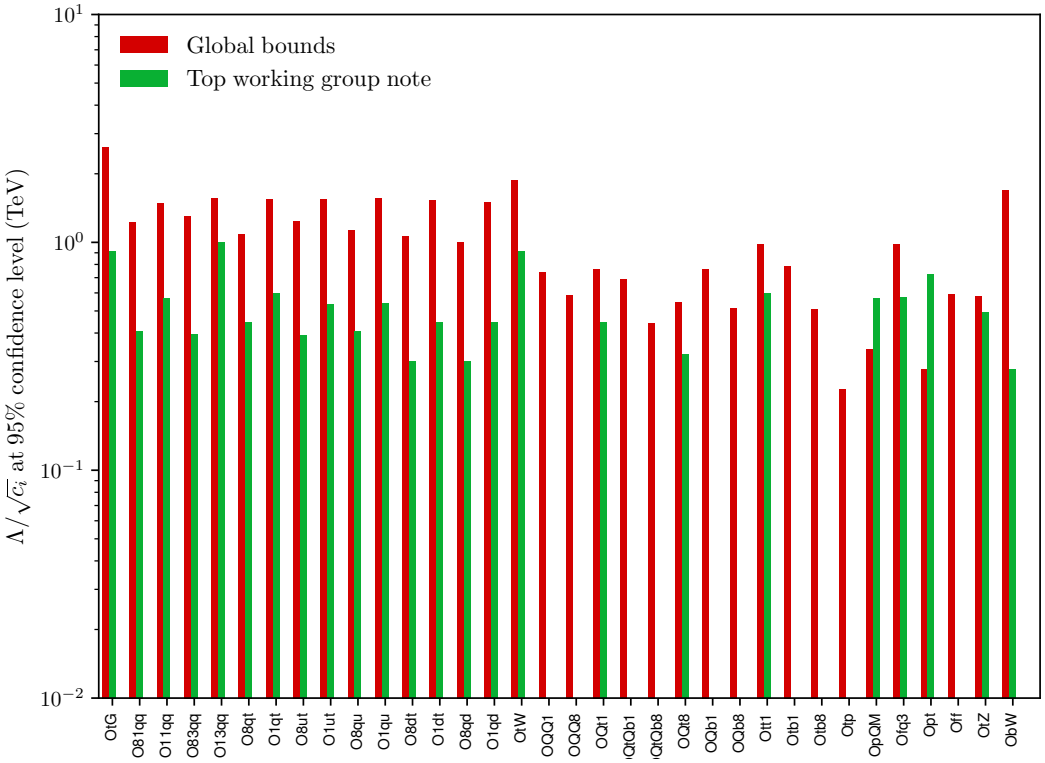

Figure 5.5: Same as Fig. 5.4, now representing the marginalised bounds obtained from the global fit as bounds on $\Lambda/\sqrt{|c_i|}$.

5.3.3 Theoretical variations

In this subsection, we will aim to assess the robustness and stability of our results by comparing the baseline fit results with those of fits based on two alternative

theory settings. Firstly we compare with a fit where only LO QCD effects are included for the SMEFT contributions, and then with a fit that includes only the linear $\mathcal{O}\left(\Lambda^{-2}\right)$ terms in the effective theory expansion (but still based on NLO QCD for the SMEFT contributions). In Table 5.9 we show the 95% CL bounds on the fitted degrees of freedom obtained in the global analysis, and compare the results obtained using the baseline theory settings with those of the theoretical variations. The corresponding individual comparison has already been presented in Table 5.8.

As can be seen from Table 5.8, the individual bounds that one obtains at $\mathcal{O}\left(\Lambda^{-2}\right)$ are very loose for all of the four-heavy quark operators. This indicates that, using only the linear SMEFT contribution, one has very limited sensitivity to these degrees of freedom. We see that in Table 5.9, the marginalised bounds for these operators is loose, but much tighter than in the individual case. This is caused by the same reason discussed in Sec. 5.3.2; the operators are, in effect, incorrectly constrained at the global level, as at most two datapoints constrain them.

This allows for a huge amount of fluctuation and numerical instability in the fitting code, which enables the global fit to find an artificially tight bound for these operators. We therefore stress again that, while we have shown the results (and not attempted to sweep them under the carpet), they should be taken as an estimate until more data can be added to the analysis. The individual bounds, however, are robust, as they are computed for all degrees of freedom by simply computing the χ^2 profile, finding its minimum and finding the 95% confidence level interval.

SMEFiT global analysis (marginalised)

Notation	DoF	Baseline	$\mathcal{O}(\Lambda^{-2})$ only	LO QCD
OQQ1	c_{QQ}^{1}	$[-1.5, 1.9]$	$[-8.8, 9.9]$	$[-1.3, 2.4]$
OQQ8	c_{QQ}^{8}	$[-4.1, 2.0]$	$[-24.8, 22.7]$	$[-3.9, 1.3]$
OQt1	c_{Qt}^{1}	$[-1.9, 1.7]$	$[-3.8, 3.3]$	$[-2.2, 2.1]$
OQt8	c_{Qt}^{8}	$[-3.7, 2.4]$	$[-7.9, 7.7]$	$[-4.5, 3.5]$
OQb1	c_{Qb}^{1}	$[-1.7, 1.3]$	$[-14.5, 13.3]$	$[-1.8, 1.5]$
OQb8	c_{Qb}^{8}	$[-4.5, 3.1]$	$[-30.0, 28.0]$	$[-3.9, 1.5]$
Ott1	c_{tt}^{1}	$[-1.0, 1.0]$	$[-2.5, 2.9]$	$[-1.4, 1.2]$
Otb1	c_{tb}^{1}	$[-1.8, 1.3]$	$[-13.8, 12.9]$	$[-1.2, 1.6]$
Otb8	c_{tb}^{8}	$[-4.7, 2.5]$	$[-29.9, 27.6]$	$[-4.1, 1.8]$
OQtQb1	c_{QtQb}^{1}	$[-3.1, 2.0]$	$*$	$[-2.0, 1.9]$
OQtQb8	c_{QtQb}^{8}	$[-4.7, 5.1]$	$*$	$[-4.0, 3.5]$
O81qq	$c_{Qq}^{1,8}$	$[-1.1, 0.2]$	$[-1.5, 1.0]$	$[-0.9, 0.1]$
O11qq	$c_{Qq}^{1,1}$	$[-0.4, 0.5]$	$[-1.0, 1.0]$	$[-0.2, 0.3]$
O83qq	$c_{Qq}^{3,8}$	$[-0.6, 0.6]$	$[-1.0, 1.0]$	$[-1.1, 0.9]$
O13qq	$c_{Qq}^{3,1}$	$[-0.5, 0.3]$	$[-0.4, 0.5]$	$[-0.4, 0.3]$
O8qt	c_{tq}^{8}	$[-0.8, 0.9]$	$[-1.3, 2.0]$	$[-0.8, 0.1]$
O1qt	c_{tq}^{1}	$[-0.4, 0.4]$	$[-1.0, 1.0]$	$[-0.3, 0.3]$
O8ut	c_{tu}^{8}	$[-1.1, 0.2]$	$[-2.0, 2.0]$	$[-0.9, -0.1]$
O1ut	c_{tu}^{1}	$[-1.2, -0.3]$	$[-0.9, 0.3]$	$[-0.2, 0.3]$
O8qu	c_{Qu}^{8}	$[-0.7, 0.8]$	$[-2.0, 2.0]$	$[-0.9, -0.1]$
O1qu	c_{Qu}^{1}	$[-0.2, 0.6]$	$[-1.0, 0.9]$	$[-0.2, 0.2]$
O8dt	c_{td}^{8}	$[-1.4, 0.4]$	$[-3.0, 1.9]$	$[-1.0, 0.0]$
O1dt	c_{td}^{1}	$[-0.4, 0.4]$	$[-1.0, 0.7]$	$[-0.3, 0.2]$
O8qd	c_{Qd}^{8}	$[-1.2, 0.8]$	$[-3.0, 2.9]$	$[-0.9, 0.1]$
O1qd	c_{Qd}^{1}	$[-0.4, 0.5]$	$[-1.0, 0.7]$	$[-0.2, 0.4]$
OtG	c_{tG}	$[-0.1, 0.1]$	$[-0.2, 0.1]$	$[-0.2, 0.2]$
OtW	c_{tW}	$[-0.3, 0.2]$	$[-0.4, 0.2]$	$[-0.4, 0.2]$
ObW	c_{bW}	$[-0.3, 0.3]$	$*$	$[-0.3, 0.3]$
OtZ	c_{tZ}	$[-2.7, 3.2]$	$[-4.0, 3.1]$	$[-3.1, 3.3]$
Off	$c_{\varphi tb}$	$[-2.6, 3.1]$	$*$	$[-2.5, 2.9]$
Ofq3	$c_{\varphi Q}^{3}$	$[-1.6, 0.5]$	$[-1.1, 1.0]$	$[-1.4, 0.4]$
OpQM	$c_{\varphi Q}^{-}$	$[-1.7, 14.5]$	$[-6.9, 10.5]$	$[-3.5, 17.6]$
Opt	$c_{\varphi t}$	$[-19.1, 7.4]$	$[-17.1, 10.0]$	$[-20.3, 10.1]$
Otp	$c_{t\varphi}$	$[-4.4, 33.8]$	$[-7.4, 5.9]$	$[-6.1, 33.4]$

Table 5.9: Same as Table 5.8, now for marginalised fits.

In Fig. 5.6 we show the graphical representation of the bounds reported in Table 5.9 for the global fit results with different theory settings. Note that, for the $\mathcal{O}\left(\Lambda^{-2}\right)$ fit, several degrees of freedom are absent as indicated in Table 5.5.

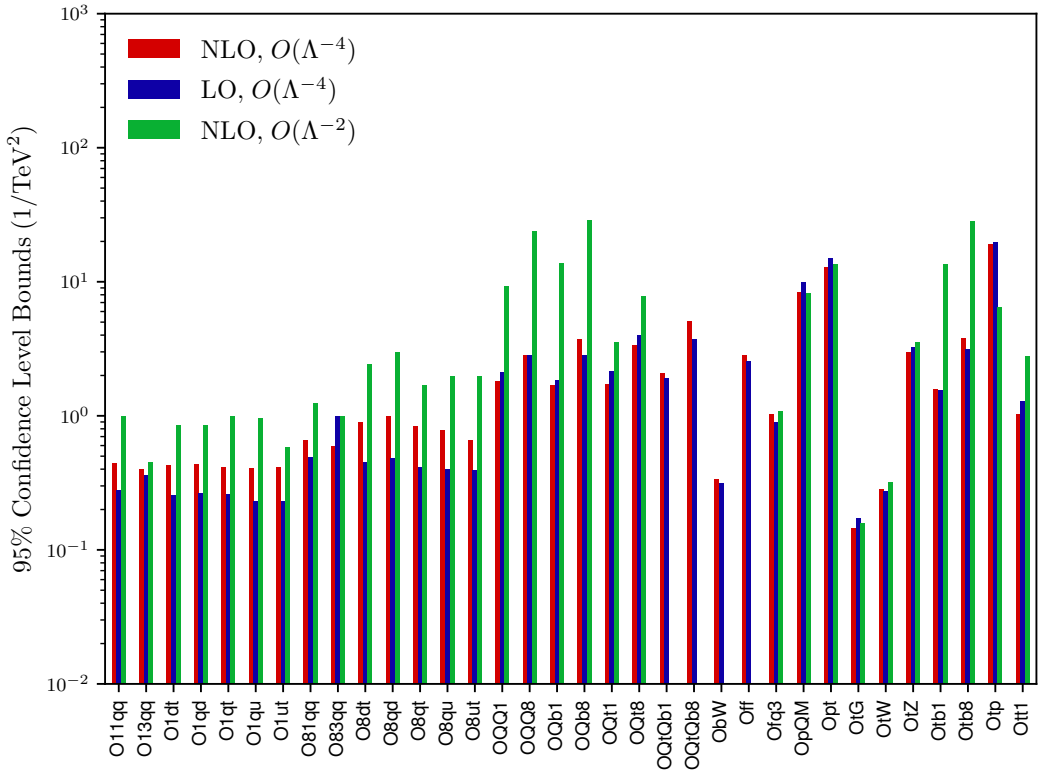

Figure 5.6: Same as Fig. 5.4, now comparing the baseline fit results reported in Table 5.7 with those from Table 5.9 based on the corresponding fits where (i) only LO QCD effects are included in the SMEFT contributions and (ii) only the linear $\mathcal{O}\left(\Lambda^{-2}\right)$ terms are accounted for.

From these comparisons, one finds that the impact of the NLO QCD corrections varies depending on the specific operators considered. For the two-light-two-heavy quark operators, the bounds including the NLO corrections are on the whole worsened compared to the bounds derived with only the leading order calculation. For example, the bound on the coefficient of the `O11qq` operator worsens to $[-0.4, 0.5]$, with baseline theory settings, from $[-0.2, 0.3]$, with LO QCD theory in the SMEFT contribution. Note, however, that this improvement does not necessarily mean that the NLO QCD corrections associated to the contributions

of `O11qq` itself are important. At the level of single-operator fits, the bounds at NLO and LO are the same within the precision we quote.

That being said, it is interesting that the bounds in general worsen for the two-heavy-two-light quark degrees of freedom upon the inclusion of NLO corrections, meaning that at the global fit level, they systematically increase. We show in Table 5.10 the comparison of the $\chi^2/n_{\rm dat}$ values of the fit obtained with the baseline theory settings (NLO QCD and $\mathcal{O}\left(\Lambda^{-4}\right)$ corrections) with the corresponding values obtained in the fits where either only LO QCD effects or $\mathcal{O}\left(\Lambda^{-2}\right)$ corrections are included in the SMEFT corrections. At LO, several of the two-heavy-two-light quark degrees of freedom (including `O11qq`) are much less constrained as they only enter at $\mathcal{O}\left(\Lambda^{-2}\right)$ at NLO for $t\bar{t}$ production. We can see in Table 5.10 that the LO fit, by removing the strong constraints upon many of the degrees of freedom from $t\bar{t}$ production, enables us to very well describe the $t\bar{t}b\bar{b}$, which is not seen by any other of the fits. This seems to suggest that the tighter bounds found by the LO fit is at least partially explained by some tension in the $t\bar{t}b\bar{b}$ datapoint being alleviated by the degrees of freedom which are allowed to fluctuate widely when not strongly constrained by the many $t\bar{t}$ data points.

Elsewhere in the parameter space, the NLO corrections have very little impact. This is as expected, as the NLO corrections only affect the number of operators fitted in the two-heavy-two-light quark sector, as shown in Table 5.5. We can therefore conclude that the impact of the NLO corrections is minimal when new degrees of freedom are not introduced, but have a large impact when data points become very constraining upon the inclusion of the NLO corrections.

Similar considerations apply to those operators whose bounds in the global fit worsen when the NLO QCD corrections to the SMEFT contributions are missing. For these three operators, namely `Otp`, `Ofq3`, and `Off`, one finds that including or not NLO QCD effects has essentially no impact. Therefore, the observed effect is most likely a consequence of the fact that adding NLO QCD corrections rearranges

the weight of the different degrees of freedom in the global fit, leading to an overall modification of the fit results.

Concerning the impact of the quadratic $\mathcal{O}\left(\Lambda^{-4}\right)$ terms, from the comparisons in Fig. 5.6, we find that the higher order corrections have a substantial affect on many of the degrees of freedom. In those cases, apart from `Otp`, the $\mathcal{O}\left(\Lambda^{-4}\right)$ terms improve the bounds by up to over an order of magnitude, in the case of the four-heavy quark sector. The improvement on `Otp` when excluding the $\mathcal{O}\left(\Lambda^{-4}\right)$ terms was discussed in Sec. 4.3.2; for this degree of freedom, the quadratic and linear terms have opposite signs and therefore cancel out.

Dataset	$\chi^2/n_{\rm dat}$			$n_{\rm dat}$
	Baseline	$\mathcal{O}\left(\Lambda^{-2}\right)$ only	LO QCD	
ATLAS_tt_8TeV_ljets [$m_{t\bar{t}}$]	1.45	1.22	1.68	7
CMS_tt_8TeV_ljets [$y_{t\bar{t}}$]	1.02	1.15	0.82	10
CMS_tt2D_8TeV_dilep [$(m_{t\bar{t}}, y_t)$]	1.38	1.38	1.38	16
CMS_tt_13TeV_ljets2 [$m_{t\bar{t}}$]	1.24	1.49	1.14	8
CMS_tt_13TeV_dilep [$m_{t\bar{t}}$]	1.40	1.91	0.81	6
CMS_tt_13TeV_ljets_2016 [$m_{t\bar{t}}$]	0.93	1.33	0.57	10
ATLAS_WhelF_8TeV	1.43	1.42	1.97	3
CMS_WhelF_8TeV	0.55	0.56	1.43	3
CMS_ttbb_13TeV	4.84	4.30	1.14	1
CMS_tttt_13TeV	0.03	0.00	0.00	1
ATLAS_tth_13TeV	1.60	0.02	0.14	1
CMS_tth_13TeV	0.89	0.73	0.31	1
ATLAS_ttZ_8TeV	0.23	2.03	0.85	1
ATLAS_ttZ_13TeV	1.24	0.73	0.19	1
CMS_ttZ_8TeV	2.65	0.31	0.16	1
CMS_ttZ_13TeV	1.69	0.38	0.06	1
ATLAS_ttW_8TeV	1.87	0.40	0.12	1
ATLAS_ttW_13TeV	0.95	0.51	0.54	1
CMS_ttW_8TeV	1.99	0.68	0.35	1
CMS_ttW_13TeV	0.20	0.50	0.39	1
CMS_t_tch_8TeV_dif	0.37	0.25	0.24	6
ATLAS_t_tch_8TeV [y_t]	0.40	0.51	0.57	4
ATLAS_t_tch_8TeV [$y_{\bar{t}}$]	0.33	0.35	0.34	4
ATLAS_t_sch_8TeV	0.03	0.46	1.77	1
ATLAS_t_tch_13TeV	0.06	0.04	0.03	2
CMS_t_tch_13TeV_dif [y_t]	0.51	0.49	0.47	4
CMS_t_sch_8TeV	1.50	1.07	0.78	1
ATLAS_tW_inc_8TeV	0.01	0.03	0.14	1
CMS_tW_inc_8TeV	0.03	0.00	0.12	1
ATLAS_tW_inc_13TeV	0.69	0.49	0.91	1
CMS_tW_inc_13TeV	2.63	2.74	1.23	1
ATLAS_tZ_inc_13TeV	0.03	0.00	0.00	1
CMS_tZ_inc_13TeV	0.63	0.61	0.07	1
Total	**1.04**	**1.05**	**0.84**	**103**

Table 5.10: Same as Table 5.6, now comparing the $\chi^2/n_{\rm dat}$ values of the fit obtained with the different theory settings.

As already mentioned several times, within a global fit it is in general not possible to precisely pinpoint how a variation of the theory settings translates into a difference in the resulting constraints on the fitted degrees of freedom, with obvious exceptions such as for those operators whose contributions vanish at $\mathcal{O}\left(\Lambda^{-2}\right)$. For such an assessment, the results of the single-operator fits reported in Table 5.8 are more suitable. For example, from the results obtained in the single-operator fits we can confirm that the improvement in the bounds obtained for, for example the `O8dt` and `OtZ` degrees of freedom upon the inclusion of the quadratic $\mathcal{O}\left(\Lambda^{-4}\right)$ corrections is genuine, rather than an artefact of the global fit.

To conclude this assessment of the impact of the NLO QCD and $\mathcal{O}\left(\Lambda^{-4}\right)$ corrections on the fit results, we want to understand how the data-theory agreement changes with the different theoretical settings by comparing the $\chi^2/n_{\rm dat}$ values in Table 5.10. The corresponding comparison with the prior (SM) theory calculations was reported in Table 5.6.

One finds that, for all three theory settings, the total $\chi^2/n_{\rm dat}$ is similar ($\simeq 1$). The lowest value is found when using LO QCD theory for the SMEFT corrections. In that case, we find $\chi^2/n_{\rm dat} = 0.84$, with the data on $t\bar{t}$ differential distributions and $t\bar{t}b\bar{b}$ data point driving the improvement as compared to the baseline settings. It will be interesting to revisit this comparison once more precise top production measurements become available and assess whether or not there is evidence for the need of NLO QCD corrections to achieve the optimal description of the experimental data.

We mentioned in Sec. 5.3.1 that the $t\bar{t}Z$ datasets seem on the whole to be poorly described upon the addition of the SMEFT corrections. From Table 5.10 we see that the datasets are very well described by the theoretical variations used; we discussed that at 8 TeV there is some tension between the ATLAS and CMS results but found that at 13 TeV the SM was a better description of the data than the SMEFT.

We see that, while the χ^2 including SMEFT variations are still worse than the SM, the results are significantly better, in particular for the LO fit. In Sec. 5.2.1 it was mentioned that the full NLO calculations for $t\bar{t}Z$ are not calculated, instead the K-factors from [64] are used. This analysis indicates that the K-factors might be insufficient, and the full NLO calculation needed. Of course it is possible that the NLO SMEFT contribution might truly lead to a worsening of the data-theory agreement for $t\bar{t}Z$, but we cannot be sure until we rule out methodological explanations.

5.3.4 Dataset dependence

Within the SMEFiT framework it is straightforward to repeat the analysis with arbitrary variations of the input dataset. To investigate the dependence of our results with respect to this choice of input dataset, in Fig. 5.7 we show a similar comparison as that of Fig. 5.4, now assessing how the baseline fit results vary if a different input dataset is used. In the first case, instead of the $m_{t\bar{t}}$ distributions indicated in Table 5.6, we use the corresponding $y_{t\bar{t}}$ distributions for the inclusive $t\bar{t}$ production measurements. In the second case, the fit is performed only using inclusive $t\bar{t}$ production measurements as input, and excluding all other processes. Note that in the latter case the fit has sensitivity to only a subset of 15 degrees of freedom.

The rationale behind performing a fit replacing the $m_{t\bar{t}}$ distributions in inclusive top quark pair production with the corresponding $y_{t\bar{t}}$ ones is to gauge the sensitivity of our results to the high-energy region, since the $m_{t\bar{t}}$ distribution is the one more directly sensitive to it due to the bins of $m_{t\bar{t}}$ at up to 2.5 TeV [127]. Although high-energy measurements enhance the sensitivity to SMEFT effects, one should avoid being dominated by the highest energy bins since this could jeopardise the effective theory interpretation, as we are assuming our cut-off, Λ is in the TeV region. Therefore, we would ideally like to see that the bounds do not become

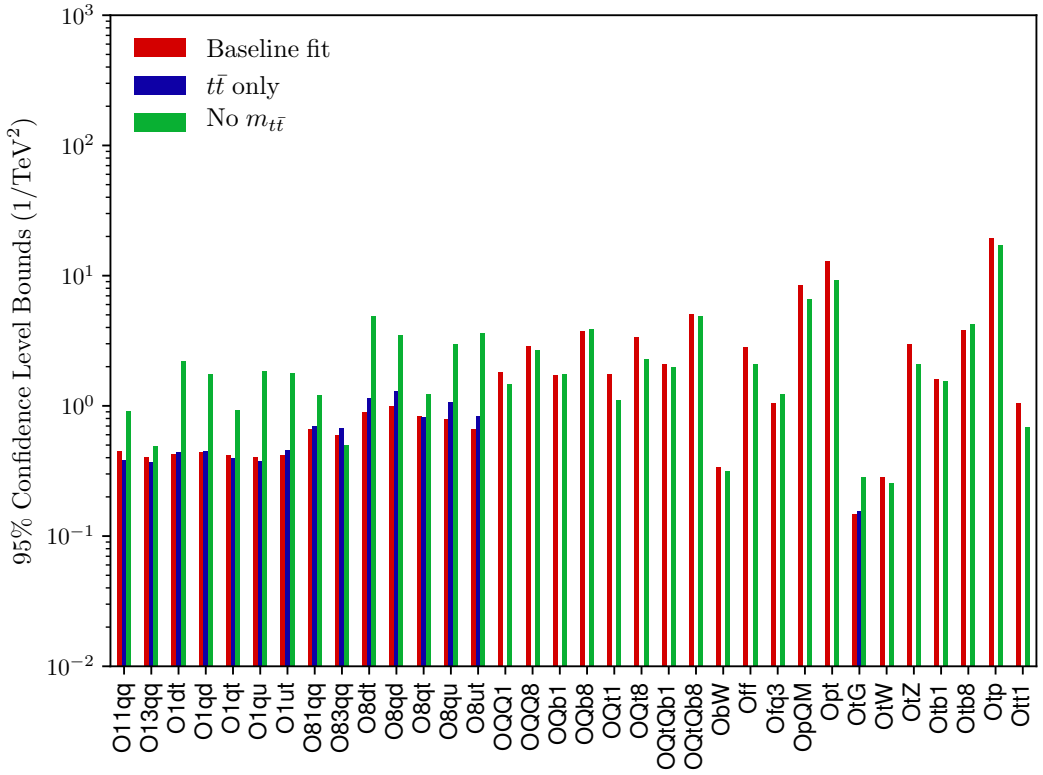

Figure 5.7: Same as Fig. 5.4, now comparing the fit results based on the baseline dataset with those obtained from two different datasets.

markedly worse once the $m_{t\bar{t}}$ distributions are replaced by the $y_{t\bar{t}}$ ones, since that would otherwise indicate that fit results are determined by high-energy events.

Concerning the fit based only on inclusive $t\bar{t}$ measurements, we would like to find that the bounds obtained from a SMEFT fit to a partial dataset are comparable to or looser than those from the baseline global dataset. Note that this is a non-trivial consistency check of the whole methodology; when additional experimental constraints are included in the analysis, then the bounds on the fitted coefficients must by necessity be either smaller or unchanged up to finite-size effects. If this were not the case, it would imply that fit results are driven not by the experimental data but by biased methodological choices.

From the comparison in Fig. 5.7, we observe that the bounds for some of the two-light-two-heavy degrees of freedom such as `O8dt` and `O8qu` worsen, presumably

as a consequence of the missing constraints provided by other processes, such as $t\bar{t}$ production in association with Z bosons or H bosons. For all the degrees of freedom directly constrained by the inclusive $t\bar{t}$ measurements, the bounds found in the global fit are comparable or superior to those obtained in the $t\bar{t}$-only fit. As always, there is some fluctuation due to the finite-size uncertainty expected in the fit as we only have a finite set of replicas; $N_{\rm rep} = 1000$. Therefore a fluctuation of the order $1/\sqrt{N_{\rm rep}}$ (i.e. approximately 3%) is to be expected.

The other comparison shown in Fig. 5.7 is that between the fit with the baseline dataset and with the same dataset where we have replaced the $m_{t\bar{t}}$ distributions with the corresponding $y_{t\bar{t}}$ ones. In this case, we find that for a subset of the degrees of freedom, in particular those constrained by inclusive $t\bar{t}$ data, we find that more stringent bounds are obtained in the fits based on the $m_{t\bar{t}}$, rather than the $y_{t\bar{t}}$, distributions. This means that we are indeed sensitive to the high-energy region, and further study is required to assess the impact of these high-energy bins. In particular, whilst the high-energy bins are clearly advantageous to getting tighter bounds, we need to ensure that the interpretation of the EFT description is still valid. As expected, the other degrees of freedom are largely unaltered by the change in dataset, as they are not constrained by the inclusive $t\bar{t}$ data.

5.4 The top-philic scenario

Throughout this chapter, we have used the assumptions we outlined in Sec. 2.2.2. That is, we enforce some additional symmetries in order to reduce the number of degrees of freedom which enter into the fit. Whilst this is a reasonable baseline, there is no reason, per se, why we cannot impose other constraints onto the degrees of freedom. In particular, we can look at the top-philic scenario, which assumes that new physics couples to only the top quark and bosons; i.e. only bosons, the right-handed top singlet t, and the left-handed 3rd generation doublet, Q. In this process, the CKM matrix is again approximated by an identity matrix and all

Yukawa couplings but the top and bottom ones are neglected. This is motivated by the fact that, given that the new physics is assumed to be at a high scale Λ, we only allow it to couple to the heaviest states in the SM.

Class	Notation	Degree of Freedom
$QQQQ$	`OQQ1`	c_{QQ}^{1}
	`OQQ8`	c_{QQ}^{8}
	`OQt1`	c_{Qt}^{1}
	`OQt8`	c_{Qt}^{8}
	`Ott1`	c_{tt}^{1}
$QQqq$	`O81qq`	$c_{Qq}^{1,8} = c_{Qu}^{8} = c_{Qd}^{8} = c_{Qb}^{8}$
	`O11qq`	$c_{Qq}^{1,1} = \frac{1}{4}c_{Qu}^{1} = -\frac{1}{2}c_{Qd}^{1} = -\frac{1}{2}c_{Qb}^{1}$
	`O13qq`	$c_{Qq}^{3,1}$
	`O8qt`	$c_{tq}^{8} = c_{td}^{8} = c_{tb}^{8} = c_{tu}^{8}$
	`O1qt`	$c_{tq}^{1} = \frac{1}{4}(C_{uu}^{(ii33)} + \frac{1}{3}C_{uu}^{(i33i)}) = -\frac{1}{2}c_{td}^{1} = -\frac{1}{2}c_{tb}^{1}$
$QQ + V, G, \varphi$	`OtG`	c_{tG}
	`OtW`	c_{tW}
	`ObW`	c_{bW}
	`OtZ`	c_{tZ}
	`Off`	$c_{\varphi tb}$
	`Ofq3`	$c_{\varphi Q}^{3}$
	`OpQM`	$c_{\varphi Q}^{-}$
	`Opt`	$c_{\varphi t}$
	`Otp`	$c_{t\varphi}$

Table 5.11: The degrees of freedom which enter into the top-philic scenario.

By imposing the top-philic scenario onto the SMEFT, we are left with only 19 degrees of freedom, shown in Table 5.11. The computation of the allowed degrees of freedom is non-trivial, as the basis of operators is over-complete and has to be transformed and projected down onto the Warsaw basis. A more detailed discussion of the top-philic scenario can be found in [54].

We show in Fig. 5.8 the 95% confidence level intervals for the baseline fit in

the top-philic scenario. We see that most of the bounds for the degrees of freedom which are unchanged by the additional constraints such as `OtG` and `O13qq` are very similar in the two fits, as we would expect. Furthermore, the bounds are as good, within the finite-size effects, or tighter for all degrees of freedom which are constrained by other ones in the fit.

It is interesting to see that in the top-philic case some degrees of freedom which are not affected by the requirements of the model are much more tightly bound than in the baseline. In particular, those in the four-heavy quark sector and some in the top+boson sector show a remarkable improvement. The reason for this is the parameter space in the top-philic scenario is now much smaller, due to the correlations induced between the degrees of freedom. Therefore the fit is now able to allow some degrees of freedom to greatly improve their bounds, especially for those only constrained by a few data points, which are precisely the ones in the aforementioned sectors. There is a caveat, however; as discussed in Sec. 5.3.2 that the baseline bounds reported for the four-heavy quark sector were unreliable due to the fact we are trying to constrain many degrees of freedom with a couple of data points.

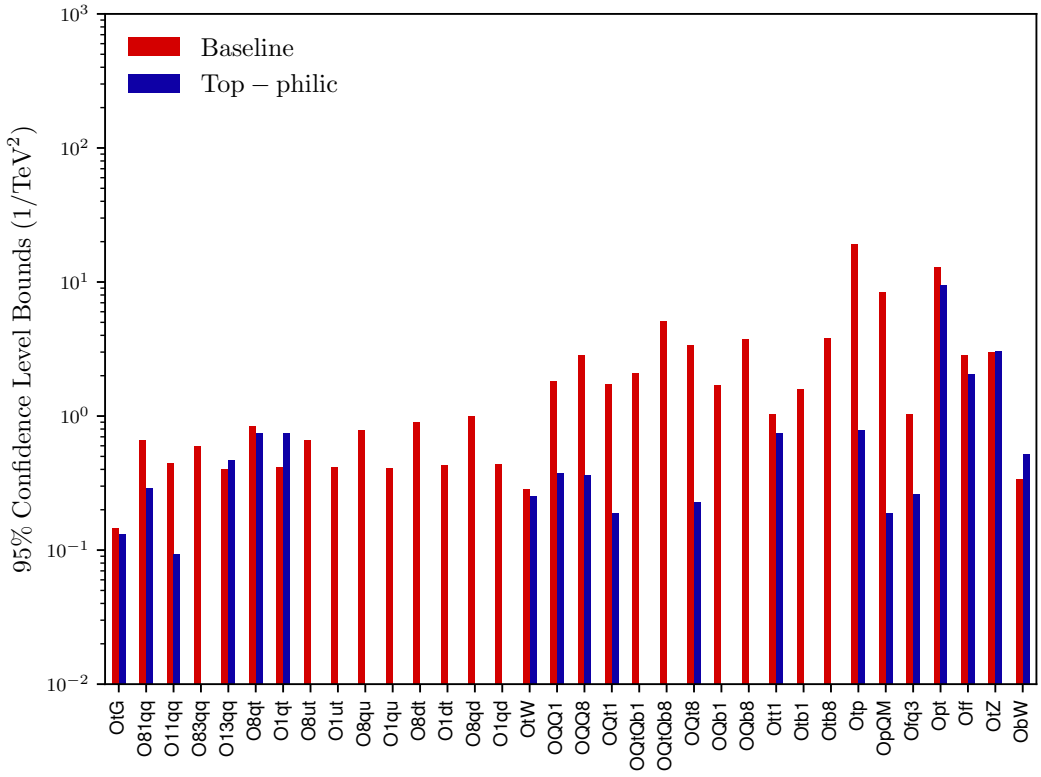

Figure 5.8: The 95% confidence level intervals for the baseline and top-philic scenarios.

CHAPTER 6

Outlook and conclusions

In this thesis we have discussed two frameworks which enable us to make more accurate theoretical predictions of free parameters at the LHC. We aimed to make robust predictions within two distinct theories; in the first part of the work, we introduced the NNPDF approach to fitting the strong coupling constant, α_s, which is a required input to all QCD calculations performed for LHC physics. We then moved on to discuss SMEFiT, a novel fitting framework designed to constrain Wilson coefficients in the SMEFT. We applied SMEFiT to the top sector at dimension-6; as the top quark is the heaviest known fundamental particle, it holds a special place as a possible area to look for new physics beyond the SM.

The correlated replica method described in Chapter 3 allowed us, for the first time, to propagate PDF uncertainties fully onto the determination of $\alpha_s(M_Z)$. In comparison to previous determinations by NNPDF, the fit we present includes for the first time a large amount of LHC data, using NNLO theory in all cases. We also thoroughly investigated the main sources of methodological uncertainties caused by the fitting framework. We found that the determination of $\alpha_s(M_Z)$ is considerably stabilised by the use of a wide set of different processes and data, and

we showed that a global simultaneous determination of $\alpha_s(M_Z)$ and PDFs leads to a more stable and accurate result than the one obtained from subsets of data. We thus obtain a value of $\alpha_s(M_Z)$ which is likely to be more reliable with regards to the fitting methodology than previous results based on similar techniques.

The main limitation of our result comes from the lack of a reliable method to estimate theoretical uncertainties including ones related to missing higher order perturbative corrections. We briefly discussed the simple way in which we estimate an upper bound on the size of the missing higher order uncertainties; however much progress in this direction is needed. We do not aim to determine any other source of theoretical uncertainty; with the very small experimental uncertainty we have found in this work, it is necessary to gain a handle on the size of the various theoretical contributions. For the time being, even with a very conservative estimate of the theoretical uncertainty, our result provides a very accurate determination of $\alpha_s(M_Z)$, and thus provides valuable input for precision tests of the Standard Model and for searches for new physics beyond it.

In Chapter 4 we introduced SMEFiT, a novel approach to carrying out fits within the SMEFT. SMEFiT is a highly flexible fitting framework, with no constraints on the dimensionality of the parameter space it is able to constrain other than computational power. Its main ingredient is the Monte Carlo replica method, cross-checked both using the closure test methodology, and against a distinct Monte Carlo fitting procedure called Nested Sampling.

As a proof-of-concept of the SMEFiT framework, in Chapter 5 we have presented an analysis of top quark production measurements at the LHC 8 TeV and 13 TeV. We have included a wide range of top quark data, in terms of total rates and differential distributions. The theoretical SM and SMEFT cross sections have been evaluated including NLO QCD corrections by default; in the SM case, we have also considered NNLO effects for the differential distributions in $t\bar{t}$ and single top t-channel production. We have also explored theoretical variations upon our baseline result, including determining the impact of the $\mathcal{O}(\Lambda^{-4})$ and NLO

QCD corrections on our bounds, as well as briefly exploring the more restrictive, but physically well motivated top-philic scenario.

There are several areas in which this work can be extended. Firstly, we do not yet have a quantitive estimate on the size of the missing higher order uncertainties in our analysis or other methodological uncertainties. Not only does our framework not account for the theoretical uncertainties due to the truncation of the perturbative series in the SM and SMEFT, but we also do not quantify the finite-size uncertainties, both due to limited replicas, but also due to the (at times, large) Monte Carlo integration errors in the calculation of the SMEFT contributions.

Finite-size uncertainties are quantified in Chapter 3 using the bootstrapping technique, which is certainly applicable to SMEFiT as we again are using a replica approach. The interplay between PDFs and the SMEFT is also important to consider; it is important to extend the framework so that we can keep track of the PDF induced correlations between datasets. It is therefore natural to try to perform simultaneous PDF + SMEFT fits within the NNPDF framework, so that, not only can we keep track of correlations between the two, but the optimal PDF fit can be produced for the SMEFT fit to the Wilson coefficients. Finally, a natural extension of the SMEFiT approach is to try and constrain a larger parameter space. Initial work on simultaneously fitting the top+Higgs sector has proven promising, with the framework comfortably managing to constrain the $\sim$60 degrees of freedom which enter.

Experimental uncertainties at the LHC are now reducing to a few percent, and with the high-luminosity upgrade of the LHC, we expect unprecedented statistics which will improve experimental precision even further. The challenge is therefore to improve theoretical predictions accordingly. This is a truly monumental task, which will involve higher-order calculations in QCD, electroweak theory, and refining our understanding of PDFs, parton showers, non-perturbative corrections, as well as the theoretical knowledge of any BSM theories we wish to constrain.

In this thesis we have discussed just two aspects of this; it is clear there is still a long way to go in our quest to achieve the ultimate precision at the LHC and future colliders.

References

[1] **NNPDF** Collaboration, R. D. Ball, S. Carrazza, L. Del Debbio, S. Forte, Z. Kassabov, J. Rojo, E. Slade, and M. Ubiali, *Precision determination of the strong coupling constant within a global PDF analysis*, *Eur. Phys. J.* **C78** (2018), no. 5 408, [arXiv:1802.03398].

[2] N. P. Hartland, F. Maltoni, E. R. Nocera, J. Rojo, E. Slade, E. Vryonidou, and C. Zhang, *A Monte Carlo global analysis of the Standard Model Effective Field Theory: the top quark sector*, *JHEP* **04** (2019) 100, [arXiv:1901.05965].

[3] J. J. Ethier, F. Maltoni, L. Mantani, E. R. Nocera, J. Rojo, E. Slade, E. Vryonidou, and C. Zhang, "A combined EFT interpretation of Higgs and top quark measurements from the LHC." in preparation.

[4] **ATLAS** Collaboration, G. Aad et al., *Observation of a new particle in the search for the Standard Model Higgs boson with the ATLAS detector at the LHC*, *Phys.Lett.* **B716** (2012) 1–29, [arXiv:1207.7214].

[5] **CMS** Collaboration, S. Chatrchyan et al., *Observation of a New Boson at a Mass of 125 GeV with the CMS Experiment at the LHC*, *Phys. Lett.* **B716** (2012) 30–61, [arXiv:1207.7235].

[6] P. Minkowski, $\mu \to e\gamma$ *at a rate of one out of 109 muon decays?*, *Physics Letters B* **67** (1977), no. 4 421 – 428.

[7] M. Gell-Mann, P. Ramond, and R. Slansky, *Complex Spinors and Unified Theories*, *Conf. Proc.* **C790927** (1979) 315–321, [arXiv:1306.4669].

[8] R. N. Mohapatra and G. Senjanović, *Neutrino mass and spontaneous parity nonconservation*, *Phys. Rev. Lett.* **44** (Apr, 1980) 912–915.

[9] S. Weinberg, *Baryon and Lepton Nonconserving Processes*, *Phys. Rev. Lett.* **43** (1979) 1566–1570.

[10] **ATLAS** Collaboration, A. collaboration, *Search for Minimal Supersymmetric Standard Model Higgs Bosons H/A in the $\tau\tau$ final state in up to 13.3 fb^{-1} of pp collisions at $\sqrt{s}$= 13 TeV with the ATLAS Detector*, .

[11] **CMS** Collaboration, C. Collaboration, *Search for a neutral MSSM Higgs boson decaying into $\tau\tau$ with 12.9 fb^{-1} of data at $\sqrt{s} = 13$ TeV*, .

[12] **ATLAS** Collaboration, T. A. collaboration, *Search for supersymmetry in events with four or more leptons in $\sqrt{s} = 13$ TeV pp collisions using 13.3 fb^{-1} of ATLAS data*, .

[13] **CMS** Collaboration, C. Collaboration, *Searches for non-resonant new phenomena in final states with leptons and photons at CMS*, .

[14] H.-W. Lin et al., *Parton distributions and lattice QCD calculations: a community white paper*, *Prog. Part. Nucl. Phys.* **100** (2018) 107–160, [arXiv:1711.07916].

[15] **NNPDF** Collaboration, R. D. Ball et al., *Parton distributions from high-precision collider data*, *Eur. Phys. J.* **C77** (2017), no. 10 663, [arXiv:1706.00428].

[16] P. A. Baikov, K. G. Chetyrkin, and J. H. Kühn, *Five-Loop Running of the QCD coupling constant*, *Phys. Rev. Lett.* **118** (2017), no. 8 082002, [arXiv:1606.08659].

[17] T. Luthe, A. Maier, P. Marquard, and Y. Schröder, *Towards the five-loop Beta function for a general gauge group*, *JHEP* **07** (2016) 127, [arXiv:1606.08662].

[18] T. Luthe, A. Maier, P. Marquard, and Y. Schroder, *The five-loop Beta function for a general gauge group and anomalous dimensions beyond Feynman gauge*, *JHEP* **10** (2017) 166, [arXiv:1709.07718].

[19] F. Herzog, B. Ruijl, T. Ueda, J. A. M. Vermaseren, and A. Vogt, *The five-loop beta function of Yang-Mills theory with fermions*, *JHEP* **02** (2017) 090, [arXiv:1701.01404].

[20] K. G. Chetyrkin, G. Falcioni, F. Herzog, and J. A. M. Vermaseren, *Five-loop renormalisation of QCD in covariant gauges*, *JHEP* **10** (2017) 179, [arXiv:1709.08541]. [Addendum: JHEP12,006(2017)].

[21] **Particle Data Group** Collaboration, M. Tanabashi et al., *Review of particle physics*, *Phys. Rev. D* **98** (Aug, 2018) 030001.

[22] R. P. Feynman, *Very high-energy collisions of hadrons*, *Phys. Rev. Lett.* **23** (Dec, 1969) 1415–1417.

[23] C. G. Callan and D. J. Gross, *High-energy electroproduction and the constitution of the electric current*, *Phys. Rev. Lett.* **22** (Jan, 1969) 156–159.

[24] J. D. Bjorken, *Asymptotic sum rules at infinite momentum*, *Phys. Rev.* **179** (Mar, 1969) 1547–1553.

[25] T. Kinoshita, *Mass singularities of feynman amplitudes*, *Journal of Mathematical Physics* **3** (1962), no. 4 650–677, [https://doi.org/10.1063/1.1724268].

[26] T. D. Lee and M. Nauenberg, *Degenerate systems and mass singularities*, *Phys. Rev.* **133** (Mar, 1964) B1549–B1562.

[27] E. Zijlstra and W. van Neerven, *Order-α_s^2 QCD corrections to the deep inelastic proton structure functions F2 and FL*, *Nuclear Physics B* **383** (1992), no. 3 525 – 574.

[28] A. Vogt, S. Moch, and J. A. M. Vermaseren, *The three-loop splitting functions in QCD: The singlet case*, *Nucl. Phys.* **B691** (2004) 129–181, [hep-ph/0404111].

[29] S. Moch, B. Ruijl, T. Ueda, J. A. M. Vermaseren, and A. Vogt, *On quartic colour factors in splitting functions and the gluon cusp anomalous dimension*, *Phys. Lett.* **B782** (2018) 627–632, [arXiv:1805.09638].

[30] J. Davies, A. Vogt, B. Ruijl, T. Ueda, and J. A. M. Vermaseren, *Large-n_f contributions to the four-loop splitting functions in QCD*, *Nucl. Phys.* **B915** (2017) 335–362, [arXiv:1610.07477].

[31] S. Moch, B. Ruijl, T. Ueda, J. A. M. Vermaseren, and A. Vogt, *Four-Loop Non-Singlet Splitting Functions in the Planar Limit and Beyond*, arXiv:1707.08315.

[32] J. C. Collins, D. E. Soper, and G. F. Sterman, *Factorization of Hard Processes in QCD*, *Adv.Ser.Direct.High Energy Phys.* **5** (1988) 1–91, [hep-ph/0409313].

[33] J. C. Collins, D. E. Soper, and G. Sterman, *Factorization for short distance hadron-hadron scattering*, *Nuclear Physics B* **261** (1985) 104 – 142.

[34] R. Ellis, H. Georgi, M. Machacek, H. Politzer, and G. G. Ross, *Perturbation theory and the parton model in QCD*, *Nuclear Physics B* **152** (1979), no. 2 285 – 329.

[35] G. T. Bodwin, *Factorization of the Drell-Yan cross section in perturbation theory*, *Phys. Rev. D* **31** (May, 1985) 2616–2642.

[36] G. Altarelli and G. Parisi, *Asymptotic Freedom in Parton Language*, *Nucl. Phys.* **B126** (1977) 298–318.

[37] Y. L. Dokshitzer, *Calculation of the Structure Functions for Deep Inelastic Scattering and e^+e^- Annihilation by Perturbation Theory in Quantum Chromodynamics.*, *Sov. Phys. JETP* **46** (1977) 641–653. [Zh. Eksp. Teor. Fiz.73,1216(1977)].

[38] V. N. Gribov and L. N. Lipatov, *Deep inelastic e p scattering in perturbation theory*, *Sov. J. Nucl. Phys.* **15** (1972) 438–450. [Yad. Fiz.15,781(1972)].

[39] L. N. Lipatov, *The parton model and perturbation theory*, *Sov. J. Nucl. Phys.* **20** (1975) 94–102.

[40] B. Henning, X. Lu, and H. Murayama, *How to use the Standard Model effective field theory*, *JHEP* **01** (2016) 023, [arXiv:1412.1837].

[41] W. Buchmuller and D. Wyler, *Effective Lagrangian Analysis of New Interactions and Flavor Conservation*, *Nucl. Phys.* **B268** (1986) 621–653.

[42] L. F. Abbott and M. B. Wise, *Effective hamiltonian for nucleon decay*, *Phys. Rev. D* **22** (Nov, 1980) 2208–2212.

[43] F. Wilczek and A. Zee, *Operator analysis of nucleon decay*, *Phys. Rev. Lett.* **43** (Nov, 1979) 1571–1573.

[44] B. Grzadkowski, M. Iskrzynski, M. Misiak, and J. Rosiek, *Dimension-Six Terms in the Standard Model Lagrangian*, *JHEP* **10** (2010) 085, [arXiv:1008.4884].

[45] L. Lehman, *Extending the Standard Model Effective Field Theory with the Complete Set of Dimension-7 Operators*, *Phys. Rev.* **D90** (2014), no. 12 125023, [arXiv:1410.4193].

[46] L. Lehman and A. Martin, *Low-derivative operators of the Standard Model effective field theory via Hilbert series methods*, *JHEP* **02** (2016) 081, [arXiv:1510.00372].

[47] B. Henning, X. Lu, T. Melia, and H. Murayama, *2, 84, 30, 993, 560, 15456, 11962, 261485, ...: Higher dimension operators in the SM EFT*, *JHEP* **08** (2017) 016, [arXiv:1512.03433]. [Erratum: JHEP09,019(2019)].

[48] C. Degrande, N. Greiner, W. Kilian, O. Mattelaer, H. Mebane, T. Stelzer, S. Willenbrock, and C. Zhang, *Effective Field Theory: A Modern Approach to Anomalous Couplings*, *Annals Phys.* **335** (2013) 21–32, [arXiv:1205.4231].

[49] A. Kobach, *Baryon Number, Lepton Number, and Operator Dimension in the Standard Model*, *Phys. Lett.* **B758** (2016) 455–457, [arXiv:1604.05726].

[50] O. Domenech, A. Pomarol, and J. Serra, *Probing the SM with Dijets at the LHC*, *Phys. Rev.* **D85** (2012) 074030, [arXiv:1201.6510].

[51] A. Biekötter, A. Knochel, M. Krämer, D. Liu, and F. Riva, *Vices and virtues of Higgs effective field theories at large energy*, *Phys. Rev.* **D91** (2015) 055029, [arXiv:1406.7320].

[52] A. Biekötter, J. Brehmer, and T. Plehn, *Extending the limits of Higgs effective theory*, *Phys. Rev.* **D94** (2016), no. 5 055032, [arXiv:1602.05202].

[53] R. Contino, A. Falkowski, F. Goertz, C. Grojean, and F. Riva, *On the Validity of the Effective Field Theory Approach to SM Precision Tests*, *JHEP* **07** (2016) 144, [arXiv:1604.06444].

[54] J. A. Aguilar Saavedra et al., *Interpreting top-quark LHC measurements in the standard-model effective field theory*, arXiv:1802.07237.

[55] J. Ellis, C. W. Murphy, V. Sanz, and T. You, *Updated Global SMEFT Fit to Higgs, Diboson and Electroweak Data*, *JHEP* **06** (2018) 146, [arXiv:1803.03252].

[56] R. Contino, M. Ghezzi, C. Grojean, M. Muhlleitner, and M. Spira, *Effective Lagrangian for a light Higgs-like scalar*, *JHEP* **07** (2013) 035, [arXiv:1303.3876].

[57] G. F. Giudice, C. Grojean, A. Pomarol, and R. Rattazzi, *The Strongly-Interacting Light Higgs*, *JHEP* **06** (2007) 045, [hep-ph/0703164].

[58] E. E. Jenkins, A. V. Manohar, and M. Trott, *Renormalization Group Evolution of the Standard Model Dimension Six Operators I: Formalism and lambda Dependence*, *JHEP* **10** (2013) 087, [arXiv:1308.2627].

[59] R. Alonso, E. E. Jenkins, A. V. Manohar, and M. Trott, *Renormalization Group Evolution of the Standard Model Dimension Six Operators III: Gauge Coupling Dependence and Phenomenology*, *JHEP* **04** (2014) 159, [arXiv:1312.2014].

[60] E. E. Jenkins, A. V. Manohar, and M. Trott, *Renormalization Group Evolution of the Standard Model Dimension Six Operators II: Yukawa Dependence*, *JHEP* **01** (2014) 035, [arXiv:1310.4838].

[61] C. Degrande, F. Maltoni, J. Wang, and C. Zhang, *Automatic computations at next-to-leading order in QCD for top-quark flavor-changing neutral processes*, *Phys. Rev.* **D91** (2015) 034024, [arXiv:1412.5594].

[62] D. Buarque Franzosi and C. Zhang, *Probing the top-quark chromomagnetic dipole moment at next-to-leading order in QCD*, *Phys. Rev.* **D91** (2015), no. 11 114010, [arXiv:1503.08841].

[63] C. Zhang, *Single Top Production at Next-to-Leading Order in the Standard Model Effective Field Theory*, *Phys. Rev. Lett.* **116** (2016), no. 16 162002, [arXiv:1601.06163].

[64] O. Bessidskaia Bylund, F. Maltoni, I. Tsinikos, E. Vryonidou, and C. Zhang, *Probing top quark neutral couplings in the Standard Model Effective Field Theory at NLO in QCD*, *JHEP* **05** (2016) 052, [arXiv:1601.08193].

[65] F. Maltoni, E. Vryonidou, and C. Zhang, *Higgs production in association with a top-antitop pair in the Standard Model Effective Field Theory at NLO in QCD*, *JHEP* **10** (2016) 123, [arXiv:1607.05330].

[66] C. Degrande, F. Maltoni, K. Mimasu, E. Vryonidou, and C. Zhang, *Single-top associated production with a Z or H boson at the LHC: the SMEFT interpretation*, *JHEP* **10** (2018) 005, [arXiv:1804.07773].

[67] G. Durieux, M. Perelló, M. Vos, and C. Zhang, *Global and optimal probes for the top-quark effective field theory at future lepton colliders*, arXiv:1807.02121.

[68] N. Deutschmann, C. Duhr, F. Maltoni, and E. Vryonidou, *Gluon-fusion Higgs production in the Standard Model Effective Field Theory*, *JHEP* **12** (2017) 063, [arXiv:1708.00460]. [Erratum: JHEP02,159(2018)].

[69] M. Chala, J. Santiago, and M. Spannowsky, *Constraining four-fermion operators using rare top decays*, arXiv:1809.09624.

[70] G. Durieux, F. Maltoni, and C. Zhang, *Global approach to top-quark flavor-changing interactions*, *Phys. Rev.* **D91** (2015), no. 7 074017, [arXiv:1412.7166].

[71] J. A. Aguilar-Saavedra, *Effective four-fermion operators in top physics: A Roadmap*, *Nucl. Phys.* **B843** (2011) 638–672, [arXiv:1008.3562]. [Erratum: Nucl. Phys.B851,443(2011)].

[72] J. D'Hondt, A. Mariotti, K. Mimasu, S. Moortgat, and C. Zhang, *Learning to pinpoint effective operators at the LHC: a study of the $t\bar{t}b\bar{b}$ signature*, *JHEP* **11** (2018) 131, [arXiv:1807.02130].

[73] S. van Beek, E. R. Nocera, J. Rojo, and E. Slade, *Constraining the SMEFT with Bayesian reweighting*, *SciPost Phys.* **7** (2019), no. 5 070, [arXiv:1906.05296].

[74] A. Buckley, C. Englert, J. Ferrando, D. J. Miller, L. Moore, M. Russell, and C. D. White, *Global fit of top quark effective theory to data*, *Phys. Rev.* **D92** (2015), no. 9 091501, [arXiv:1506.08845].

[75] A. Buckley, C. Englert, J. Ferrando, D. J. Miller, L. Moore, M. Russell, and C. D. White, *Constraining top quark effective theory in the LHC Run II era*, *JHEP* **04** (2016) 015, [arXiv:1512.03360].

[76] S. Brown, A. Buckley, C. Englert, J. Ferrando, P. Galler, D. J. Miller, L. Moore, M. Russell, C. White, and N. Warrack, *TopFitter: Fitting*

top-quark Wilson Coefficients to Run II data, in *39th International Conference on High Energy Physics (ICHEP 2018) Seoul, Korea, July 4-11, 2018*, 2019. arXiv:1901.03164.

[77] A. Buckley, C. Englert, J. Ferrando, D. J. Miller, L. Moore, K. Nördstrom, M. Russell, and C. D. White, *Results from TopFitter*, *PoS* **CKM2016** (2016) 127, [arXiv:1612.02294].

[78] R. P. Moutafis, *A Global Analysis of the Standard Model Effective Field Theory in the Production and Decay Channels of a Single Top Quark*, Master's thesis, Orsay, LAL, 2019.

[79] I. Brivio, S. Bruggisser, F. Maltoni, R. Moutafis, T. Plehn, E. Vryonidou, S. Westhoff, and C. Zhang, *O new physics, where art thou? A global search in the top sector*, arXiv:1910.03606.

[80] A. Buckley, H. Hoeth, H. Lacker, H. Schulz, and J. E. von Seggern, *Systematic event generator tuning for the LHC*, *Eur. Phys. J.* **C65** (2010) 331–357, [arXiv:0907.2973].

[81] **Gfitter Group** Collaboration, M. Baak, J. Cúth, J. Haller, A. Hoecker, R. Kogler, K. Mönig, M. Schott, and J. Stelzer, *The global electroweak fit at NNLO and prospects for the LHC and ILC*, *Eur. Phys. J.* **C74** (2014) 3046, [arXiv:1407.3792].

[82] A. Akhundov, A. Arbuzov, S. Riemann, and T. Riemann, *The ZFITTER project*, *Phys. Part. Nucl.* **45** (2014), no. 3 529–549, [arXiv:1302.1395].

[83] J. de Blas, M. Ciuchini, E. Franco, S. Mishima, M. Pierini, L. Reina, and L. Silvestrini, *The Global Electroweak and Higgs Fits in the LHC era*, *PoS* **EPS-HEP2017** (2017) 467, [arXiv:1710.05402].

[84] A. Biekötter, T. Corbett, and T. Plehn, *The Gauge-Higgs Legacy of the LHC Run II*, arXiv:1812.07587.

[85] E. da Silva Almeida, A. Alves, N. Rosa Agostinho, O. J. P. Éboli, and M. C. Gonzalez–Garcia, *Electroweak Sector Under Scrutiny: A Combined Analysis of LHC and Electroweak Precision Data*, *Phys. Rev.* **D99** (2019), no. 3 033001, [arXiv:1812.01009].

[86] J. Aebischer, J. Kumar, P. Stangl, and D. M. Straub, *A Global Likelihood for Precision Constraints and Flavour Anomalies*, *Eur. Phys. J.* **C79** (2019), no. 6 509, [arXiv:1810.07698].

[87] **LHC Higgs Cross Section Working Group** Collaboration, D. de Florian et al., *Handbook of LHC Higgs Cross Sections: 4. Deciphering the Nature of the Higgs Sector*, arXiv:1610.07922.

[88] **Particle Data Group** Collaboration, K. Nakamura et al., *Review of particle physics*, *J.Phys.G* **G37** (2010) 075021.

[89] J. de Blas, M. Ciuchini, E. Franco, S. Mishima, M. Pierini, L. Reina, and L. Silvestrini, *Electroweak precision observables and Higgs-boson signal strengths in the Standard Model and beyond: present and future*, *JHEP* **12** (2016) 135, [arXiv:1608.01509].

[90] G. Altarelli, *The QCD Running Coupling and its Measurement*, *PoS* **Corfu2012** (2013) 002, [arXiv:1303.6065].

[91] G. P. Salam, *The strong coupling: a theoretical perspective*, in *From My Vast Repertoire ...: Guido Altarelli's Legacy* (A. Levy, S. Forte, and G. Ridolfi, eds.), pp. 101–121. 2019. arXiv:1712.05165.

[92] M. Johnson and D. Maître, *Strong coupling constant extraction from high-multiplicity Z+jets observables*, arXiv:1711.01408.

[93] **H1** Collaboration, V. Andreev et al., *Determination of the strong coupling constant $\alpha_s(m_Z)$ in next-to-next-to-leading order QCD using H1 jet cross section measurements*, *Eur. Phys. J.* **C77** (2017), no. 11 791, [arXiv:1709.07251].

[94] T. Klijnsma, S. Bethke, G. Dissertori, and G. P. Salam, *Determination of the strong coupling constant $\alpha_s(m_Z)$ from measurements of the total cross section for top-antitop quark production*, *Eur. Phys. J.* **C77** (2017), no. 11 778, [arXiv:1708.07495].

[95] **ATLAS** Collaboration, M. Aaboud et al., *Determination of the strong coupling constant α_s from transverse energy–energy correlations in multijet events at $\sqrt{s} = 8$ TeV using the ATLAS detector*, *Eur. Phys. J.* **C77** (2017), no. 12 872, [arXiv:1707.02562].

[96] B. Bouzid, F. Iddir, and L. Semlala, *Determination of the strong coupling constant from ATLAS measurements of the inclusive isolated prompt photon cross section at 7 TeV*, arXiv:1703.03959.

[97] **CMS** Collaboration, S. Chatrchyan et al., *Determination of the top-quark pole mass and strong coupling constant from the t t-bar production cross section in pp collisions at $\sqrt{s} = 7$ TeV*, *Phys.Lett.* **B728** (2014) 496, [arXiv:1307.1907].

[98] D. Britzger, K. Rabbertz, D. Savoiu, G. Sieber, and M. Wobisch, *Determination of the strong coupling constant using inclusive jet cross section data from multiple experiments*, *Eur. Phys. J.* **C79** (2019), no. 1 68, [arXiv:1712.00480].

[99] S. Lionetti et al., *Precision determination of α_s using an unbiased global NLO parton set*, *Phys. Lett.* **B701** (2011) 346–352, [arXiv:1103.2369].

[100] R. D. Ball, V. Bertone, L. Del Debbio, S. Forte, A. Guffanti, et al., *Precision NNLO determination of $\alpha_s(M_Z)$ using an unbiased global parton set*, *Phys.Lett.* **B707** (2012) 66–71, [arXiv:1110.2483].

[101] **The NNPDF** Collaboration, R. D. Ball et al., *Impact of Heavy Quark Masses on Parton Distributions and LHC Phenomenology*, *Nucl. Phys.* **B849** (2011) 296–363, [arXiv:1101.1300].

[102] **The NNPDF** Collaboration, R. D. Ball et al., *Unbiased global determination of parton distributions and their uncertainties at NNLO and at LO*, *Nucl.Phys.* **B855** (2012) 153–221, [arXiv:1107.2652].

[103] L. A. Harland-Lang and R. S. Thorne, *On the Consistent Use of Scale Variations in PDF Fits and Predictions*, *Eur. Phys. J.* **C79** (2019), no. 3 225, [arXiv:1811.08434].

[104] **NNPDF** Collaboration, R. Abdul Khalek et al., *Parton Distributions with Theory Uncertainties: General Formalism and First Phenomenological Studies*, *Eur. Phys. J.* **C79** (2019), no. 11 931, [arXiv:1906.10698].

[105] **NNPDF** Collaboration, R. D. Ball et al., *Parton distributions for the LHC Run II*, *JHEP* **04** (2015) 040, [arXiv:1410.8849].

[106] A. D. Martin, R. G. Roberts, W. J. Stirling, and R. S. Thorne, *Uncertainties of predictions from parton distributions. I: Experimental errors*, *Eur. Phys. J.* **C28** (2003) 455–473, [hep-ph/0211080].

[107] J. Pumplin et al., *Uncertainties of predictions from parton distribution functions. 2. The Hessian method*, *Phys. Rev.* **D65** (2001) 014013, [hep-ph/0101032].

[108] A. D. Martin, W. J. Stirling, R. S. Thorne, and G. Watt, *Parton distributions for the LHC*, *Eur. Phys. J.* **C63** (2009) 189, [arXiv:0901.0002].

[109] V. Bertone, S. Carrazza, and J. Rojo, *APFEL: A PDF Evolution Library with QED corrections*, *Comput.Phys.Commun.* **185** (2014) 1647–1668, [arXiv:1310.1394].

[110] V. Bertone, S. Carrazza, and N. P. Hartland, *APFELgrid: a high performance tool for parton density determinations*, *Comput. Phys. Commun.* **212** (2017) 205–209, [arXiv:1605.02070].

[111] B. Efron and R. J. Tibshirani, *An Introduction to the Bootstrap*. No. 57 in Monographs on Statistics and Applied Probability. Chapman & Hall/CRC, Boca Raton, Florida, USA, 1993.

[112] J. Currie, E. W. N. Glover, and J. Pires, *Next-to-Next-to Leading Order QCD Predictions for Single Jet Inclusive Production at the LHC*, *Phys. Rev. Lett.* **118** (2017), no. 7 072002, [arXiv:1611.01460].

[113] **ATLAS** Collaboration, G. Aad et al., *Measurement of the inclusive jet cross-section in proton-proton collisions at $\sqrt{s} = 7$ TeV using 4.5 fb^{-1} of data with the ATLAS detector*, *JHEP* **02** (2015) 153, [arXiv:1410.8857]. [Erratum: JHEP09,141(2015)].

[114] **CMS** Collaboration, S. Chatrchyan et al., *Measurements of differential jet cross sections in proton-proton collisions at $\sqrt{s} = 7$ TeV with the CMS detector*, *Phys.Rev.* **D87** (2013) 112002, [arXiv:1212.6660].

[115] A. D. Martin, W. J. Stirling, R. S. Thorne, and G. Watt, *Uncertainties on α_S in global PDF analyses*, *Eur. Phys. J.* **C64** (2009) 653–680, [arXiv:0905.3531].

[116] S. Forte and Z. Kassabov, *Why α_s Cannot be Determined from Hadronic Processes without Simultaneously Determining the Parton Distributions*, *Eur. Phys. J.* **C80** (2020), no. 3 182, [arXiv:2001.04986].

[117] S. Alekhin, J. Blümlein, S. Moch, and R. Placakyte, *Parton distribution functions, α_s, and heavy-quark masses for LHC Run II*, *Phys. Rev.* **D96** (2017), no. 1 014011, [arXiv:1701.05838].

[118] L. A. Harland-Lang, A. D. Martin, P. Motylinski, and R. S. Thorne, *Uncertainties on α_S in the MMHT2014 global PDF analysis and implications for SM predictions*, arXiv:1506.05682.

[119] R. D. Ball and A. Deshpande, *The Proton Spin, Semi-Inclusive processes, and a future Electron Ion Collider*, 2018. arXiv:1801.04842.

[120] J. Skilling, *Nested sampling*, *AIP Conference Proceedings* **735** (2004), no. 1 395–405.

[121] J. Skilling, *Nested sampling for general bayesian computation*, *Bayesian Anal.* **1** (12, 2006) 833–859.

[122] F. Feroz, M. P. Hobson, E. Cameron, and A. N. Pettitt, *Importance Nested Sampling and the MultiNest Algorithm*, arXiv:1306.2144.

[123] **ATLAS** Collaboration, G. Aad et al., *Measurements of top-quark pair differential cross-sections in the lepton+jets channel in pp collisions at $\sqrt{s} = 8$ TeV using the ATLAS detector*, *Eur. Phys. J.* **C76** (2016), no. 10 538, [arXiv:1511.04716].

[124] **CMS** Collaboration, V. Khachatryan et al., *Measurement of the differential cross section for top quark pair production in pp collisions at $\sqrt{s} = 8$ TeV*, *Eur. Phys. J.* **C75** (2015), no. 11 542, [arXiv:1505.04480].

[125] **CMS** Collaboration, A. M. Sirunyan et al., *Measurement of double-differential cross sections for top quark pair production in pp collisions at $\sqrt{s} = 8$ TeV and impact on parton distribution functions*, *Eur. Phys. J.* **C77** (2017), no. 7 459, [arXiv:1703.01630].

[126] **CMS** Collaboration, V. Khachatryan et al., *Measurement of differential cross sections for top quark pair production using the lepton+jets final state in proton-proton collisions at 13 TeV*, *Phys. Rev.* **D95** (2017), no. 9 092001, [arXiv:1610.04191].

[127] **CMS** Collaboration, A. M. Sirunyan et al., *Measurement of differential cross sections for the production of top quark pairs and of additional jets in lepton+jets events from pp collisions at $\sqrt{s} = 13$ TeV*, *Phys. Rev.* **D97** (2018), no. 11 112003, [arXiv:1803.08856].

[128] **CMS** Collaboration, A. M. Sirunyan et al., *Measurement of normalized differential $t\bar{t}$ cross sections in the dilepton channel from pp collisions at $\sqrt{s} = 13$ TeV*, *JHEP* **04** (2018) 060, [arXiv:1708.07638].

[129] **ATLAS** Collaboration, M. Aaboud et al., *Measurement of the W boson polarisation in $t\bar{t}$ events from pp collisions at $\sqrt{s} = 8$ TeV in the lepton + jets channel with ATLAS*, *Eur. Phys. J.* **C77** (2017), no. 4 264, [arXiv:1612.02577].

[130] **CMS** Collaboration, V. Khachatryan et al., *Measurement of the W boson helicity fractions in the decays of top quark pairs to lepton + jets final states produced in pp collisions at $\sqrt{s} = 8$ TeV*, *Phys. Lett.* **B762** (2016) 512–534, [arXiv:1605.09047].

[131] **CMS** Collaboration, A. M. Sirunyan et al., *Measurements of $t\bar{t}$ cross sections in association with b jets and inclusive jets and their ratio using dilepton final states in pp collisions at $\sqrt{s} = 13$ TeV*, *Phys. Lett.* **B776** (2018) 355–378, [arXiv:1705.10141].

[132] **CMS** Collaboration, A. M. Sirunyan et al., *Search for standard model production of four top quarks with same-sign and multilepton final states in proton–proton collisions at $\sqrt{s} = 13$ TeV*, *Eur. Phys. J.* **C78** (2018), no. 2 140, [arXiv:1710.10614].

[133] **CMS** Collaboration, V. Khachatryan et al., *Observation of top quark pairs produced in association with a vector boson in pp collisions at $\sqrt{s} = 8$ TeV*, *JHEP* **01** (2016) 096, [arXiv:1510.01131].

[134] **CMS** Collaboration, A. M. Sirunyan et al., *Measurement of the cross section for top quark pair production in association with a W or Z boson in proton-proton collisions at $\sqrt{s} = 13$ TeV*, *JHEP* **08** (2018) 011, [arXiv:1711.02547].

[135] **ATLAS** Collaboration, G. Aad et al., *Measurement of the $t\bar{t}W$ and $t\bar{t}Z$ production cross sections in pp collisions at $\sqrt{s} = 8$ TeV with the ATLAS detector*, *JHEP* **11** (2015) 172, [arXiv:1509.05276].

[136] **ATLAS** Collaboration, M. Aaboud et al., *Measurement of the $t\bar{t}Z$ and $t\bar{t}W$ production cross sections in multilepton final states using 3.2 fb^{-1} of pp collisions at $\sqrt{s}$ = 13 TeV with the ATLAS detector*, *Eur. Phys. J.* **C77** (2017), no. 1 40, [arXiv:1609.01599].

[137] **CMS** Collaboration, A. M. Sirunyan et al., *Observation of $t\bar{t}H$ production*, *Phys. Rev. Lett.* **120** (2018), no. 23 231801, [arXiv:1804.02610].

[138] **ATLAS** Collaboration, M. Aaboud et al., *Observation of Higgs boson production in association with a top quark pair at the LHC with the ATLAS detector*, *Phys. Lett.* **B784** (2018) 173–191, [arXiv:1806.00425].

[139] **CMS** Collaboration, V. Khachatryan et al., *Measurement of the t-channel single-top-quark production cross section and of the $| V_{tb} |$ CKM matrix element in pp collisions at $\sqrt{s}$= 8 TeV*, *JHEP* **06** (2014) 090, [arXiv:1403.7366].

[140] **CMS** Collaboration, V. Khachatryan et al., *Search for s channel single top quark production in pp collisions at $\sqrt{s} = 7$ and 8 TeV*, *JHEP* **09** (2016) 027, [arXiv:1603.02555].

[141] **ATLAS** Collaboration, G. Aad et al., *Evidence for single top-quark production in the s-channel in proton-proton collisions at $\sqrt{s}$ =8 TeV with the ATLAS detector using the Matrix Element Method*, *Phys. Lett.* **B756** (2016) 228–246, [arXiv:1511.05980].

[142] **ATLAS** Collaboration, M. Aaboud et al., *Fiducial, total and differential cross-section measurements of t-channel single top-quark production in pp collisions at 8 TeV using data collected by the ATLAS detector*, *Eur. Phys. J.* **C77** (2017), no. 8 531, [arXiv:1702.02859].

[143] **ATLAS** Collaboration, M. Aaboud et al., *Measurement of the inclusive cross-sections of single top-quark and top-antiquark t-channel production in pp collisions at $\sqrt{s}$ = 13 TeV with the ATLAS detector*, *JHEP* **04** (2017) 086, [arXiv:1609.03920].

[144] **CMS** Collaboration, A. M. Sirunyan et al., *Cross section measurement of t-channel single top quark production in pp collisions at $\sqrt{s}$ = 13 TeV*, *Phys. Lett.* **B772** (2017) 752–776, [arXiv:1610.00678].

[145] **CMS Collaboration** Collaboration, A. M. Sirunyan et al., *Single top t-channel differential cross section at 8 TeV*, *CMS-PAS-TOP-14-004* (2014) https://cds.cern.ch/record/1956681.

[146] **CMS** Collaboration, V. Khachatryan et al., *Measurement of the differential cross section for t-channel single-top-quark production at $\sqrt{s} = 13$ TeV*, *CMS-PAS-TOP-16-004* (2016) https://cds.cern.ch/record/2151074.

[147] **ATLAS** Collaboration, G. Aad et al., *Measurement of the production cross-section of a single top quark in association with a W boson at 8 TeV with the ATLAS experiment*, *JHEP* **01** (2016) 064, [arXiv:1510.03752].

[148] **CMS** Collaboration, S. Chatrchyan et al., *Observation of the associated production of a single top quark and a W boson in pp collisions at $\sqrt{s}$ =8 TeV*, *Phys. Rev. Lett.* **112** (2014), no. 23 231802, [arXiv:1401.2942].

[149] **ATLAS** Collaboration, M. Aaboud et al., *Measurement of the cross-section for producing a W boson in association with a single top quark in pp collisions at $\sqrt{s} = 13$ TeV with ATLAS*, *JHEP* **01** (2018) 063, [arXiv:1612.07231].

[150] **CMS** Collaboration, A. M. Sirunyan et al., *Measurement of the production cross section for single top quarks in association with W bosons in proton-proton collisions at $\sqrt{s} = 13$ TeV*, *JHEP* (2018) [arXiv:1805.07399].

[151] **CMS** Collaboration, A. M. Sirunyan et al., *Measurement of the associated production of a single top quark and a Z boson in pp collisions at $\sqrt{s} =$ TeV*, *Phys. Lett.* **B779** (2018) 358–384, [arXiv:1712.02825].

[152] **ATLAS** Collaboration, M. Aaboud et al., *Measurement of the production cross-section of a single top quark in association with a Z boson in proton–proton collisions at 13 TeV with the ATLAS detector*, *Phys. Lett.* **B780** (2018) 557–577, [arXiv:1710.03659].

[153] M. Czakon, M. L. Mangano, A. Mitov, and J. Rojo, *Constraints on the gluon PDF from top quark pair production at hadron colliders*, *JHEP* **1307** (2013) 167, [arXiv:1303.7215].

[154] M. Czakon, N. P. Hartland, A. Mitov, E. R. Nocera, and J. Rojo, *Pinning down the large-x gluon with NNLO top-quark pair differential distributions*, *JHEP* **04** (2017) 044, [arXiv:1611.08609].

[155] M. Czakon, D. Heymes, and A. Mitov, *Dynamical scales for multi-TeV top-pair production at the LHC*, *JHEP* **04** (2017) 071, [arXiv:1606.03350].

[156] T. Gleisberg et al., *Event generation with SHERPA 1.1*, *JHEP* **02** (2009) 007, [arXiv:0811.4622].

[157] R. Boughezal, J. M. Campbell, R. K. Ellis, C. Focke, W. Giele, X. Liu, F. Petriello, and C. Williams, *Color singlet production at NNLO in MCFM*, *Eur. Phys. J.* **C77** (2017), no. 1 7, [arXiv:1605.08011].

[158] M. Czakon, D. Heymes, and A. Mitov, *fastNLO tables for NNLO top-quark pair differential distributions*, arXiv:1704.08551.

[159] **CMS** Collaboration, A. M. Sirunyan et al., *Measurements of $t\bar{t}$ differential cross sections in proton-proton collisions at $\sqrt{s} = 13$ TeV using events containing two leptons*, arXiv:1811.06625.

[160] **ATLAS** Collaboration, M. Aaboud et al., *Measurements of top-quark pair differential cross-sections in the lepton+jets channel in pp collisions at $\sqrt{s} = 13$ TeV using the ATLAS detector*, *JHEP* **11** (2017) 191, [arXiv:1708.00727].

[161] **ATLAS** Collaboration, M. Aaboud et al., *Measurements of top-quark pair differential cross-sections in the $e\mu$ channel in pp collisions at $\sqrt{s} = 13$ TeV using the ATLAS detector*, *Eur. Phys. J.* **C77** (2017), no. 5 292, [arXiv:1612.05220].

[162] **ATLAS** Collaboration, M. Aaboud et al., *Measurements of $t\bar{t}$ differential cross-sections of highly boosted top quarks decaying to all-hadronic final states in pp collisions at $\sqrt{s} = 13$ TeV using the ATLAS detector*, *Phys. Rev.* **D98** (2018), no. 1 012003, [arXiv:1801.02052].

[163] M. Czakon, D. Heymes, A. Mitov, D. Pagani, I. Tsinikos, and M. Zaro, *Top-pair production at the LHC through NNLO QCD and NLO EW*, *JHEP* **10** (2017) 186, [arXiv:1705.04105].

[164] M. Czakon, A. Ferroglia, D. Heymes, A. Mitov, B. D. Pecjak, D. J. Scott, X. Wang, and L. L. Yang, *Resummation for (boosted) top-quark pair production at NNLO+NNLL' in QCD*, *JHEP* **05** (2018) 149, [arXiv:1803.07623].

[165] **ATLAS** Collaboration, M. Aaboud et al., *Measurement of the $t\bar{t}\gamma$ production cross section in proton-proton collisions at $\sqrt{s} = 8$ TeV with the ATLAS detector*, *JHEP* **11** (2017) 086, [arXiv:1706.03046].

[166] **ATLAS** Collaboration, G. Aad et al., *Observation of top-quark pair production in association with a photon and measurement of the $t\bar{t}\gamma$ production cross section in pp collisions at $\sqrt{s} = 7$ TeV using the ATLAS detector*, *Phys. Rev.* **D91** (2015), no. 7 072007, [arXiv:1502.00586].

[167] **CMS** Collaboration, A. M. Sirunyan et al., *Measurement of the semileptonic $t\bar{t} + \gamma$ production cross section in pp collisions at $\sqrt{s} = 8$ TeV*, *JHEP* **10** (2017) 006, [arXiv:1706.08128].

[168] **CMS** Collaboration, *Measurement of top quark pair production in association with a Z boson in proton-proton collisions at $\sqrt{s} = 13$ TeV*, arXiv:1907.11270.

[169] **CMS** Collaboration, V. Khachatryan et al., *Measurement of $t\bar{t}$ production with additional jet activity, including* b *quark jets, in the dilepton decay channel using pp collisions at $\sqrt{s} = 8$ TeV*, *Eur. Phys. J.* **C76** (2016), no. 7 379, [arXiv:1510.03072].

[170] C. Englert, M. Russell, and C. D. White, *Effective Field Theory in the top sector: do multijets help?*, *Phys. Rev.* **D99** (2019), no. 3 035019, [arXiv:1809.09744].

[171] **ATLAS** Collaboration, *Measurements of fiducial and differential cross-sections of $t\bar{t}$ production with additional heavy-flavour jets in proton-proton collisions at $\sqrt{s} = 13$ TeV with the ATLAS detector*, *ATLAS-CONF-2018-029* (Jul, 2018) https://cds.cern.ch/record/2628772/.

[172] **ATLAS** Collaboration, G. Aad et al., *Measurements of fiducial cross-sections for $t\bar{t}$ production with one or two additional b-jets in pp collisions at $\sqrt{s}$ =8 TeV using the ATLAS detector*, *Eur. Phys. J.* **C76** (2016), no. 1 11, [arXiv:1508.06868].

[173] **CMS** Collaboration, V. Khachatryan et al., *Search for Standard Model Production of Four Top Quarks in the Lepton + Jets Channel in pp Collisions at $\sqrt{s} = 8$ TeV*, *JHEP* **11** (2014) 154, [arXiv:1409.7339].

[174] **CMS** Collaboration, A. M. Sirunyan et al., *Search for standard model production of four top quarks in proton-proton collisions at $\sqrt{s} = 13$ TeV*, *Phys. Lett.* **B772** (2017) 336–358, [arXiv:1702.06164].

[175] *Search for four-top-quark production in final states with one charged lepton and multiple jets using 3.2 fb^{-1} of proton-proton collisions at $\sqrt{s} = 13$ TeV with the ATLAS detector at the LHC*, Tech. Rep. ATLAS-CONF-2016-020, CERN, Geneva, Apr, 2016.

[176] **ATLAS** Collaboration, M. Aaboud et al., *Search for four-top-quark production in the single-lepton and opposite-sign dilepton final states in pp collisions at $\sqrt{s}$ = 13 TeV with the ATLAS detector*, arXiv:1811.02305.

[177] **CMS** Collaboration, A. M. Sirunyan et al., *Search for production of four top quarks in final states with same-sign or multiple leptons in proton-proton collisions at $\sqrt{s}$ = 13 TeV*, *Eur. Phys. J.* **C80** (2020), no. 2 75, [arXiv:1908.06463].

[178] **CMS** Collaboration, A. M. Sirunyan et al., *Search for the production of four top quarks in the single-lepton and opposite-sign dilepton final states in proton-proton collisions at $\sqrt{s}$ = 13 TeV*, *JHEP* **11** (2019) 082, [arXiv:1906.02805].

[179] **CMS** Collaboration, A. M. Sirunyan et al., *Measurement of the $t\bar{t}b\bar{b}$ production cross section in the all-jet final state in pp collisions at $\sqrt{s}$ = 13 TeV*, arXiv:1909.05306.

[180] A. Giammanco, *Single top quark production at the LHC*, *Rev. Phys.* **1** (2016) 1–12, [arXiv:1511.06748].

[181] **CMS** Collaboration, A. M. Sirunyan et al., *Measurement of differential cross sections and charge ratios for t-channel single top quark production in proton-proton collisions at $\sqrt{s}$ = 13 TeV*, arXiv:1907.08330.

[182] E. L. Berger, J. Gao, C. P. Yuan, and H. X. Zhu, *NNLO QCD Corrections to t-channel Single Top-Quark Production and Decay*, *Phys. Rev.* **D94** (2016), no. 7 071501, [arXiv:1606.08463].

[183] **ATLAS** Collaboration, M. Aaboud et al., *Measurement of differential cross-sections of a single top quark produced in association with a W boson at $\sqrt{s} = 13$ TeV with ATLAS*, *Eur. Phys. J.* **C78** (2018), no. 3 186, [arXiv:1712.01602].

[184] **CMS** Collaboration, S. Chatrchyan et al., *Evidence for associated production of a single top quark and W boson in pp collisions at $\sqrt{s}$ = 7 TeV*, *Phys. Rev. Lett.* **110** (2013) 022003, [arXiv:1209.3489].

[185] S. Frixione, E. Laenen, P. Motylinski, B. R. Webber, and C. D. White, *Single-top hadroproduction in association with a W boson*, *JHEP* **07** (2008) 029, [arXiv:0805.3067].

[186] F. Demartin, B. Maier, F. Maltoni, K. Mawatari, and M. Zaro, *tWH associated production at the LHC*, *Eur. Phys. J.* **C77** (2017), no. 1 34, [arXiv:1607.05862].

[187] **CMS** Collaboration, A. M. Sirunyan et al., *Observation of single top quark production in association with a Z boson in proton-proton collisions at 13 TeV*, arXiv:1812.05900.

[188] **ATLAS, CMS** Collaboration, M. Aaboud et al., *Combinations of single-top-quark production cross-section measurements and $|f_{\mathrm{LV}}V_{tb}|$ determinations at $\sqrt{s} = 7$ and 8 TeV with the ATLAS and CMS experiments*, *JHEP* **05** (2019) 088, [arXiv:1902.07158].

[189] P. Artoisenet, P. de Aquino, F. Demartin, R. Frederix, S. Frixione, et al., *A framework for Higgs characterisation*, *JHEP* **1311** (2013) 043, [arXiv:1306.6464].

[190] F. Maltoni, K. Mawatari, and M. Zaro, *Higgs characterisation via vector-boson fusion and associated production: NLO and parton-shower effects*, *Eur. Phys. J.* **C74** (2014), no. 1 2710, [arXiv:1311.1829].

[191] F. Demartin, F. Maltoni, K. Mawatari, B. Page, and M. Zaro, *Higgs characterisation at NLO in QCD: CP properties of the top-quark Yukawa interaction*, *Eur.Phys.J.* **C74** (2014), no. 9 3065, [arXiv:1407.5089].

[192] F. Demartin, F. Maltoni, K. Mawatari, and M. Zaro, *Higgs production in association with a single top quark at the LHC*, *Eur. Phys. J.* **C75** (2015), no. 6 267, [arXiv:1504.00611].

[193] K. Mimasu, V. Sanz, and C. Williams, *Higher Order QCD predictions for Associated Higgs production with anomalous couplings to gauge bosons*, *JHEP* **08** (2016) 039, [arXiv:1512.02572].

[194] C. Degrande, B. Fuks, K. Mawatari, K. Mimasu, and V. Sanz, *Electroweak Higgs boson production in the standard model effective field theory beyond leading order in QCD*, *Eur. Phys. J.* **C77** (2017), no. 4 262, [arXiv:1609.04833].

[195] S. Alioli, W. Dekens, M. Girard, and E. Mereghetti, *NLO QCD corrections to SM-EFT dilepton and electroweak Higgs boson production, matched to parton shower in POWHEG*, *JHEP* **08** (2018) 205, [arXiv:1804.07407].

[196] C. Zhang, *Effective field theory approach to top-quark decay at next-to-leading order in QCD*, *Phys. Rev.* **D90** (2014), no. 1 014008, [arXiv:1404.1264].

[197] C. Zhang, *Constraining qqtt operators from four-top production: a case for enhanced EFT sensitivity*, *Chin. Phys.* **C42** (2018), no. 2 023104, [arXiv:1708.05928].

[198] C. Englert and M. Russell, *Top quark electroweak couplings at future lepton colliders*, *Eur. Phys. J.* **C77** (2017), no. 8 535, [arXiv:1704.01782].